Analysis of a Car Door Subjected to Side Impact

Christopher Robert Long

Thesis presented in part fulfilment of the requirements of the degree of Master of Science in Mechanical Engineering

BLAST IMPACT AND SURVIVABILITY RESEARCH UNIT

Department of Mechanical Engineering
University of Cape Town
2014 – 2015

Plagiarism Declaration

I, Christopher Robert Long, hereby declare that the work on which this thesis is based is my original work (except where acknowledgements indicate otherwise) and that neither the whole work nor any part of it has been, is being, or is to be submitted for another degree in this or any other university. I authorise the University to reproduce for the purpose of research either the whole or any portion of the contents in any manner whatsoever.

I know the meaning of plagiarism and declare that all the work in the document, save for that which is properly acknowledged, is my own.

Signature: Christopher Robert Long Date: 15 February 2016

Abstract

The study presented in this thesis focuses on the response of a side impact beam located in a car door to impact loading in close conformation to the Federal Motor Vehicle Safety Standard 214 (FMVSS 214) standard. The side impact beam is situated in both the front and rear side doors of a vehicle between the inner and outer shells to minimise intrusion into the passenger compartment whilst absorbing as much impact energy as possible in a collision. While some manufacturers use tubular side impact beams, others use corrugated structures. Different materials are also considered, depending on the class of vehicle, and market for which it is intended.

In this study, a numerical model of a light-weight passenger car, developed by the National Crash Analysis Center (NCAC) of The George Washington University under contract with the Federal Highway Administration (FHWA) and National Highway Traffic Safety Administration (NHTSA) of the United States Department of Transportation (US DOT), was used to simulate a side impact on the front side door using the LS-DYNA R7.1.1 explicit solver. The resulting deformation of the door from the full vehicle model was used to design an experiment for an impact test on a passenger door, which was used to validate an equivalent numerical simulation. In the experiments, the car door was modified and subjected to a drop mass of 385 kg from a height of 1.27 m. The drop mass and height were chosen such that the maximum deflection in the car door impact test would be of similar magnitude to the deflection of the door in full vehicle model when subjected to an impact load in accordance with the FMVSS 214 Standard - which requires that the vehicle be projected into a rigid vertical 10 inch diameter pole at 29 km/h in a direction 75° to the longitudinal axis of the vehicle. The results from the numerical simulation of the struck door test were in good agreement with the experiments in both shape and magnitude of deformation.

The behaviour of the side impact beam located in the passenger door was isolated and further studied. Drop test experiments on beams with square and round cross-sections were carried out to validate the equivalent finite element model. The drop mass and height of the striker was varied such that

the transient response of the isolated side impact beam matched the response of the beam in the simulation of the equivalent door model and full vehicle model. In the impact test experiments, the tubular structures were subjected to a 200 kg mass dropped from six incrementally varying heights of 250-500 mm. Both square and round tubes were observed to buckle at approximately 835 mm from the free end with different magnitudes of maximum deformation (depending on the drop height). The results from the numerical simulations showed good correlation with the experiments for shape and magnitude of deformation. A quadratic curve fit to the experimental maximum transverse deflection resulted in an R-squared value of 0.92 and 0.96 for the square and round tubes respectively.

A parametric study was carried out on the side impact beam to investigate the effect of:

- Thickness and material of a singular tube configuration, and
- Inner tube length and outer tube thickness of a compound tube structure.

The performance of the different configurations were assessed in terms of Crash Force Efficiency (CFE) and Specific Energy Absorption (SEA). A parametric study on the effect of the tube thickness showed that thicker tubes of the same material exhibited deformation of lower magnitude and had lower SEA. Aluminium tubes absorbed two or more times the energy per unit mass than the equivalent steel tubes. A round aluminium tube with a thickness of 2.175 mm was found to give the best balance between SEA and maximum deflection with values of 1.5 kJ/kg and 350 mm respectively. The compound tube configuration with the inner tube extended beyond the buckling point performed better in terms of SEA and maximum deflection provided the length of the inner tube did not exceed 90% of the length of the outer tube. The optimised compound tube configuration performed better than the single tube configuration in the full vehicle model with a 1mm reduction in the overall intrusion of the rigid pole.

Acknowledgements

I would like to express my appreciation and gratitude to my project supervisor, Dr Steeve Chung Kim Yuen for his invaluable assistance and support throughout the duration of the project. Regardless of the number of times I went to him he always made himself available to assist. I would also like express my gratitude to my co-supervisor and mentor Professor Gerald Nurick for his words of encouragement, guidance, and support. They have both been an inspiration to me for which I am honoured to have had the opportunity to be supervised and mentored. I would also like to thank the John Davidson Educational Trust, the University of Cape Town Postgraduate Funding Centre, and the Centre for High Performance Computing without which it would not have been possible to complete this research project. Lastly, I would like to thank all my friends and family for their love and support throughout the duration of this project.

Table of Contents

List of Tables

List of Figures

Glossary

ABS – Antilock Braking System 4

ASM - Active Stability Management 4

CFE - Crash Force Efficiency 6, 15, 111, 125

CG - Centre of Gravity 62, 63

EA - Energy Absorption 15, 32

EDS - Energy-dispersive X-ray spectroscopy 55, 82

EMU - Electron Microscope Unit 55

FE - Finite Element 37, 49, 61, 66

FEA - Finite Element Analysis 43, 162

FGF - Functionally Graded Foam 30, 32

FGT - Functionally Graded Thickness 29, 30

FHWA - Federal Highway Administration ..... iii, 61

FLOPS - Floating Point Operations per Second 46

FMVSS - Federal Motor Vehicle Safety Standard 6, 11, 59, 64

fps - Frames per Second 75, 76, 80, 107

G - Gravitational Acceleration 68

HAZ - Heat Affected Zone 61, 122

HLDI - Highway Loss Data Institute 11

IIHS - Insurance Institute for Highway Safety 1, 11

MASH - Manual of the Assessment of Safety Hardware 62, 63

MDB - Mobile Deformable Barrier 12, 13, 14, 41

MOPSO - Multiobjective Particle Optimisation 30

NCAP - New Car Assessment Program 12, 14, 62, 63

NCHRP - National Cooperative Highway Research Program 62, 63

NHTSA - National Highway Traffic Safety Administration 11, 13, 15, 63

NTSB - National Transportation Safety Board 11

PTFE - Polytetrafluoroethylene 162, 163, 164, 165

ROM - Reduced Order Model 31, 38

RSM - Response Surface Method 38, 41

SEA - Specific Energy Absorption 6, 16, 29, 37

SEM – Scanning Electron Microscopy 6, 55, 82, 133

SPI - Synthetic Performance Indicator 16, 27, 111

TC – Traction Control 4

UK - United Kingdom 12

UN-ECE - United Nations Economic Commission for Europe 12

US DOT - United States Department of Transportation ..... iii, 11, 61

UTS - Ultimate Tensile Strength 16, 44

Chapter 1

Introduction

1.1 Background

Since the advent of the automobile in 1888 car manufacturers used style and affordability as the biggest selling points for their new models when cars were initially developed [1]. Henry Ford stated that manufacturing safe vehicles was unprofitable and consumers were not interested in safety [1]. In 1965, Ralph Nader published a book titled Unsafe at Any Speed which accused car manufacturers of resisting the introduction of basic safety implements into their vehicles so as to maximise profits, at the expense of the safety of consumers [1]. This led to a revolution of the industry with the introduction of several automotive regulatory car safety bodies such as the National Highway Traffic Safety administration (NHTSA), Insurance Institute for Highway Safety (IIHS) and European New Car Assessment Program (Euro NCAP). Research in the field of automotive safety has since led to significant safety improvements. However, there is still much to improve on in automotive safety.

1.1.1 Crash Statistics

In 2015 the World Health Organisation (WHO) estimated that road injury claimed almost 3300 lives each day [2]. This was an increase from 2900 deaths a day at the turn of the 21st century, thus making road accidents one of the top 10 leading causes of death worldwide [3]. Figure 1.1 illustrates the distribution of the 10 most common causes of death for every 1000 people who died in 2012. The 10 most common causes of death amounted to 51.4% of all fatalities [3]. The lower/upper middle

income groups as indicated in Figure 1.1, and people aged 15-29 years as indicated in Figure 1.2 were most vulnerable to road injury. It was also reported that approximately 18% of all injuries and 35% of all serious and fatal injuries occurred where the principal component of the force was lateral to the vehicle [4, 5, 6]. In the United States and Europe side impact collisions accounted for between 20-40% of all accidents [7, 6, 8, 9] with 18.2% of collisions involving driver side impact and 13.8% of collisions involving passenger side impact [7]. This has led to significant international research interest from automobile manufacturers and traffic safety regulators in side impact protection.

Studies have shown that the main cause of injury to persons in side impact collisions can be attributed to intrusion of the vehicle side panel into the occupant compartment, with nearside occupants four times more likely to sustain serious or fatal injuries than farside occupants [8, 10, 11, 12]. The term 'accident' implies an unavoidable event in which a person or equipment is unintentionally harmed, when in fact all collisions are avoidable provided the correct measures are in place. However, for the purpose of consistency between this thesis and other published material the term 'accident' shall be used to describe a collision between a vehicle and some other object.

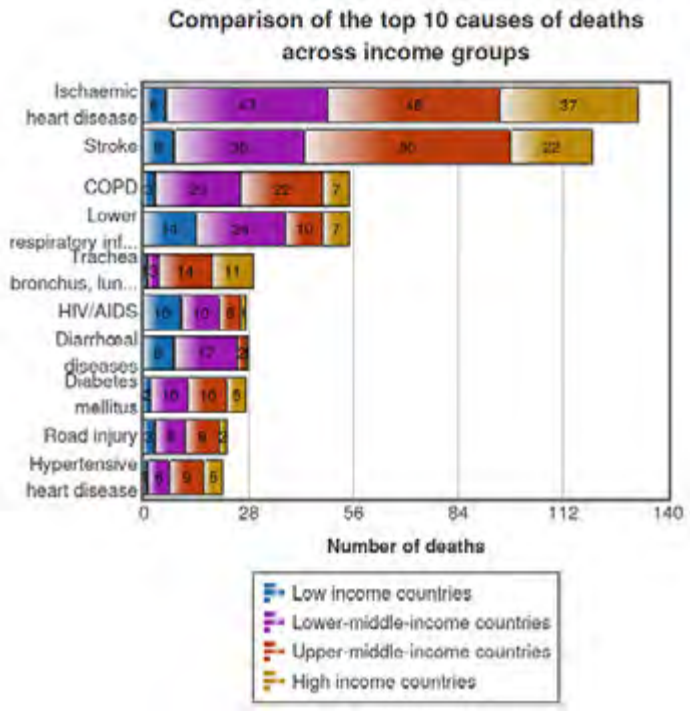

Figure 1.1: Comparison of the top ten causes of death across all income groups worldwide for every 1000 deaths [3].

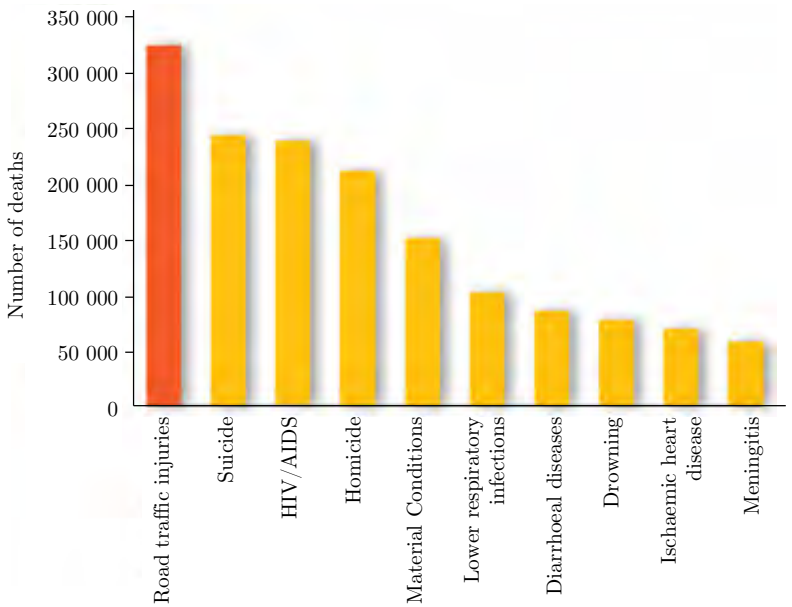

Figure 1.2: Top ten causes of death among people aged from 15-29 years [2].

Table 1.1 shows a breakdown of the types of injuries incurred for different ranges of the Abbreviated Injury Scale (AIS). The AIS is a representative score of the severity of injury. A description of the severity of each score given as follows [8, 13]:

- 1 – minor injuries such as superficial lacerations where the chance of mortality resulting from induced injuries are less than 1%,
- 2 – intermediate injuries, such as a fractured sternum where the likelihood of death is 1-2%,
- 3 – serious injury such as open fracture of the humerus, with likelihood of death from 8-10%,
- 4 – severe injury such as a perforated trachea, with the likelihood of fatality from 5-50%,
- 5 – critical injuries such as ruptured liver with the likelihood of death from 5-50%, and
- 6 – injuries fatal in nature, an example being total severance of the aorta.

Table 1.1: Breakdown of injuries in side impact collisions according to the Abbreviated Injury Scale [8].

AIS	**3-6**	**4-6**	**5-6**	**6**
Head (%)	12.2	28.7	34.5	32.0
Neck (%)	6.7	0.4	18.1	46.6
Abdomen (%)	15.6	24.2	21.0	0.1
Chest (%)	38.3	24.2	24.5	19.4
Other (%)	27.2	22.5	1.9	1.9

Table 1.1 shows that for AIS scores ranging from 3-6, chest injuries are the predominant form of trauma, whereas for AIS scores of 6 the type of injury predominant is in the head and neck region. This has led to the development of safety implements targeted at protecting parts of the body most susceptible to injuries severe or fatal in nature. One such example is the curtain airbag, which is aimed at protecting the head and neck from severe or fatal injuries during a side impact collision.

1.1.2 Active and Passive Safety

The modern automobile is now fitted with a number of implements designed to prevent accidents, and to keep occupants and pedestrians as safe as possible should an accident occur. Such implements typically fall into two main categories, namely active and passive safety, also referred to as primary and secondary safety devices. Active safety refers to any implement which serves to reduce the likelihood of accidents, such examples are a good suspension and stiff chassis, good steering and brakes, as well as electronic safety devices such as Anti-lock Braking System (ABS), Traction Control (TC), and Active Stability Management (ASM). More sophisticated systems such as radar guided crash avoidance programs that scan the roads for impending danger are also becoming available in more expensive executive and luxury vehicles. Passive safety serves to protect the occupants once a collision is inevitable so as to minimise the chance of injury or fatality. Such examples of passive safety include seatbelts and bolsters, airbags, and energy absorbent or dissipative structures in a vehicle chassis as illustrated in Figure 1.3. The highest strength steel in a Volvo XC60 surrounds the occupant compartment, which provides passengers with the best possible protection against side impacts and rollover type crashes, whilst the steel with lower strength is placed in regions where crumpling is desirable to absorb energy during a crash such as the engine bay during a frontal impact. Active safety implements are the first defence to a collision as they are preventive measures, and are receiving as much attention by car manufacturers as passive safety.

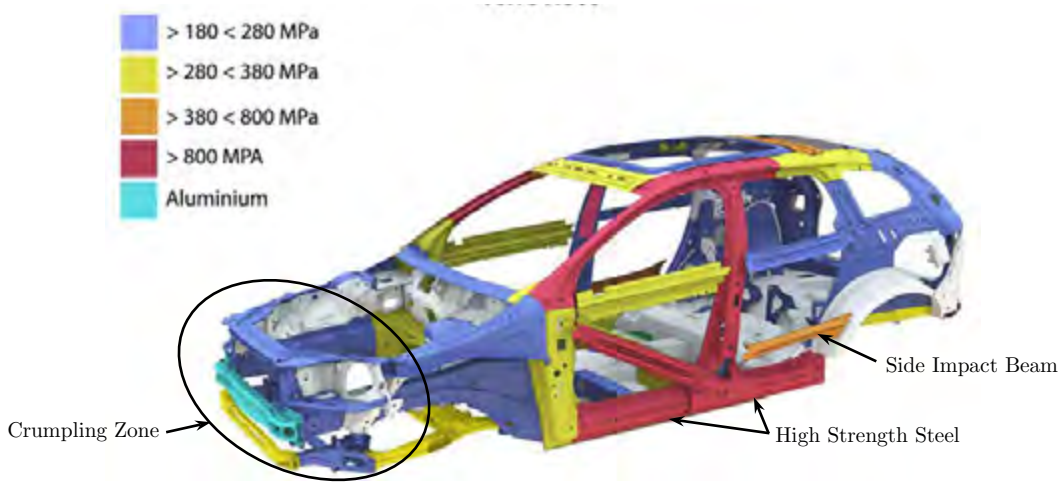

Figure 1.3: Volvo XC60 ('09-'14) chassis with different strength components [14].

1.1.3 Motivation for the study

An automobile accident comprises of three stages, as listed in Table 1.2, of which fatal injury is likely to occur from stages two and three. To improve the survivability of stages two and three it is imperative that the vehicle structure is sufficiently strong to minimise intrusion into the occupant cell. It is also important that the structure not be too rigid as this would cause accelerations as a result of the collision to be too high for the human body to survive.

Table 1.2: The three stages of an automobile accident.

Stage	**Description**
1	Collision between the vehicle and obstruction
2	Occupants collide with internal parts of the car (i.e. airbag, seatbelt, and upholstery)
3	Internal organs striking the skeletal structure of the human body

Frontal impact has received significant attention as it is the most common mode of accident. In contrast to frontal impacts, side impacts are more difficult to protect occupants against as there is less space for the chassis to crumple and absorb energy. As a result, side impact protection is focussed more on dissipating the energy around the occupant whilst minimising intrusion into the occupant compartment.

1.2 Thesis Objectives and Outline

This thesis presents the results of an experimental and numerical investigation on the response of side impact beams located in the front door of a passenger vehicle to an impact load. The purpose of this investigation was to determine the effect of changing geometric parameters on the behaviour of a side impact beam in a lateral collision, with a focus on Crash Force Efficiency (CFE), transverse deflection, and Specific Energy Absorption (SEA). The objectives of this thesis are:

i. Modelling of a passenger car subjected to side impact
   a. Implement a numerical model of a vehicle subjected to a side impact, in close conformation to the Federal Motor Vehicle Safety Standard 214 (FMVSS 214) [15] to obtain the transient behaviour of the door during impact for the purpose of determining appropriate initial conditions (striker mass and impact velocity) and boundary conditions (support structure design) for a simplified model.

ii. Isolate and validate the vehicle door model
   a. Design and construct a test rig to support the front side door of a light weight passenger vehicle in a vertical drop tester and carry out experiments to validate the finite element model of the door when struck with a rigid pole.

iii. Modelling and optimisation of a Side impact beam
   a. Characterise materials using Scanning Electron Microscopy (SEM), and a lateral tube compression test for the purpose of validating a side impact beam model.
   b. Develop a numerical model to reproduce the lateral tube compression test for the purpose of computing the material parameters to be used in the side impact beam model.
   c. Design and build a test rig for supporting square and round tubes in the vertical drop tester, of similar length and size to the side impact beam located in the front side door of a sedan.
   d. Develop a numerical model which reproduces the experimental transverse tube impact test as per (c), for the purpose of obtaining the friction coefficient parameters.
   e. Conduct a parametric study on different singular and compound tube geometric configurations to determine the effect of tube length, thickness, and material type on the transverse deflection, CFE and SEA.
   f. Compare the results, and re-implement the best compound tube configuration in the numerical model of a vehicle subjected to side impact.

iv. Draw conclusions and recommendations based on the findings of this study.

A literature review on the different testing methods, mandatory and voluntary, used by different regulating authorities in the automotive industry on side impact collisions are reported in Chapter 2. Additionally, studies relevant to this project are discussed in the literature review. This is followed by a discussion of different post-yield deformation modes in transverse beam loading, material characterisation techniques, and different commercially available finite element programs already

used in similar studies. The process of characterising the mechanical properties of materials in finite element analysis involves the selection of the correct material model. Material models applicable to this study are discussed and weighed against each other, followed by the selection of the most appropriate model.

The experimental methodology for the side door and impact beam tests as well as material characterisation are discussed in Chapter 3. This is followed by Chapter 4 which discusses the finite element models and analysis of the passenger car side impact tests, side door impact tests, and side impact beam tests. The results from experiments conducted for the purpose of developing the numerical models are also discussed in Chapter 4, along with the approach taken to obtain the material parameters from the experimental lateral compression tests.

A description and the results of a parametric study on different singular and compound tube configurations is presented in Chapter 5. The results from each configuration is compared in terms of transverse deflection, SEA and CFE. Finally conclusions are drawn and recommendations are made based on the findings of Chapter 4 and Chapter 5.

Chapter 2

Literature Review

This literature review is divided into several sections. Each section has its own underlying theory and is briefly discussed in this chapter. This literature review is laid out as follows:

2.1. Side Impact Structure in Passenger Vehicles
2.2. Industry Regulatory Bodies
2.3. Structural Impact Mechanics and Theory
2.4. Deformation Modes
2.5. Lateral Impact of Beams
2.6. Design Considerations for Side Impact Protection
2.7. Finite Element Programs used for Impact Loading
2.8. Material Models

2.1 Side Impact Structure in Passenger Vehicles

The structural components relevant to side impact protection are identified in Figure 2.1. In a side impact the obstruction strikes the outer shell of the door which then presses against the side impact beam or reinforcing structure which channels the energy into the door ring comprising outer rocker panel, A-pillar and B-pillar.

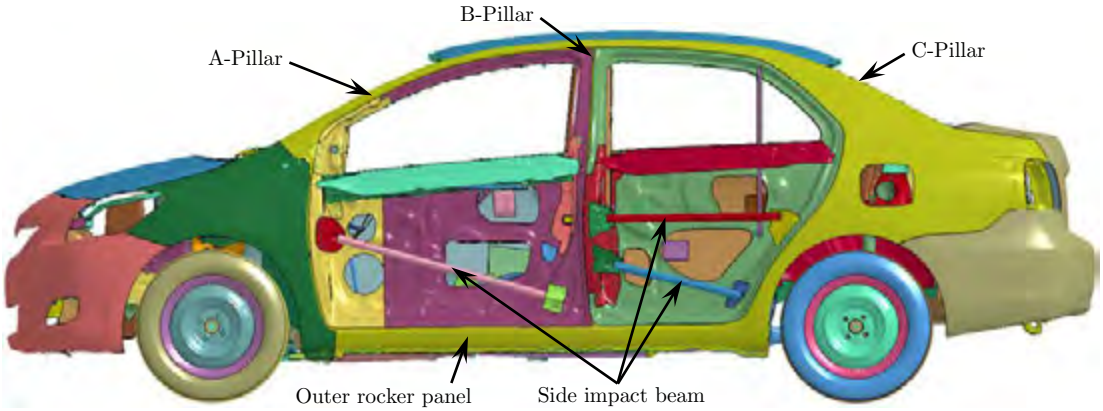

Figure 2.1: Vehicle occupant cell nomenclature for side impact protection.

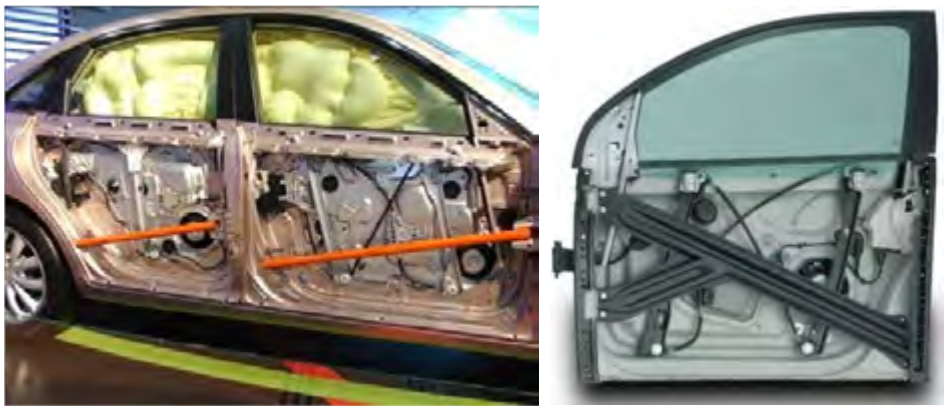

(a) (b)

Figure 2.2: Different types of anti-intrusion apparatus, (a) impact beam [16], and (b) corrugated steel. [17].

Car manufacturers use different anti-intrusion apparatus in side doors. Examples of such apparatus situated in typical passenger sedans are shown in Figure 2.2. These include side impact beams of different cross-sections such as square, diamond, and round tubes to name a few, sometimes solid, hollow, foam filled, or ribbed configurations. Tube structures are typically high strength steel with yield points upward of 800 MPa. In some vehicles, side and curtain airbags are also added in the door and A-pillar respectively, to provide a cushion between occupants and the interior of the vehicle.

2.2 Industry Regulatory Bodies

An increasing drive in the transport industry has led to the formation of several regional institutes and regulatory bodies such as the National Highway Traffic Safety administration (NHTSA), Insurance Institute for Highway Safety (IIHS) and European New Car Assessment Program (Euro NCAP) that have established guidelines and standards for automotive safety.

2.2.1 US Regulatory & Testing Bodies

The NHTSA was established by the Highway Safety Act of 1970 in a bid to improve safety on public roads in the United States [18]. The NHTSA establishes and regulates all vehicle safety standards in the US. The standard of particular relevance to side impact protection is the FMVSS 214, "Side Impact Protection". This standard was amended in 1990 by the US Department of Transportation (DOT) under the authority of the NHTSA to test the level of occupant protection in a crash that simulates a severe side impact collision using a Mobile Deformable Barrier (MDB) [18]. The safety standard was phased into new passenger vehicles from 1994-1997 with all passenger cars in production after 1997 and all Multi-Purpose Vehicles produced post 1999 required to conform to this standard.

Furthermore, the US DOT utilises the National Transportation Safety Board (NTSB) to provide a feedback loop on the state of safety on public roads in the US. The NTSB is an independent US government investigative authority primarily focused on investigating aviation accidents/incidents, as well as certain types of motor vehicle, maritime, pipeline and railroad accidents.

Auto insurers and insurance associations in the United States have additionally founded the IIHS, which is an independent, non-profit educational and scientific research organization which focusses on reducing injuries, deaths, and damage to property resulting from crashes on public roads [19]. The organization shares and supports its mission through the Highway Loss Data Institute (HLDI) by means of published scientific studies and insurance data for human and economic costs as a result of ownership and operation of automobiles.

2.2.2 European Regulatory & Testing Bodies

The United Nations Economic Commission for Europe Regulation 95 (UN-ECE R95) is a legislative document regarding the approval of vehicles for the protection of occupants in side impact collisions with jurisdiction over the European Union. All new vehicles sold in the EU after 1997 must conform to this regulation.

Euro NCAP is a European Union (EU) backed Car Safety Performance Assessment Program founded in 1997 by the Transportation Research Authority for the Department of Transportation in the United Kingdom (UK) which closely follows the UN-ECE Regulation 95 in terms of test specification, driver crash test dummy and injury criteria [20]. Euro NCAP conducts a variety of tests including front, side, pole and pedestrian impact testing with qualitative outcomes described by means of a 5-star rating system, with star ratings described in Table 2.1 [21]. The effectiveness of passenger vehicles in side impact collisions is assessed in two laboratory tests, namely the Mobile Deformable Barrier (MDB) and rigid pole test [20].

Table 2.1: Different star systems of the Euro NCAP rating [21].

Stars	**Description**
☆	Marginal crash safety
☆☆	Nominal crash protection but lacks crash mitigation technologies
☆☆☆	Average to good crash protection but lacks crash mitigation technologies
☆☆☆☆	Overall good crash protection with option of additional crash mitigation technology
☆☆☆☆☆	Overall good performance in crash protection with well-equipped and robust crash mitigation technology

2.2.3 Comparison of European to US Side Impact Crash Tests

A comparison of US and European Testing Standards as used by the NHTSA and Euro NCAP respectively, are provided in Table 2.2. The US testing standard for MDB side impact tests is more severe than the European standard largely because the mass of the average American vehicle is considerably more than European vehicles, which warrants a larger face width. The impact angle in the US standard is also more representative of a typical T-bone type side impact between two vehicles as the vehicle struck in the side is usually not stationary when the impact occurs.

Table 2.2: Comparison of European and US test conditions for side impact testing [22].

Description	**European Test**	**US Test**
MDB Mass	950 kg	1367 kg
Impact Angle	90°	63°
Impact Velocity	50 km/h	54 km/h
Impact Point	Centred on R-Point[1]	940mm from wheelbase centre
Barrier Face Ground Height	300 mm	280 mm Bumper 330 mm
Face Width	1500 mm	1676 mm
Barrier Material	Performance Defined	Aluminium Honeycomb
Crash Test Dummy	Euro-SID-1	SID
Support structure & work zone traffic control device testing	Only small car tested	Small car and light truck tested
Windshield damage criteria	Subjective/Qualitative	Objective/Quantitative
Vehicle rebound in crash cushion tests	None	Required

[1] Same as seating reference point.

2.2.4 Comparison of Automotive Safety Bodies

The pole test is considered more severe than the MDB side impact tests as the contact area of the striking face is considerably smaller and rigid in comparison to that of a deformable face found on an MDB. Similar to Euro NCAP, other car safety performance assessment programmes exist such as ANCAP [23] used in Australia and New Zealand, Latin NCAP [24] used in Latin America, as well as C-NCAP [25] used in China[2]. All of these voluntary and regulatory automotive safety bodies serve a common goal to improve the safety of vehicles on public roads. In 2010 the Australian government proposed the harmonisation of crash test procedures to the UNECE technical regulation [26]. The motivation was brought forth in a bid to reduce design costs for car manufacturers associated with designing to double safety standards depending on the different markets for which the product is intended. The proposal for the harmonisation of crash test procedures is under the authority of the World Forum for Harmonisation of Vehicle Regulations WP29 of the Transport Division of the UNECE. To date, 58 countries have signed the agreement with the notable exception of the US and Canada. Table 2.3 shows a comparison of the different regulatory and voluntary standards laid out by these automobile safety bodies across the world. All standards comply with the 254 mm rigid pole setting.

Table 2.3: Salient differences in global regulatory and voluntary side pole impact testing procedures [26].

	Impact Angle	**Impact Velocity**	**Dummy**	**Comments**
Regulatory				
US FMVSS 201	90°	29 km/h	SID H3 (50th percentile male)	Phasing out
US FMVSS 214	75°	26-32 km/h	ES-2RE (50th percentile male)	Phasing in
			SID-IIs (5th percentile female)	Phasing
Voluntary Standards - NCAPs				
U.S. NCAP	75°	32 km/h	SID-IIs (5th percentile female)	
Euro NCAP	90°	29 km/h	ES-2 (50th percentile male)	
KNCAP	90°	29 km/h	ES-2 (50th percentile male)	
ANCAP	90°	29 km/h	ES-2 (50th percentile male)	
JNCAP	No test			
Latin NCAP	No test			

[2] For the purposes of this study only the European and US equivalent testing standards, used by Euro NCAP and the NHTSA respectively, are discussed and compared. For more information about ANCAP, Latin NCAP, and C-NCAP kindly refer to [15], [16] and [17] respectively.

The WorldSID taskforce in collaboration with the NHTSA conducted tests in accordance with the 10 point ISO TR9790 biofidelity rating system and reported that the WorldSID 50th percentile male performed considerably better than any other side impact crash test dummy, scoring 8.0 out of 10 [26]. The ES-2 50th percentile male and the ES-2RE 50th percentile male did not perform favourably well as it scored 4.7 and 4.2 respectively [26]. One particular finding from the tests was that shoulder design considerably affected the response of the crash test dummy to the impact through interaction with the curtain airbags [26]. The WorldSID 50th percentile male dummy performed considerably better than the rest. [26]

2.3 Structural Impact Mechanics and Theory

Structural impact mechanics deals with the response of any physical structure to large dynamic loads that result in a range of failures such as permanent deformation or damage such as tearing [27]. Structural impact mechanics is a knowledge base used in applications ranging from design to maintenance or accident investigations. The severity of the impact is determined by factors such as the striking velocity, as well as the mass, geometry, and material characteristics of the struck and striking bodies [28].

Impact algorithms typically make use of the strain energy imparted on the material as a result of impact between two bodies. The strain energy is a function of the work done on the deformable structure through deformation which is based on the applied load, resulting elongation and distribution of stress, and is obtained by integrating over the volume of each element [29]. The equation defining the strain energy is given in Equation 2.1 [29].

$$U_e = \frac{1}{2}\int_v \sigma \times \varepsilon \times dv = \frac{1}{2} K_{eq}.\delta_{max}^2 \tag{2.1}$$

To quantify the relative performance of different anti-intrusion beams on their crash behaviour certain performance indicators are used. One such example is CFE, which is defined as the ratio between the mean and maximum loads over the duration of impact for a given structure, described in Equation 2.2 [30].

$$\eta(\delta L_{max}) = {P_{avg}(\delta L_{max})}\Big/{P_{max}(\delta L_{max})} \tag{2.2}$$

The crash force efficiency is an important performance criterion as it dictates how regular the Energy Absorption (EA) takes place over the duration of impact. The smaller the difference between the mean to the maximum load the more gradual the deceleration of the structure. Equation 2.1 leads to the definition of the second performance indicator called the Specific Energy Absorption (SEA).

The SEA is a measure of a structures ability to absorb energy through deformation per unit of mass, as given in Equation 2.3 [30].

$$SEA = \frac{U_e}{Mass} \tag{2.3}$$

In side impact collisions of a motor vehicle it is desirable to optimise the following parameters [30]:

- SEA is to be maximised whilst limiting cost,
- Intrusion/encumbrance into the passenger cell is to be minimised, and
- CFE is to be maximised.

The parameters described on Equations 2.2 and 2.3 may be combined together to produce a factorial combination, together with some other parameters, called the Synthetic Performance Indicator 'y' (SPI), given in Equation 2.6 [30]:

$$y(\delta L_{max}) = \frac{SEA(\delta L_{max}) \cdot \eta(\delta L_{max})}{W \cdot \delta L_{max}} \tag{2.4}$$

where 'W' is the lateral encumbrance and the SPI is measured in $[kN \cdot kg^{-1} \cdot mm^{-1}]$

Another metric for comparing the efficiency of tubes with different geometries and material compositions, called the dynamic energy-absorbing effectiveness factor, suggested by Jones [27] (based on axial impact of tubes, although may be used in transverse impact), is given in Equation 2.5. The energy-absorbing effectiveness, given in Equation 2.5 [27], is defined as the quotient of the total energy absorbing capability of the system to that of a specimen of the same volume subjected to a simple uniaxial tensile test [27]. It is thus a measure of the amount of energy absorbed by a particular geometry with reference to the total energy absorbing capability of the material used in the structure.

$$\bar{\psi}' = \frac{3GV_0^2}{8\sigma_0 A \delta_f \epsilon_r} \tag{2.5}$$

where G is the striking mass with initial velocity V_0, and σ_0 is the mean flow stress of the material, described by $\sigma_0 = (\sigma_y + \sigma_u)/2$. σ_y and σ_u are the uniaxial tensile yield stress and Ultimate Tensile Strength (UTS) of the material respectively [27]. A is the cross-sectional area of the thin-walled structure, δ_f is the deflection at failure, and ϵ_r is the strain at rupture for the material [27].

2.3.1 Energy and Momentum Conservation

The interaction between the striker and impacted structure is governed by two principles, namely, momentum or energy conservation. Typically the principle of energy conservation is used when three criteria are met, namely:

- The inertia of the impacted structure is negligible in comparison to the striking object,
- The two striking objects do not separate after impact [31] (inelastic collision), and
- No energy is dissipated in the form of heat, sound or any other form of radiation, chemical or nuclear reaction.

If the inertia of the impacted structure is not negligible or any part of the two objects separate after impact the conservation of momentum is used [31]. The equations describing the above two conservation principles are given in Equations 2.6 and 2.7.

$$\frac{1}{2}m_p v_p^2 = \frac{1}{2}\left(m_p + m_d\right)v^2 + \frac{1}{2}K_{eq}\delta_{max}^2 \tag{2.6}$$

$$m_p v_p = m_p v_p' + m_d v_d' \tag{2.7}$$

Both Equations 2.6 and 2.7 assume that the impacted structure 'd' is stationary in the current reference frame prior to impact with the striking object 'p'.

2.4 Deformation Modes

The initiation of buckling of thin-walled structures from lateral impact loading results in one of two modes of deformation, namely lateral indentation or flattening in a localised region.

2.4.1 Lateral Indentation

When the compression and restitution phases of loading is dominated by the relationship between the contact force and local deformation of the two bodies in contact lateral indentation occurs [32]. This results in the formation of a dent which typically occurs in a localised region of a tube due to the application of a concentrated load. The illustration shown in Figure 2.3 shows the deformation resulting from the application of a concentrated load on a simply supported beam.

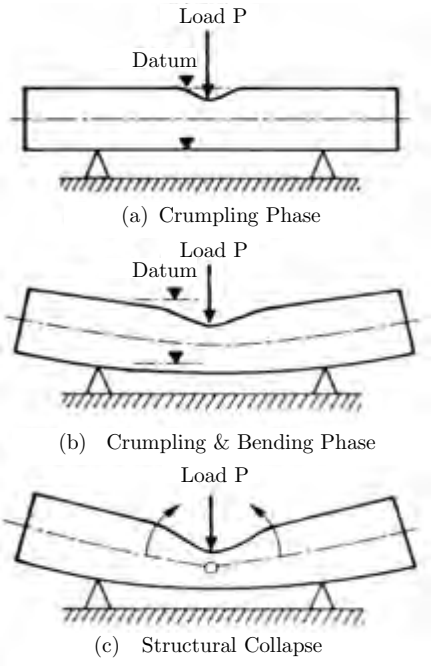

Figure 2.3: Progression of deformation of a laterally loaded beam [33].

The deformation shown in Figure 2.3(a) shows lateral indentation, which progresses into bending shown in Figure 2.3(b), followed by the onset of structural failure shown in Figure 2.3(c). Lu and Yu [32] describe two methods for determining the point of lateral indentation on a deformable isotropic homogeneous structure, these two methods are given by:

- Hertz Theory, and
- Winkler Foundation Model.

Hertz theory defines an equation for the relationship between contact area, contact pressure, and stress. [32]

$$a = \sqrt{\frac{4PR}{\pi E^*}} \tag{2.8}$$

where E^* is the equivalent modulus of elasticity, and R is the equivalent radius, defined in Equation 2.9. Young's modulus is defined as E, the radius of the tube and striker are defined as R_1 and R_2, and Poisson's ratio is defined as v. The maximum contact pressure σ_o is defined in Equation 2.10. [32]

$$E^* \equiv \left(\frac{1-v_1^2}{E_1}+\frac{1-v_2^2}{E_2}\right)^{-1} \qquad R \equiv \left(\frac{1}{R_1}+\frac{1}{R_2}\right)^{-1} \tag{2.9}$$

$$\sigma_o = \frac{2P}{\pi a} = \frac{4}{\pi}\sigma_m = \sqrt{\frac{PE^*}{\pi R}} \tag{2.10}$$

where σ_m is the mean normal pressure [32]. Complications arise in elastic contact stress theory used in Hertz Theory when determining displacements as it is a function of pressure which has a non-linear distribution over the cross-section. This complication can however be avoided by making use of the Winkler Foundation model [32]. The Winkler Foundation model assumes an elastic foundation onto which the cylinder is pressed as shown in Figure 2.4 as opposed to being modelled as an elastic half space as in the case of Hertz theory [32].

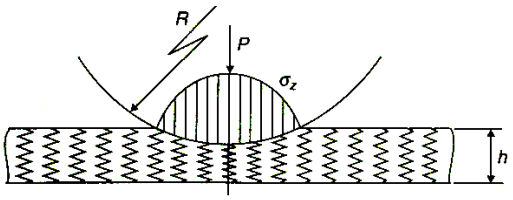

Figure 2.4: Rigid cylinder pressed onto a Winkler foundation [32].

The equation for the relationship between compression force P of a cylinder of radius R and the circular contact area a on an elastic foundation of depth h with elastic modulus k is given by Equation 3.2 [32]. The point at which the onset of yielding occurs between two cylinders is found by applying the Tresca failure criterion to the Winkler Model [34].

$$P = \frac{\pi}{4}\left(\frac{ka}{h}\right)\frac{a^2}{R} \tag{2.11}$$

A simple theoretical model for the indentation of a round tube due to a blunt wedge as illustrated in Figure 2.5 was formulated by de Oliveira et al. [35]. The model describes the relationship between the applied load P and the indentation magnitude δ [32].

$$P = \frac{4M_t}{D}\left\{\frac{\pi h \delta_p}{D^2}\left[1-\frac{1}{2}\left(\frac{N}{N_p}-1\right)^2\right]\right\}^{1/2} \tag{2.12}$$

and,

$$\xi = D\left\{\frac{\pi\delta_p}{4h}\left[1-\frac{1}{2}\left(\frac{N}{N_p}-1\right)^2\right]\right\}^{1/2} \tag{2.13}$$

where $N_p = \pi DhY$ is the fully plastic axial load in the tube and N is the axial force generated in the tube. D is the tube outer diameter and h is the thickness of the tube. The ratio N/N_p is set to 0 for free ends and 1 for fully constrained ends [32].

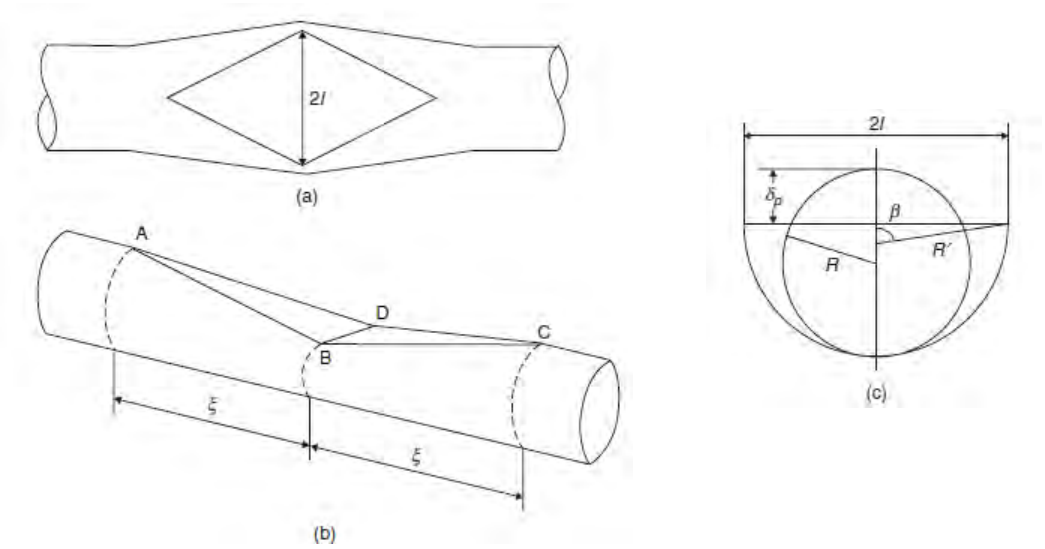

Figure 2.5: Indentation of a round tube by a wedge indenter (a) top view, (b) isometric view, and (c) cross-sectional view. [32]

Wierzbicki and Suh [36] improved on the model by de Oliveira et al. [35] by adapting the geometric deformation profile resulting from a wedge induced indentation [32]. The subsequent equations for the load P and characteristic length δ are given in Equations 2.14 and 2.15 [32].

$$P = 4Yh^2\left\{\frac{\pi D\delta_p}{3hR}\left[1-\frac{1}{4}\left(1-\frac{N}{N_p}\right)^3\right]\right\}^{1/2} \tag{2.14}$$

and,

$$\xi = \frac{D}{2}\left\{\frac{2\pi\delta_p}{3h}\left[1-\frac{1}{4}\left(1-\frac{N}{N_p}\right)^3\right]\right\}^{1/2} \tag{2.15}$$

The theory developed by Wierzbicki and Suh [36] was compared with experimental testing of 457 mm length simply supported beams under elastic-plastic and rigid-plastic assumptions as shown in Figure 2.6. The elastic-plastic theory assumes that there is a linear relationship between bending moment and curvature about which bending occurs provided that the bending moment is small. Rigid-plastic theory makes the assumption that plastic deformation exists predominantly at the hinge points. The elastic-plastic assumption was found to be in better agreement with the experiments than the rigid-plastic assumption.

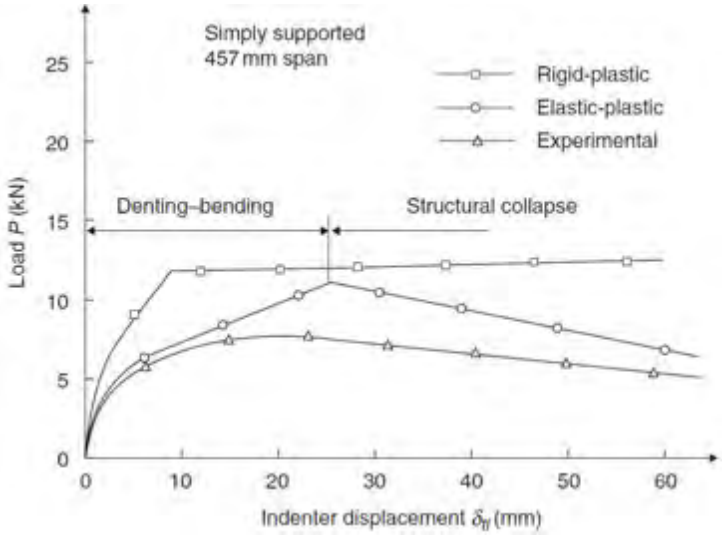

Figure 2.6: Simply supported theoretical and experimental load–indenter displacement curves [37], reproduced from Lu and Yu [32].

2.4.2 Lateral Flattening

Lateral flattening can be described as the measure of compression of a tube on an axis perpendicular to its longitudinal axis. Round tubes typically take an elliptical shape at the region of application of the transverse force. An example of lateral flattening is illustrated in Figure 2.7, where Figure 2.7(a) shows before, and Figure 2.7(b) shows after a lateral compression test. The unloaded tube takes a cylindrical form, after which the cross-section begins to deform into an ellipse. This is proceeded by two common modes of deformation, the first has four stationary plastic hinges forming a double Limaçon type profile, with bowing at contact points as shown in Figures 2.7(b) and 2.8(a). The second mode of deformation involves the straightening of the region of the tube in contact with the flat crosshead section, as illustrated in Figure 2.8(b). Both deformation modes initiate from the same loading diagram and equations. The equation describing the relationship between the load and bending moment at the contact point between the tube and crosshead is given in Equation 2.16.

$$\frac{1}{2}PRcos\theta = 2M_p \tag{2.16}$$

And the relationship between the deflection of the tube and size is given in Equation 2.17.

$$\delta = 2Rsin\theta \tag{2.17}$$

(a) (b)

Figure 2.7: Typical (a) before and (b) after lateral flattening by means of a typical lateral compression test [38].

Three different analytical formulations available for the analysis of round lateral tube compression are listed as follows:

- Limit Analysis as described by DeRuntz and Hodge [39],
- Plastica Theory as described by Reid and Reddy [40], and
- Moving Hinge Method as described by Sherbourne and Lu [41].

The limit analysis formulated by DeRuntz and Hodge [39] describes the failure modes of a round tube under lateral compression between two flat plates. Four plastic hinge mechanisms, as shown in Figure 2.8 are needed for the tube to collapse as shown in Figure 2.8. The configuration in Figure 2.8(a) is more applicable to materials with an upper and lower yield point such as mild steel.

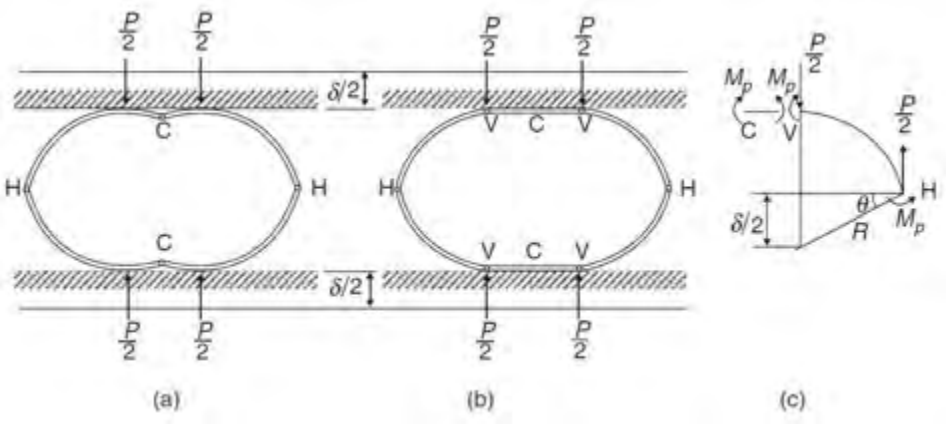

Figure 2.8: Failure mechanisms as described by (a) DeRuntz and Hodge [39], (b) Burton and Craig [42], and (c) loading diagram for both segments [32].

The Limit Analysis makes use of a perfectly plastic material model with a geometric component of stiffening. The equation governing the theory is given in Equation 2.18.

$$P = \frac{2Yh^2L}{D(1-(\delta/D)^2)^{1/2}} \tag{2.18}$$

where P is the applied load, Y is the yield stress (σ_y) for rings and $2/\sqrt{3}\,\sigma_y$ for longer tubes to account for the plane strain condition, h is the hinge length and L is the width of the tube. D is the intial diameter of the tube and δ is the crush distance. The limit analysis theory under underpredicts the force when compared with experimental results due to the perfectly plastic material assumption as shown in Figure 2.9. Redwood [43] proposed the adaptation of the perfectly plastic assumption by replacing the perfectly plastic material assumption with a linear hardening relationship. The linear hardening relationship was included using Equation 2.19:

$$M = M_p + E_p I\kappa = M_p\left(1+\frac{E_p\theta}{2Y\lambda}\right) \tag{2.19}$$

where I is the moment of inertia and E_p is the strain-hardening moulus of the tube material. Redwood [43] replaced M_p in Equation 2.16 with Equation 3.2, resulting in the linear strain hardening equation for tubes under lateral compression, given in Equation 3.2. This equation provides an improvement in the prediction accuracy over the perfectly plastic material model.

$$\frac{P}{P_o} = \frac{1}{[1-(\delta/D)^2]^{1/2}}\left[1+\frac{E_p}{3Y\lambda}sin^{-1}\left(\frac{\delta}{D}\right)\right] \tag{2.20}$$

The configuration shown in Figure 2.8(b), also known as the Moving Hinge Method is applicable when there is no lower yield point. It also takes into account contact conditions between the tube and flat crosshead surface where the hinge point shifts from the centre C in an outward direction as crush distance increases [44]. The Moving Hinge Method is an enhancement of the perfectly plastic material model.

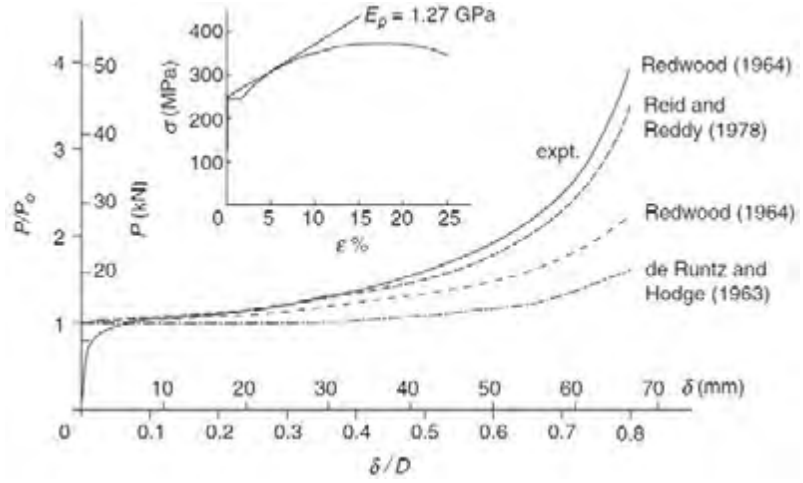

Figure 2.9: Non-dimensional force-deflection curves from experiment and different theories with $h/R = 0.108$, $R = 42.16\,mm$, and $L = 101.6\,mm$ [45].

Reid and Reddy [40] proposed the Plastica theory which uses a linear strain hardening material model similar to that of Redwood [43]. The Plastica theory formulation is given by Equation 2.21.

$$E_p I \frac{d^2\theta}{ds^2} = -\frac{P}{2} sin\theta \tag{2.21}$$

From where P can be obtained from Equation 2.22.

$$P = \frac{4M_p}{Rcos\gamma} \tag{2.22}$$

And,

$$\frac{\delta}{2} = Rsin\gamma - c \tag{2.23}$$

where γ, b, and c are defined in Figure 2.10, R is the tube radius before deformation begins, and M_p is defined as the initial plastic bending moment at B as shown in Figure 2.10. The Plastica theory

by Reid and Reddy [40] produces better results than the limit analysis. The Plastica theory best approximates the experiments of the three theories as shown in Figure 2.9, with the limit analysis with linear hardening material assumption performing second best. The perfectly plastic material model performed the worst as expected.

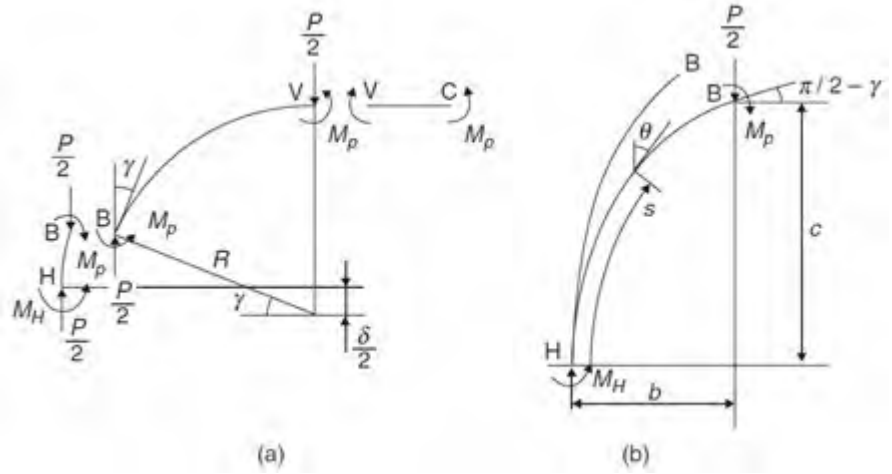

Figure 2.10: Strain-hardening tube material analysed with plastic theory as per Reid and Reddy [40] (a) forces on a quadrant of a tube in the HV region as per Figure 2.8 [32], and (b) deformation in the plastic region HB [32].

2.5 Lateral Impact of Beams

Strano et al. [30] conducted research into the design and manufacture of aluminium foam filled anti-intrusion beams. All tubes were subjected to 3 point bend tests with cylindrical Ø20 mm punch, 150 mm span between supports and constant crosshead rate of 500 mm/min. A photograph of the setup is provided in Figure 2.11. Each specimen was deformed by a maximum deflection (δl_{max}) of 48 mm, which corresponded to a vertex angle of 133° [30]. This was comparable with a maximum prescribed deflection of 120 mm for a real anti-intrusion beam as per the IIHS Side impact test program rating guidelines [46].

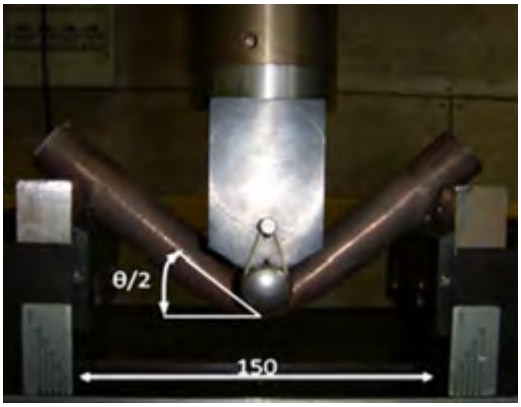

Figure 2.11: Arrangement of the three-point bending test by Strano et al. [30].

Square and round tubes were tested, some hollow, and others filled with foam. The foam was produced from an AlMg1Si0.6 alloy, by means of powder compaction followed by sintering [47]. The test conditions are shown in Table 2.4.

Table 2.4: Dimensions and conditions of tested tubes. Tested configurations are indicated by means of the symbol v, and untested configurations by means of an x [30] (reproduced from Strano et al.).

		Round Tube							**Square Tube**						
Abbrev.	**Materials**	**Ø [mm]**	**t [mm]**	**Experimental condition**					**L [mm]**	**t [mm]**	**Experimental condition**				
				AS	**HT**	**D**	**G**	**C**			**AS**	**HT**	**D**	**G**	**C**
LCS	Low carbon steel S235	27	2.5	v	v	v	v	v	20	2	v	v	v	x	x
INOX	Austenitic Stainless Steel AISI 304	25	1.5	v	v	v	x	x	x	x	x	x	x	x	x
HSS	High Strength Steel DOCOL 800 DP	32	2	v	v	v	x	x	30	1.5	v	x	v	x	v

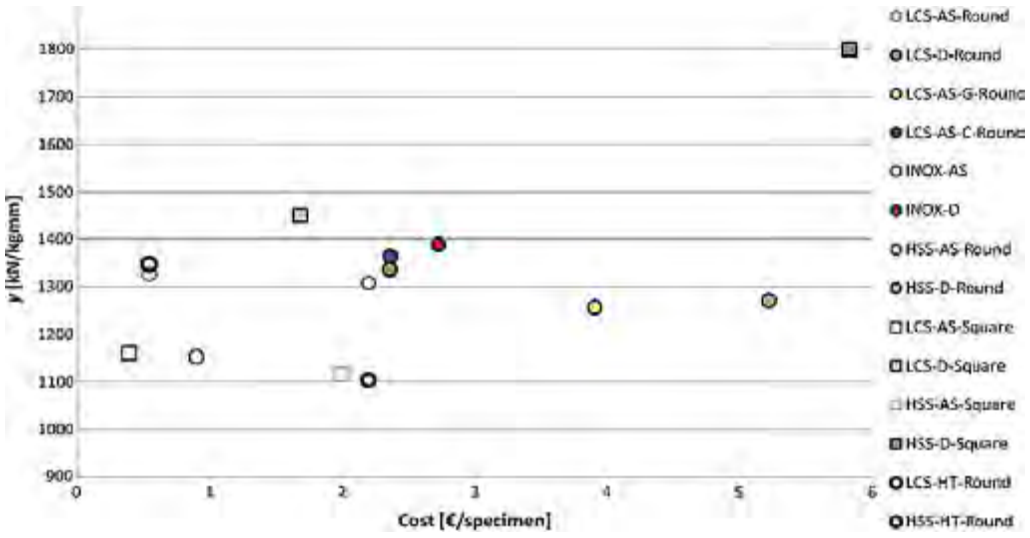

Figure 2.12: Synthetic performance indicator versus cost in Euro's as of 2013 [30].

The results of the synthetic performance indicator (SPI) versus cost per specimen of different configurations were plotted on a graph shown in Figure 2.12. The abbreviations in the legend refer to the following:

- INOX is Stainless Steel,
- HSS is High Strength Steel, and
- LCS is Low Carbon Steel.

The letters after the material refers to the following:

- D stands for directly foam filled tube (foam density of 560 kg/m^3),
- C stands for a tube filled with a core formed in a separate die such that there exists a small clearance between the foam and tube,
- G for gluing the foam which has been formed in a separate die, to the tube, (20 MPa shear strength of the glue at 20°C),
- The abbreviation AS refers to "As Received" from the suppliers, and
- HT refers to Heat Treatment after receiving the material.

The same thermal cycle was used to heat treat (HT) the hollow tubes as the foam filled tubes during the foam filling process. The tubes of particular interest were the LCS-AS-Round and LCS-HT-Round, as they possessed the best trade-off between cost and SPI. There appears to be less than a 2% increase in the SPI as a result of heat treatment of the tubes. Another observation of the plot in Figure 2.12 is that there was also approximately a 15% decrease in the SPI of the HSS tubes as a result of the heat treatment undergone due to direct foam filling.

Ghadianlou and Bin Abdullah [29] investigated the effect of adding different ribbed structures into round tube cross-sections. A purely numerical study was conducted on 4 different rib arrangements shown in Figure 2.13. However, validated material data was obtained from Grover [48]. Ghadianlou and Bin Abdullah [29] did not discuss validation of their models. The tubes were struck horizontally along the x-axis. The tubes were embedded within a side door and struck with a steel pole of mass 20 kg at 4 m/s [29]. The resulting internal energy plotted as a function of transverse deflection is plotted in Figure 2.14.

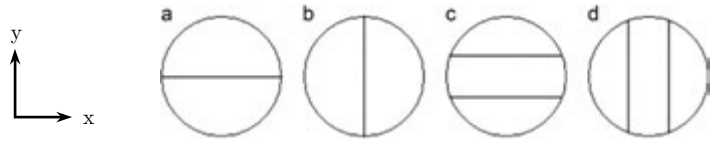

Figure 2.13: Four different arrangements of the inside ribs: (a) two-cell vertical, (b) two-cell vertical, (c) three-cell horizontal and (d) three-cell vertical [29].

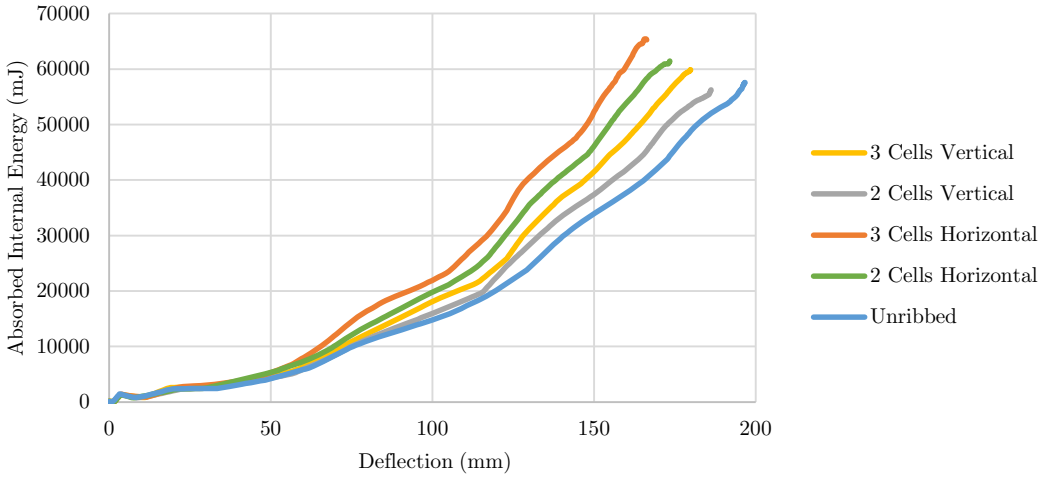

Figure 2.14: Absorbed internal energy versus transverse deflection for five different configurations [29] (Redrawn from Ghadianlou and Abdullah, with the tolerance within the line thickness of the original plots).

Plot points were obtained from time zero until the point of maximum deflection with all rebound data excluded from the plot. Each configuration indicated the maximum deflection of the bar/tubes. The results indicated that tubes with horizontal internal ribs perform better than their transverse counterparts, this may be attributed to a higher second moment of area about which bending occurred for the horizontal ribbed cells. The results also showed that more cells in the tube (I.e. Figure 2.13(c) and (d)) perform better, as with more cells there was more material to resist bending.

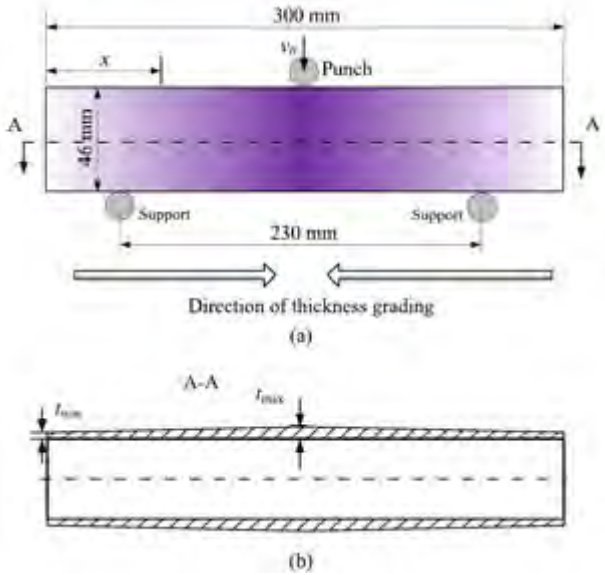

Figure 2.15: Schematic profile showing thickness grading pattern in the longitudinal direction: (a) Front view, (b) A-A cross-sectional view [49].

Sun et al. [49] reported on the analysis and optimisation of the dynamic bending behaviour of round Functionally Graded Thickness (FGT) tubes. The FGT tubes had a varying thickness from the longitudinal centre with maximum thickness at the centre as illustrated in Figure 2.15. The wall-thickness of the tube was varied as a function of position and gradient exponent m which was varied from 0-10 as given in Equation 2.24 [49].

$$t_f(x) = t_{min} + (t_{max} - t_{min})\left(\frac{2x}{L}\right)^m \tag{2.24}$$

The thin walled tube, made from an aluminium alloy AA6061, was subjected to a simple 3-point bend test. The test was modelled in LS-DYNA using Belytschko-Tsay reduced integration shell elements with 5 integration points through the thickness of the tube wall using the piecewise linear plasticity material model with rate effects ignored due to the rate insensitivity of aluminium [50]. The supports were modelled as a rigid material [49]. The tube material was characterised using a standard uni-axial tensile test [49]. The FGT tubes were benchmarked against same weight constant/uniform thickness (UT) tubes.

The results, shown in Figure 2.16, indicated that FGT tubes performed better in SEA, EA, and CFE but performed worse in maximum impact force. However, in the context of crashworthiness, SEA is the most significant indicator of an energy absorbing member for automobile designers. Functionally Graded Thickness tubes were, thus, found to perform better than their equivalent uniform thickness tubes in lateral impact tests under the conditions.

A similar study using Functionally Graded Foam (FGF) in square tubes was conducted by Fang et al. [51]. Two grading patterns as illustrated in Figure 2.17 were assessed. Kriging (a probabilistic mathematical tool), and a Multi-objective particle optimisation (MOPSO) algorithm were integrated to conduct an optimisation study. The equation describing the grading pattern is given by Equation 2.25 [51].

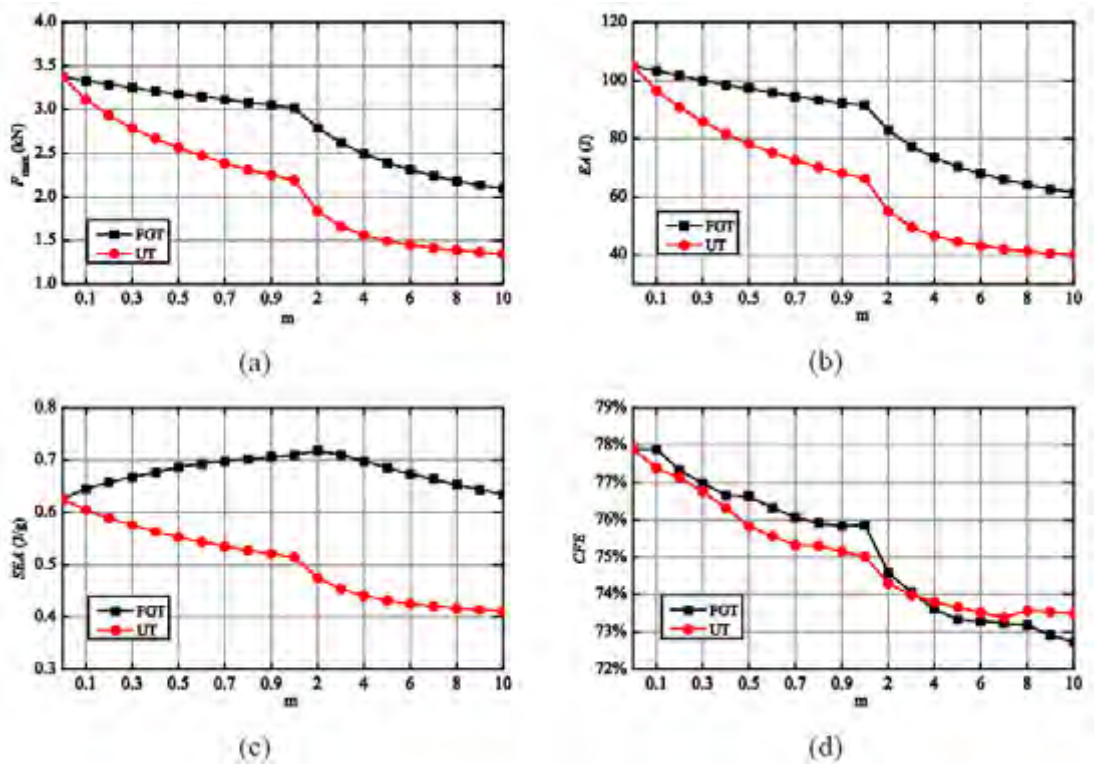

Figure 2.16: Energy absorption versus gradient exponent 'm' of FGT and UT tubes: (a) F_{max}, (b) EA, (c) SEA, (d) CFE [49].

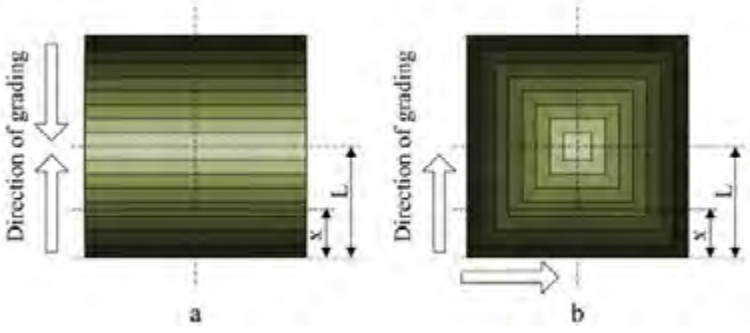

Figure 2.17: Schematic of the two grading patterns in the transverse direction [51].

$$\rho_f(x,m) = \begin{cases} \rho_{min} + (\rho_{max} - \rho_{min})\left(\frac{x}{L}\right)^m & \text{for ascending pattern} \\ \rho_{max} - (\rho_{max} - \rho_{min})\left(\frac{x}{L}\right)^m & \text{for descending pattern} \end{cases} \quad (2.25)$$

Kriging is a probabilistic mathematical tool which functions as a surrogate model to provide an expected output value and uncertainty at all untrained points. The equation describing Kriging is given in Equation 2.26.

$$\hat{y}(\boldsymbol{x}^*) = \sum_{j=1}^{k} \beta_j f_j(\boldsymbol{x}^*) + Z(\boldsymbol{x}^*) \quad (2.26)$$

where $\beta_j f_j(\boldsymbol{x}^*)$ is the regression model and $Z(\boldsymbol{x}^*)$ is the stochastic process. The stochastic term represents the uncertainty of the approximation [52]. The Reduced Order Model (ROM) is trained from the results of the full order model at points which maximize the range of variation due to dynamic loading. The aluminium alloy AlMg0.5F22 tube walls were modelled with a bilinear elastic-plastic material model with strain hardening, to good agreement with the results from experiments. The tubes were struck with a cylindrical Ø50 mm object of mass 128 kg at a velocity of 4.4 m/s at mid-span in a simply-supported configuration as illustrated in Figure 2.18.

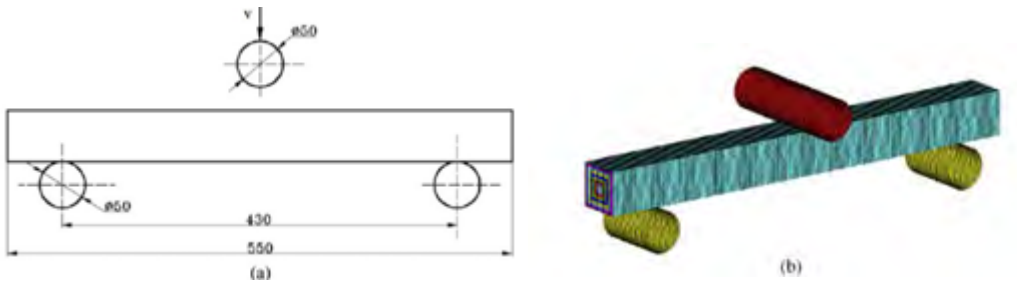

Figure 2.18: Square beam with functionally graded foam-filler: (a) schematic and (b) finite element model [51].

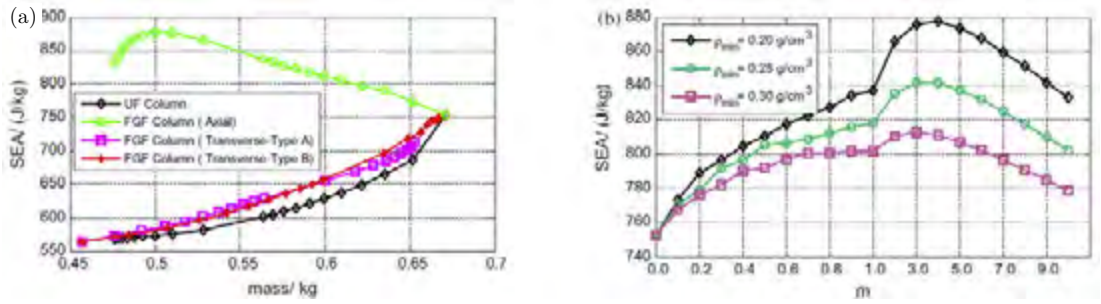

Figure 2.19: (a) Comparison of crashworthiness performance between FGF and UF filled tubes, and (b) crashworthiness performance due to variation of σ_y of tube wall [51].

When compared with their uniform graded counterparts the FGF tubes perform better under lateral impact for SEA, EA and CFE, but worse with maximum impact force [51] as observed by Sun et al. [49].

Studies have also been conducted on square tubes with different boundary or clamping conditions and different loading rates, by Jing and Barton [53]. Dynamic experimental tests were conducted at impact velocities of up to 6 m/s. The early version of LS-DYNA, called DYNA3D [54] was used to model the experiments for the purpose of attaining the velocity and force time histories of the experiments. The results for the experiments and simulations of the study by Jing and Barton [53] are shown in Figure 2.20.

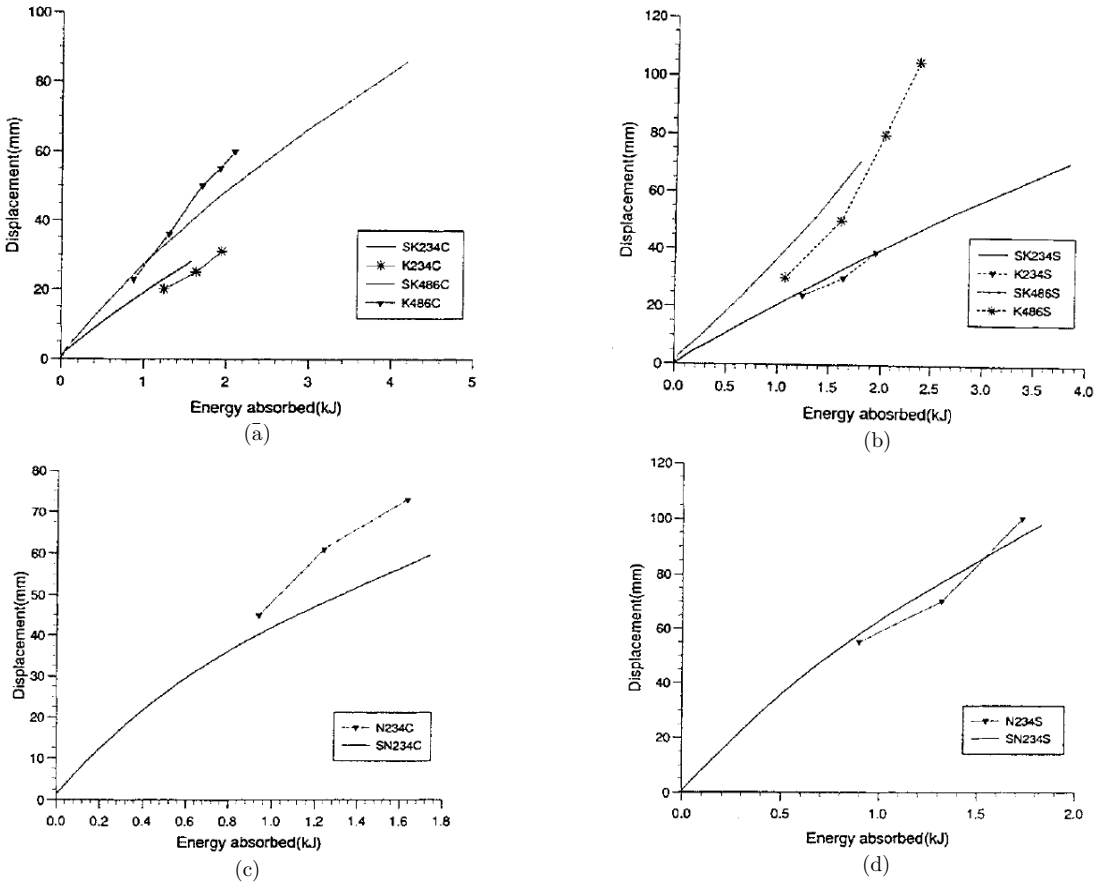

Figure 2.20: Displacement versus energy absorbed for (a) fully clamped thick-walled tubes, (b) simply supported thick-walled tubes, (c) fully clamped thin-walled tubes, and (d) simply supported thin-walled tubes [53].

The results for the relationship between the displacement and absorbed energy of four different boundary conditions, namely, fully clamped thick-walled tubes, simply supported thick-walled tubes, fully clamped thin-walled tubes, and simply supported thin-walled tubes are presented in Figure 2.20 [53]. They showed that there was a fairly regular increase in energy absorbed with increasing displacement. The clamped beams, described with a 'C' at the end of the label, were found to absorb more energy than their simply supported counterparts, described with an 'S' at the end of the label. The thick walled tubes, described with an 'N' in the label, were also found to absorb more energy than their thin walled counterparts 'N'.

Zarei and Kröger [55] conducted a parametric study on bending impact tests on Ø55 mm and Ø60 mm hollow and foam-filled aluminium tubes. Both numerical and experimental tests were conducted with the experiments used to validate the numerical model. Tubes of length 550 mm with thicknesses of 2, 3 and 4 mm were supported by two steel cylinders in a 3-point bend configuration as shown in Figure 2.21.

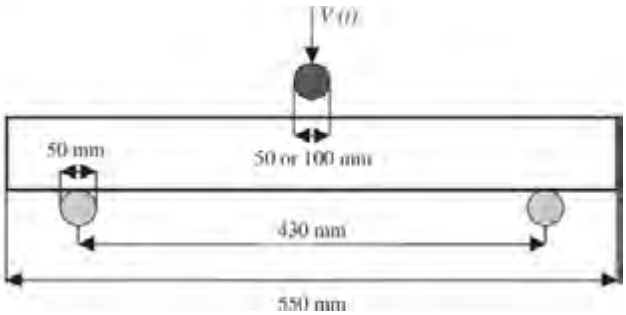

Figure 2.21: Boundary and loading conditions of impact bend tests conducted by Zarei and Kröger [55].

Two different striker diameters were considered, both of which struck the tubes in the longitudinal centres. An extruded 6060 aluminium alloy (AlMgSi0.5F22) with yield strength and ultimate tensile strength of 231 MPa and 254 MPa was used for the tube specimen. An Alporas aluminium foam produced by Shinko Wire with density of 230 kg/m^3 was used as the filler material for the foam filled specimens. An impactor of mass 20-300 kg was dropped from heights varying between 0.85-1.5 m as shown in Figure 2.22.

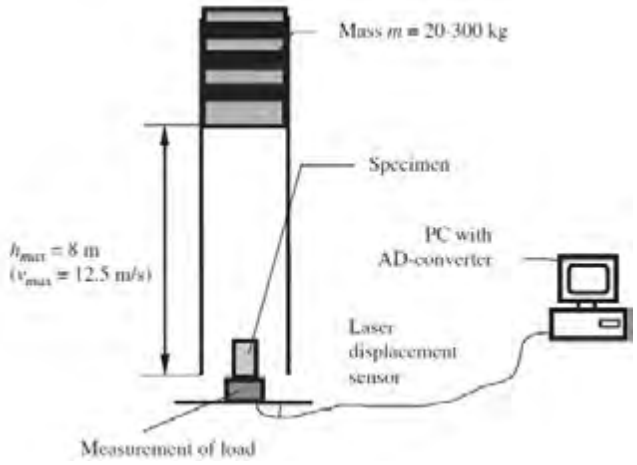

Figure 2.22: Test setup for experiments conducted by Zarei and Kröger [55].

Results from the experiments of the hollow (S) and foam filled (F) tubes are listed in Table 2.5. A comparison between the energy absorption capabilities of the hollow and foam filled tubes from the experiments are presented in Table 2.6. The results indicated that the energy absorbed by the foam filled tubes was higher than that of the hollow tubes as there was more material to absorb energy. A comparison of the SEA between the foam-filled and hollow tubes also showed that the foam filled counterparts performed better in all cases with an improvement of between 2.5-5.2%. The diameter "d" in Table 2.5 refers to the striker diameter, and the diameter "D" refers to the diameter of the tube.

Table 2.5: Experimental impact bend test results by Zarei and Kröger [48].

Test no.	d (mm)	V (m/s)	D (mm)	T (mm)	ρ_f (kg/m^3)	P_{max} (kN)	P_{60} (kN)
S1a	50	4.4	55	2	Unfilled	13.1	4.38
S1b	50	4.4	55	2	Unfilled	12.8	4.14
S2a	100	4.1	55	2	Unfilled	9.6	1.16
S2b	100	4.1	55	2	Unfilled	10.4	1.68
S3a	100	5.4	55	2	Unfilled	13.4	4.95
S3b	100	5.4	55	2	Unfilled	13.7	5.06
S5a	100	4.1	60	3	Unfilled	17.6	9.81
S6a	100	4.1	60	4	Unfilled	26.7	10.2
F1a	50	4.4	55	2	230	16.6	7.05
F1b	50	4.4	55	2	230	16.8	6.19
F2a	100	4.1	55	2	230	12.6	2.29
F2b	100	4.1	55	2	230	13.4	3.08
F3a	100	5.4	55	2	230	26.07	7.77
F3b	100	5.4	55	2	230	26.64	7.98

Table 2.6: Experimental energy absorption and specific energy absorption [55].

Test no.	EA (J)	SEA (J/kg)	SEA Improvement (%)
S1	432	687	-
F1	568	705	2.5
S2	227	361	-
F2	305	379	4.8
S3	468	744	-
F3	631	783	5.2

An illustrative comparison between the numerical and experimental results together with a crash force versus displacement comparison are shown for the hollow and foam-filled tubes in Figure 2.23. The comparison of force versus displacement curves for the experimental and numerical tests showed good correlation. A visual comparison of the experimental and numerical buckling showed similar behaviour. An optimisation to maximise the SEA involving tube thickness, diameter and foam density was conducted using the Response Surface Method (RSM). The wall thickness of the tube was allowed to vary between 0.5-3.5 mm, and the outer tube diameter was allowed to vary between 50-120 mm for both the hollow and foam-filled tubes. The foam density was allowed to vary within the limits of 60-540 kg/m^3. Optimised results are listed for the hollow and foam-filled tubes in Table 2.7. The energy absorbed for the optimised hollow tube was approximately 6 times higher than the S3 results. This is because the tube was 75% thicker with a diameter 40% larger for the optimised tube. SEA increased for the optimised configuration by approximately 260% over the S3 test. This is the most important metric as it takes the mass of the resulting configuration into consideration as well.

Table 2.7: Optimisation results for hollow and foam filled tubes [55].

	D (mm)	T (mm)	Pmax (kN)	E (J)	SEA (J/kg)	Increase in SEA (%)
Optimum hollow tube	77	3.5	50.9	3017	1949	
Optimum foam-filled tube	64	3.11	53.2	3028	2498	28.1

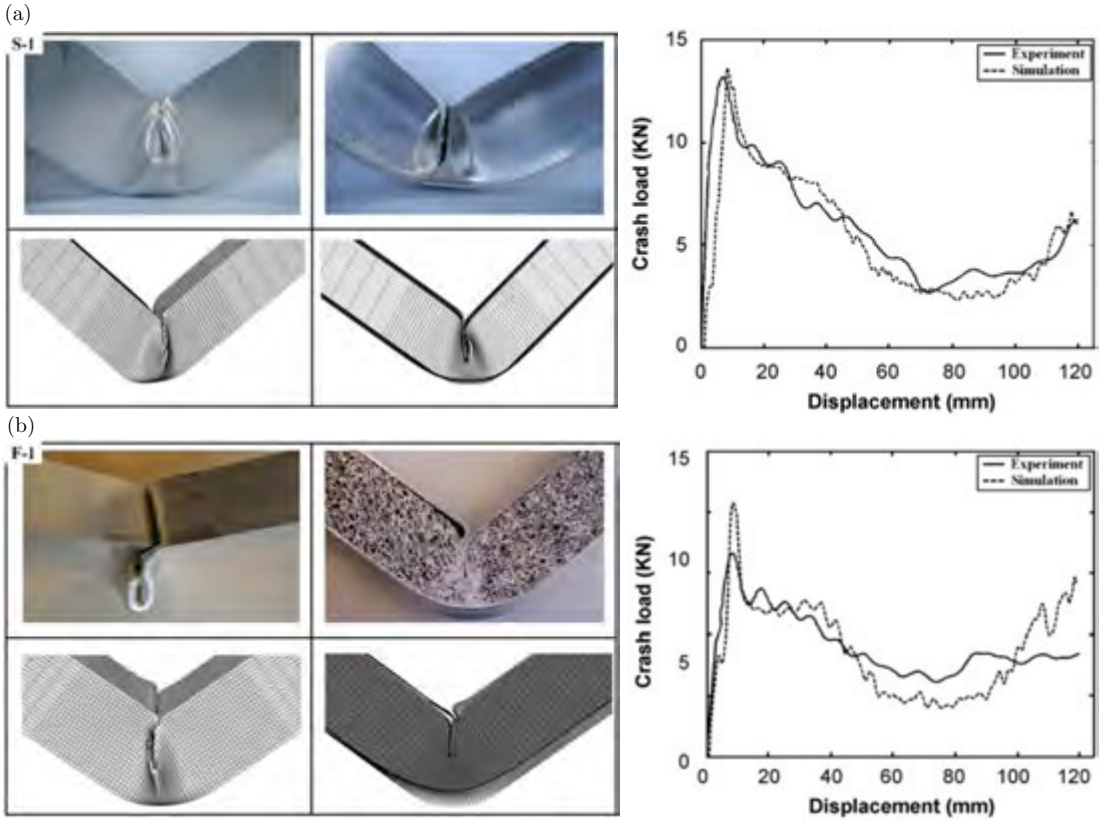

Figure 2.23: Experimental and numerical buckling behaviour and crash load–displacement curves of tests S1 and F1 for (a) hollow, and (b) foam-filled tubes respectively [55].

Husin et al. [56] investigated the effect of round side impact beam thickness and diameter on energy absorption in the front side door of a Proton Wira, a vehicle common to the Malaysian automobile market. The intent was to maximise the SEA whilst keeping the outer diameter within a range of 30-50 mm, and thickness within the range 1.0-3.0 mm. A Finite Element (FE) model of the side door structure and impact beam is illustrated in Figure 2.24.

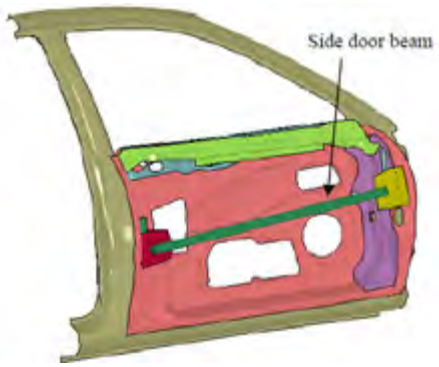

Figure 2.24: Side door structure of a Proton Wira as used by Husin et al. [56].

The tube length is 900 mm, and the structure was projected into a rigid vertical pole at 15 m/s. The material modelled was an aluminium alloy AA6061-T4. The variables were parametrised with 25 design cases fitted to a surrogate RSM model [56]. A quadratic ROM fit the results best with $R^2 = 0.9616$ after the elimination of less accurate linear and cubic models. The equation given by the RSM model is provided in 2.27 [56]:

$$SEA(a,t) = -4.4457 + 6.0882a + 4.1656t - 0.0868a^2 + 0.0523at - 0.779t^2 \quad (2.27)$$

where a is the outer tube diameter, and t is the tube thickness. A 3-Dimensional graphic of the specific energy absorption as a function of outer tube diameter and thickness is shown in Figure 2.25. The plot shown in Figure 2.25 shows that the SEA increased with tube thickness and was a maximum at an outer tube diameter of approximately 35mm.

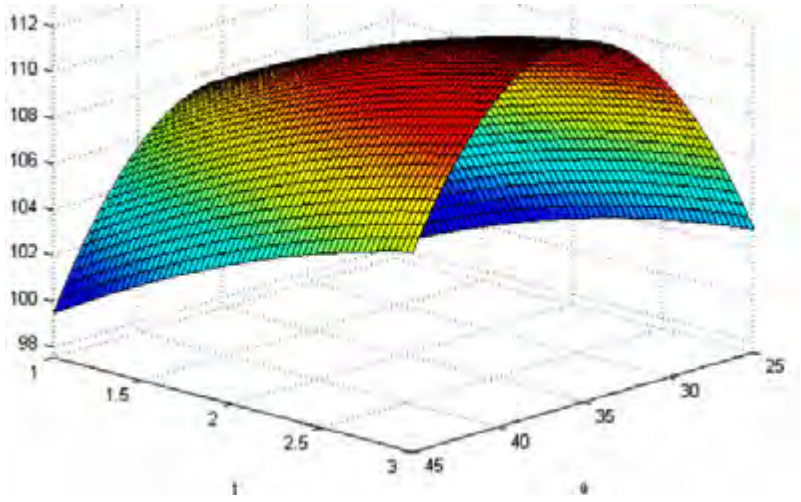

Figure 2.25: Quadratic response surface model of SEA for round side impact beam in a Proton Wira [56].

2.6 Design Considerations for Side Impact Protection

The design of a vehicle structure for side impact protection must take into consideration the interaction between separate components in the structure as shown by Harle et al. [57]. Harle et al. [57] investigated the feasibility of an optimising algorithm on the performance of a car structure design. The effect of individually varying the second moment of area of the B-pillar and rocker panels, as well as the axial stiffness of the floor panel on the overall performance of the structure was studied. The model consisted of approximately 3000 elements with an MDB crashing into the side door, outer rocker panel, B-pillar and floor of a passenger car.

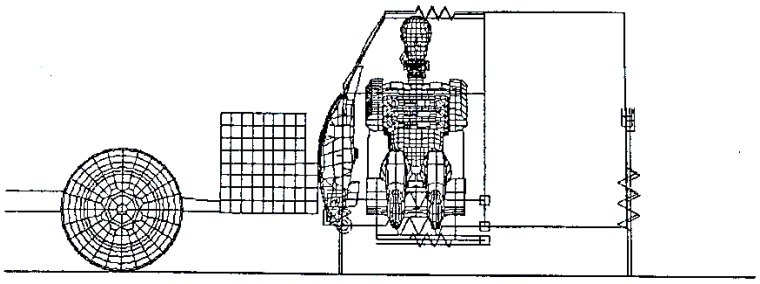

Figure 2.26: Finite element model of the side structure of a car with idealised spring mass damping system [57].

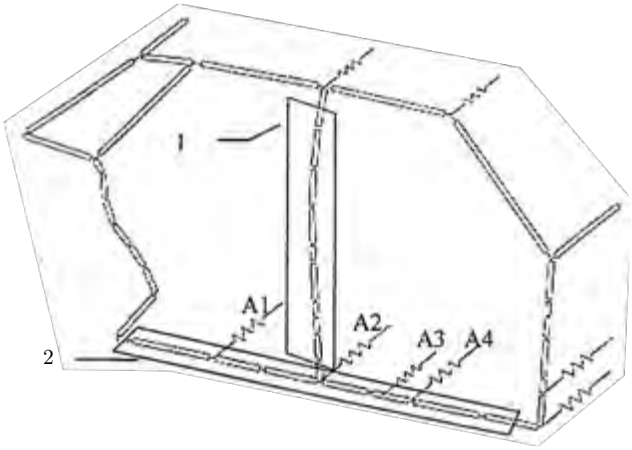

Figure 2.27: Design variables for optimisation routine of finite element model. The force versus deflection curves of axial members A1-A4 are scaled together, while the second moment of area of the beams in boxes 1 and 2 are independently varied. [57].

The design points were scaled with 3 factors, each ranging from 1-10. The order of the design points illustrated in Figure 2.27 are [Axial Members A1-A4, Beam 1, Beam 2]. The results from the design optimisation showed that greater deflections occur in the weakest members. The result of two design configurations is shown in Figure 2.28. The configuration in Figure 2.28(a) shows the deformation

mode for the baseline design points {1,1,1}. The resistance of box one to bending was increased to its maximum in Figure 2.28(b), with design points {1,10,1}. The result of design points {1,10,1} was that the mode of deformation changed with box deforming more. This demonstrated that the improvement of one component for side impact protection did not necessarily result in an improved design. Changing the design cases to {10,1,10} resulted in only a marginal reduction of intrusion into the occupant cell as shown in Figure 2.28(c). It was only with an improvement of every energy absorbing component, with design cases {10,10,10} that there was a significant reduction of intrusion into the occupant cell, as shown in Figure 2.28(d).

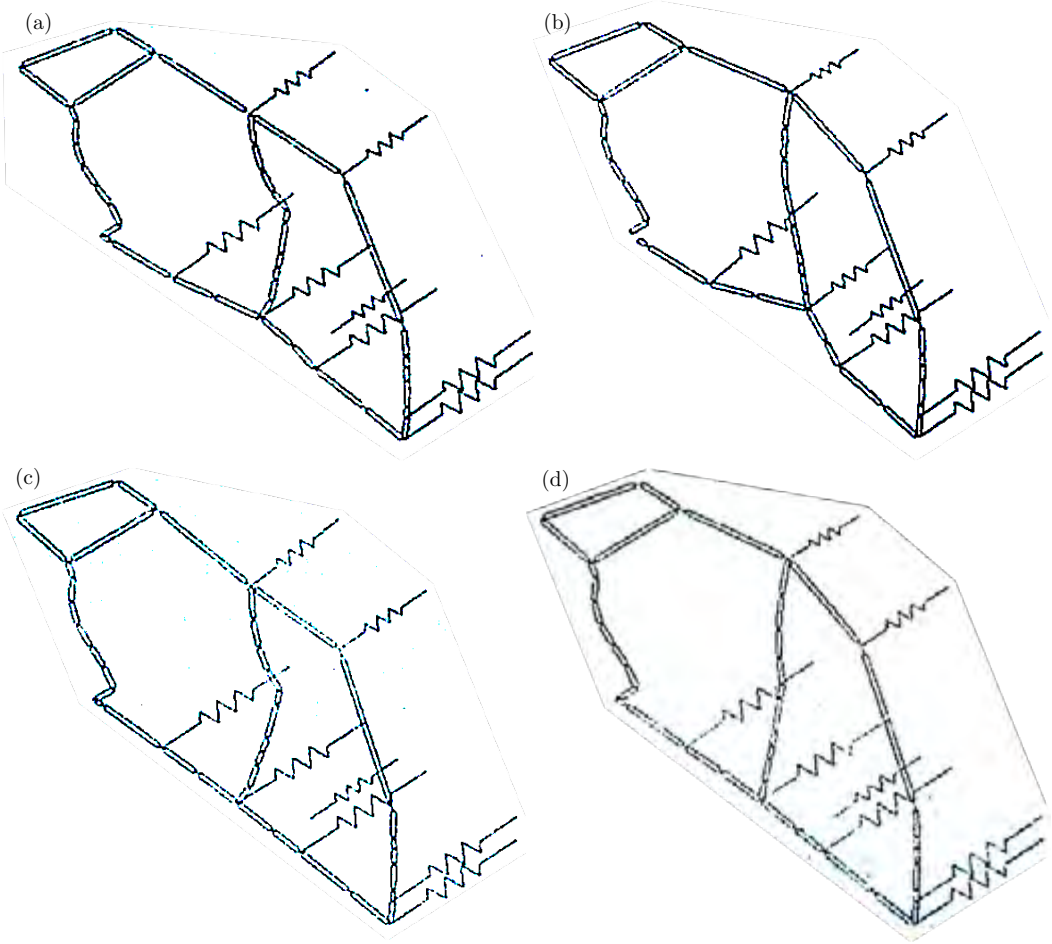

Figure 2.28: Collapse mechanisms for design points (a) {1,1,1}, (b) {1,10,1}, (c) {10,1,10}, and (d) {10,10,10} [57].

Harle et al. [57] identified that the human body collides with the internal panels of the car door in a side impact (with no airbags), hence the behaviour of those panels was used as a performance metric for the comparison of different design cases. Harle et al. [57] observed that strengthening the B-pillar delayed and reduced the initial velocity peak of the internal panels. It also resulted in a decrease in

the deformation of the internal panels of the vehicle. Strengthening only the rocker panel caused the B-pillar to hinge about its mid-point, while strengthening the B-pillar and rocker panel resulted in a lower broader velocity peak of the internal trim.

Marklund and Nilsson [58] conducted a study on the B-pillar from a SAAB 95 subjected to a T-bone impact with an MDB as shown in Figure 2.29(a). The crash test was setup in conformance with European regulation. A simplified B-pillar was modelled with time dependent boundary conditions as shown in Figure 2.29(b).

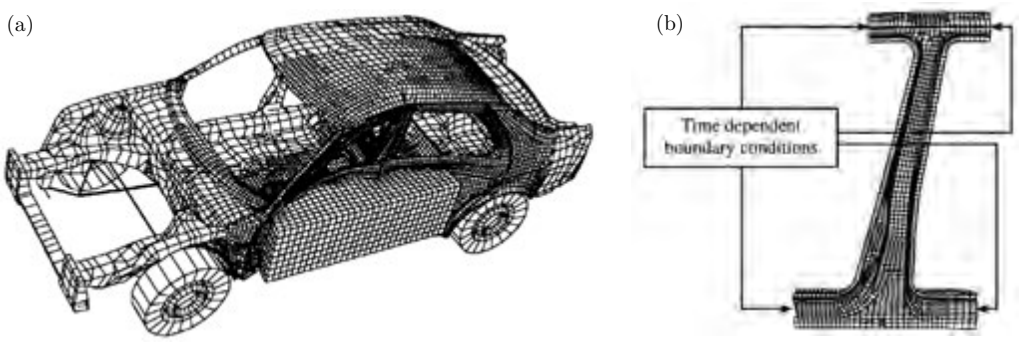

Figure 2.29: Finite element mesh of (a) full vehicle with MDB model, and (b) extracted B-pillar [58].

Marklund and Nilsson [58] performed geometric optimisation of a simplified B-pillar shown in

Figure **2.30** using the RSM algorithm. The optimisation objectives were to minimise the maximum velocities v_1, v_2 and v_3. The optimisation was setup to begin with $d_1 = d_2 = d_3 = 2\ mm$ and $d_4 = d_5 = d_6 = d_7 = 100\ mm$. Optimisation constraints used by Marklund and Nilsson [58] are given in Equation 3.2.

$$v_{1_{max}} \leq 3.5\ m/s \quad v_{2_{max}} \leq 5m/s \quad v_{3_{max}} \leq 3m/s$$
$$1\ mm \leq d_1, d_2, d_3 \leq 4\ mm \tag{2.28}$$
$$50\ mm \leq d_4, d_5, d_6, d_7 \leq 200\ mm$$

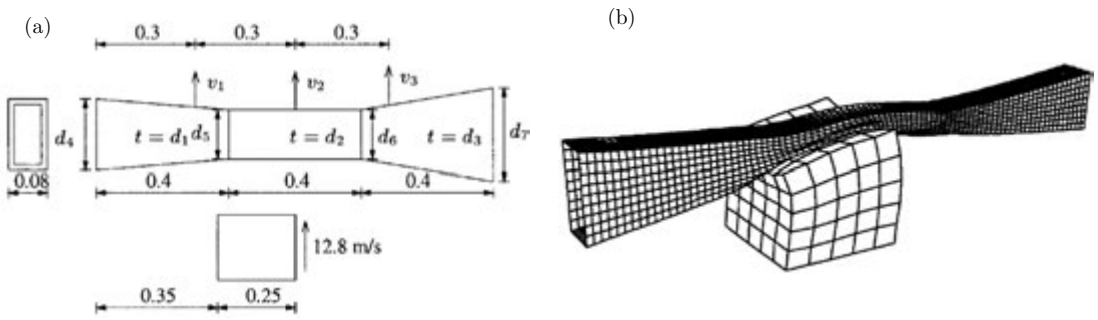

Figure 2.30: Simplified B-pillar geometry (in meters), and (b) simplified finite element model of B-pillar and MDB [58].

The optimised design parameters are shown in Table 2.8. The results showed that more material was required in regions d_4 and d_5 with widths of 155 mm and 161 mm respectively. Dimensions d_5 and d_6 were found to be 114 mm and 81 mm respectively. The thickness of the B-pillar material was set at 2 mm throughout its length for the first iteration. The optimisation found that the thickness in all three parts of the simplified B-pillar geometry reduced with the B-pillar having a thickness of 1mm in the centre. The thickness increased to 1.5 mm and 1.3 mm at the bottom and top tapers respectively. The optimised results are shown in Table 2.9. The results showed that all constraints were satisfied with a total B-pillar mass of 6.27 kg.

Table 2.8: Optimised B-pillar design parameters [58].

d_1 (mm)	d_2 (mm)	d_3 (mm)	d_4 (mm)	d_5 (mm)	d_6 (mm)	d_7 (mm)
1.5	1	1.3	155	114	81	161

Table 2.9: Results from the B-pillar optimisation study [56].

Mass	$v_{1_{max}}$	$v_{2_{max}}$	$v_{2_{max}}$
6.27 kg	3.42 m/s	4.79 m/s	2.65 m/s

2.7 Finite Element Programs used for Impact Loading

There are several commercial codes available for conducting finite element analysis (FEA) that have been used to analyse the behaviour of mechanical systems subjected to impact loading. A few examples of the successful implementation of different finite element codes employed include PAM-CRASH, used by Kim et al. [59], Njuguna [60] and Markiewicz et al. [61]; LS-DYNA used by Langseth et al. [62], Dietenberger et al. [63] and Olabi et al. [64]; ABAQUS explicit used by Belingardi et al. [65], Wu & Carney [66] and Lukman et al. [67]; RADIOSS used by Belingardi & Obradovic [68]; and MARC K6.2 used by Miyazaki et al. [69]. In most cases the explicit solver was employed for impact loads and other short duration simulations while the implicit solver was used for quasi-static type simulations. In both cases, multiple through thickness integration points of 4 noded quadrilateral or 3 noded triangular shell elements were used.

2.8 Material Models

The rate at which the component strains for some materials may have an effect on the results. This is due to the strain-rate sensitivity of the material. The strain rate domain is typically split into 3 categories, namely low or quasi-static strain rates (10^{-5} to $10^{-1}\ s^{-1}$), intermediate strain rates (10^{-1} to $10^{2}\ s^{-1}$), and dynamic strain rates (10^{2} to $10^{4}\ s^{-1}$). Materials loaded quasi-statically typically do not indicate any strain rate sensitivities. It is only in the intermediate or dynamic loading regime that materials appear harder or stronger than they did when loaded quasi-statically. Strain rates of 0.013 /s are experienced in humans during running by Lanyon et al. [70], and 0.05 /s during sprinting and downhill running by Burr et al. [71], whereas dynamic strain rates may be observed in structures subjected to explosions or bullets impacting objects.

Dietenberger et al. (2005) proposes five of many different material models for strain and strain-rate hardening in automotive crashworthiness applications [63]. These 5 models are as follows:

- Piecewise Linear Plasticity Formulation,
- Plastic Kinematic Hardening,
- Mixed Piecewise Linear plasticity with Cowper-Symonds Model,
- Simplified Johnson-Cook, and
- Zerilli-Armstrong.

These 5 models together with 2 other material models relevant to automotive crashworthiness are discussed in 0 to 0.

2.8.1 Piecewise Linear Plasticity Formulation

Of the 5 material models the piecewise linear formulation is the most widely used in automotive type applications [72]. In this model the stress-strain curve is made up of discrete data points, which unlike other models, does not first need to be fitted to some predefined equation. Rate effects are accounted for by defining a table of curves at different strain rates [73]. The strain rate is computed in each element of the finite element model and interpolated from the table of curves. If the computed strain rate is outside of the table of curves the value from the nearest available strain rate is used [73].

2.8.2 Plastic Kinematic Hardening (Cowper-Symonds)

The Cowper-Symonds model serves to incorporate rate effects to other material models which do not already include their own rate dependent parameters. The plastic kinematic hardening model scales the yield stress in accordance with the strain rate as per Equation 2.29. It is best suited for modelling isotropic and kinematic hardening.

$$\sigma_y = \sigma_0 \left[1 + \left(\frac{\dot{\varepsilon}}{C} \right)^{1/p} \right] \tag{2.29}$$

where σ_0 is the quasi-static yield stress, and C and P are experimentally determined constants. Typical values of coefficients C and P for different materials are given in Table 2.10.

Table 2.10: Coefficient and exponent values for the Plastic Kinematic Hardening equation in 2.29 [32].

Material	C (s^{-1})	P	Reference
Mild Steel	40.4	5	[74]
Aluminium Alloy	6500	4	[75]
A-Titanium (Ti50A)	120	9	[76]
Stainless Steel 304	100	10	[77]
High Tensile Steel	3200	5	[78]
Austenitic Steel X2CrNiN18-7/1.4318 1000<UTS[3]<1150	13889	5.57	[79]
Carbon Steel ZstE180BH	424	4.73	[80]

[3] Ultimate Tensile Strength (MPa)

2.8.3 Mixed Piecewise Linear plasticity with Cowper-Symonds Model

This material model differs from the piecewise linear plasticity model in that only one set of discrete data points defining a stress-strain curve is used in conjunction with the Cowper-Symonds equation to introduce rate effects. The data set is typically obtained at the lowest strain rate as is practicable with any rate effects introduced as a result of the test being offset by scaling the data. This reduces the number of experiments that must be conducted, provided that there is readily available information about the rate sensitivity of the material in literature.

2.8.4 Simplified Johnson-Cook

Simplified Johnson-Cook strain sensitivity plasticity model is used when strain rates vary over a large range [73]. This model does not include thermal and damage effects, which is more applicable when there are large temperature variations such as in explosive environments, or where tearing or some separation of elements is expected. Subsequently, this model has been reported to perform 50% faster than the full Johnson-Cook implementation [73]. The flow stress equation describing the relationship between stress, strain and strain rate used in the Simplified Johnson-Cook material model with the Cowper-Symonds rate operator is given in Equation 2.30.

$$\sigma_y = \left(A + B\bar{\varepsilon}^{p^n}\right)(1 + C ln\dot{\varepsilon}^*) \tag{2.30}$$

where A, B and C are empirically derived constants, $\bar{\varepsilon}^p$ is the effective plastic strain, $\dot{\varepsilon}^*$ is the normalised effective strain rate which is given by $\dot{\varepsilon}^* = \frac{\dot{\varepsilon}}{EPS0}$. There are however other available rate operators such as the log-linear Johnson-Cook equation, Huh & Kang, or the Allen, Rule & Jones equation [73]. A comparison between the different rate operators is illustrated in Figure 2.31.

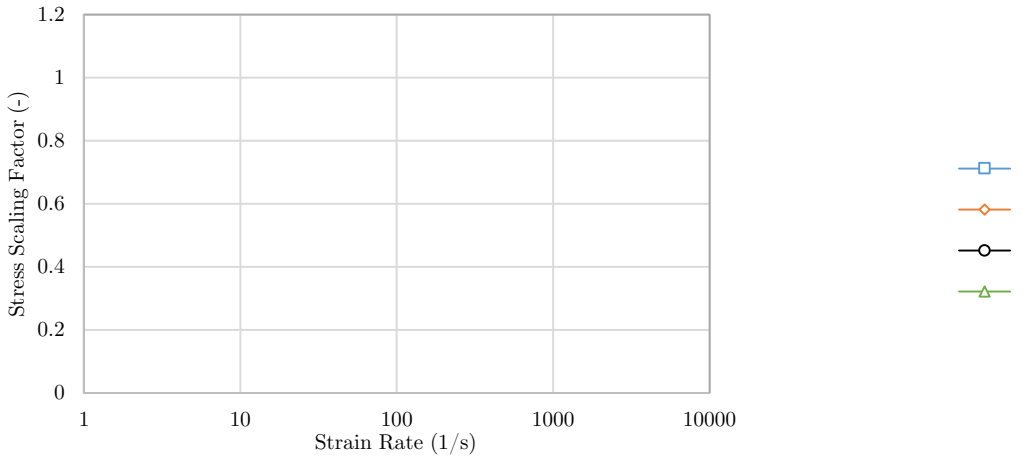

Figure 2.31: Comparison between the different rate operators available to scale the stress in accordance with the computed strain rate in each element.

The Cowper-Symonds formulation is the most common approach to including rate effects, however one may consider the log-linear or Allen, Rule & Jones formulation if it is known that the strain rate will always be above 1 /s as these 2 formulations require less Floating Point Operations Per Second (FLOPS) to compute during each iteration.

2.8.5 Zerilli-Armstrong Material Model

As with the Johnson and Cook material model the Zerilli-Armstrong model accounts for rate and temperature effects in an isotropic material. It is expressed in Equation 2.31.

$$\sigma = C_1 + \left\{C_2(\varepsilon^p)^{1/2}\left[e^{[-C_3+C_4 ln(\dot{\varepsilon}^*)]T}\right] + C_5\right\}\left[\frac{\mu(T)}{\mu(293)}\right] \tag{2.31}$$

where ε^p is the effective plastic strain and $\dot{\varepsilon}^*$ is the effective plastic strain rate. The constants C_1 through C_5 are all empirically determined flow stress coefficients.

2.8.6 Power-Law Plasticity Model

This is an isotropic plasticity model which accounts for rate effects using the Cowper and Symonds model which scales the yield stress. The power-law formulation is given in Equation 2.32.

$$\sigma_y = k\varepsilon^n = k\left(\varepsilon_{yp} + \bar{\varepsilon}^p\right)^n \tag{2.32}$$

where k and n are the strength coefficient and hardening exponent respectively. The intersection between Equation 2.32 and $\sigma = E\varepsilon$ gives the elastic strain at yield. The result is given in Equation 2.33

$$\varepsilon_{yp} = \left(\frac{E}{k}\right)^{\left[\frac{1}{n-1}\right]} \tag{2.33}$$

The option to additionally specify the yield stress is possible with this material model, in which case Equation 2.32 is manipulated such that the strain is set to the subject of the formula, as given in Equation 2.34

$$\varepsilon_{yp} = \left(\frac{\sigma_y}{k}\right)^{\left[\frac{1}{n}\right]} \tag{2.34}$$

2.9 Summary of Literature Review

The side doors in passenger vehicles are typically reinforced with bars, tubes or corrugated steel structures to improve side impact protection. These structures may also be supplemented with side and curtain airbags to provide a cushion between the occupant and internal structure of the vehicle. There are several regional institutes and regulatory bodies such as the NHTSA and Euro NCAP whose purpose it is to establish and implement guidelines and standards for automotive safety. The two main types of side impact tests carried out make use of either an MDB, which is projected into a stationary vehicle, or a rigid vertical pole into which the vehicle is projected laterally at speeds of between 26-32 km/h. Pole tests typically result in a higher maximum intrusion as the contact area of the pole is smaller than the deformable barrier of an MDB. Several available metrics are used to compare the performance of components in an impact. Examples of such metrics include the CFE, EA, SEA, SPI, and energy-absorbing effectiveness.

Lateral impact investigations have been carried out involving heat treated tubes, constant density and functionally graded foam filled tubes, ribbed tubes, and tubes with functionally graded thicknesses. Functionally graded foam filled tubes were found to absorb more energy than their constant foam density counterparts, and constant foam density tubes were found to have a higher SEA than their hollow tube counterparts. Ribbed tubes were also found to absorb more energy than hollow tubes due to an increased moment of inertia. Another study found that a holistic view to improving all components protecting occupants in a side impact yielded far better results than the improvement of components in isolation.

Several material models have been developed to describe the behaviour of different materials under different loading conditions. However, the power law plasticity model offers the best balance between effort expended during material testing and accuracy as it requires fewer experiments, and has only two variables to determine from quasi-static loading.

Chapter 3

Experimental Method

This chapter is divided into 3 parts, namely the door drop test rig design, side impact beam setup, and testing method used for material characterisation. Tests were conducted on the vehicle door, and the side impact beam separately to validate the numerical models, and the material characterisation was performed to obtain material parameters for the Finite Element (FE) model. All components in the vehicle door had already been characterised and published by the National Crash Analysis Center (NCAC) [81]. It was therefore not necessary to perform material characterisation of these components.

3.1 Door Impact Test Rig

The side impact door test was conducted in a vertical drop tester. Due to spatial constraints the window frame was removed so that the door specimen could fit within the framework of the drop tester. A Computer Aided Draughting (CAD) representation of the components fabricated for the experimental setup (including the door) are shown in Figure 3.1.

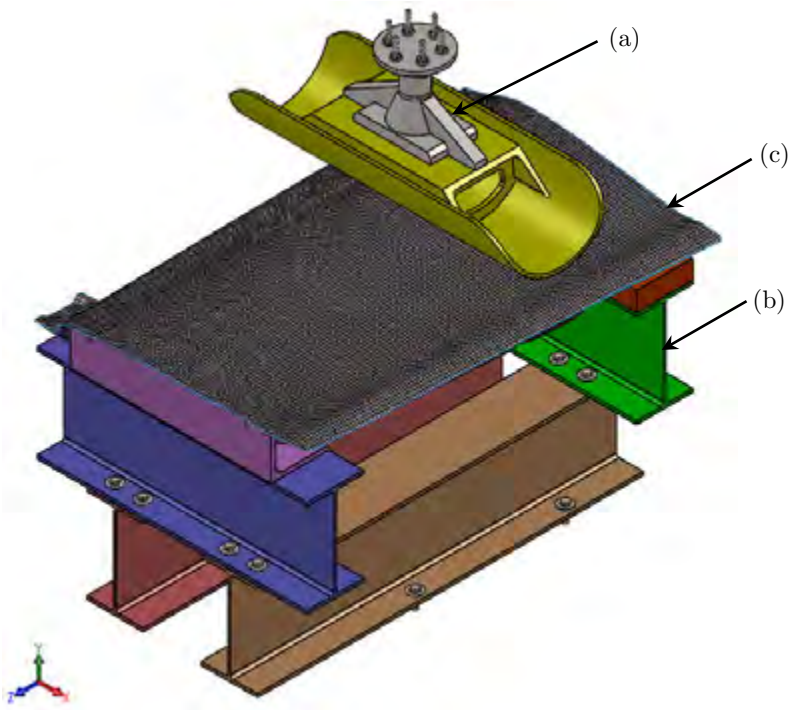

Figure 3.1: Experimental rig setup with (a) striker/impactor, (b) fixed base and (c) trimmed door/specimen without window pillar.

The test rig comprised two transverse pairs of 254×146×31.1 I-beam girders and a 150×150×12 equal leg angle, making up the test apparatus. This allowed for approximately 250 millimetres of overhead deflection of the test specimen (door - illustrated in Figure 3.1(c)). The experimental setup of the door test rig after installation is shown in Figure 3.2. A striker mass of 385 kg and drop height of 1,274 m were determined based on results from the simulations of the door test rig to best emulate the deflection of the door specimen in the full vehicle simulation. The photograph in Figure 3.2 shows the door between the support structure of the vertical drop tester with A and B-pillar sections removed. The masses of the respective components making up the total striker mass are detailed in Table 3.1.

Figure 3.2: Side door impact test rig (with door installed).

Table 3.1: Drop tester masses.

	Qty	Description	Unit Mass	Total Mass
Required, part of drop tester	1	450×450×20mm Mounting Plate	31.38 kg	31.38 kg
	2	Threaded Rod and Nut	3.34 kg	6.68 kg
	6	M10 Striker Mount Bolt & Nut	0.053 kg	0.32 kg
	4	M12 Mounting Plate Bolt & Nut	0.065 kg	0.26 kg
	1	Cage	111.84 kg	111.84 kg
Impactor	1	Half Cylindrical Striker	49.18 kg	49.18 kg
Optional additive	5	450×450×20mm Steel Ballast	32 ± 0.1 kg	160 ± 0.5 kg
	1	Custom Ad hoc steel ballast	25.36 kg	25.36 kg
			Sub-Total:	385 ± 0.5 kg

There was no data on frictional effects in the guideway of the drop tester and thus was only determined by analysing camera footage of the impact after the test was conducted. It was initially assumed that the guides of a well lubricated well maintained drop tester would have negligible effect on the velocity at impact.

3.2 Side Impact Beam Test Rig

The side impact beam test rig shown in Figure 3.3 was built on the base of the door test rig. The test apparatus comprised of two support mountings, one bolted pivot and one hinged Teflon collar as illustrated in Figure 3.3(b). The hinged Teflon collar allowed for axial sliding of the tube about the hinged/pivot point. Two Teflon inserts, as shown in Figure 3.4, were machined to accommodate either a round tube with 43 mm diameter tube or a 40 mm square tube.

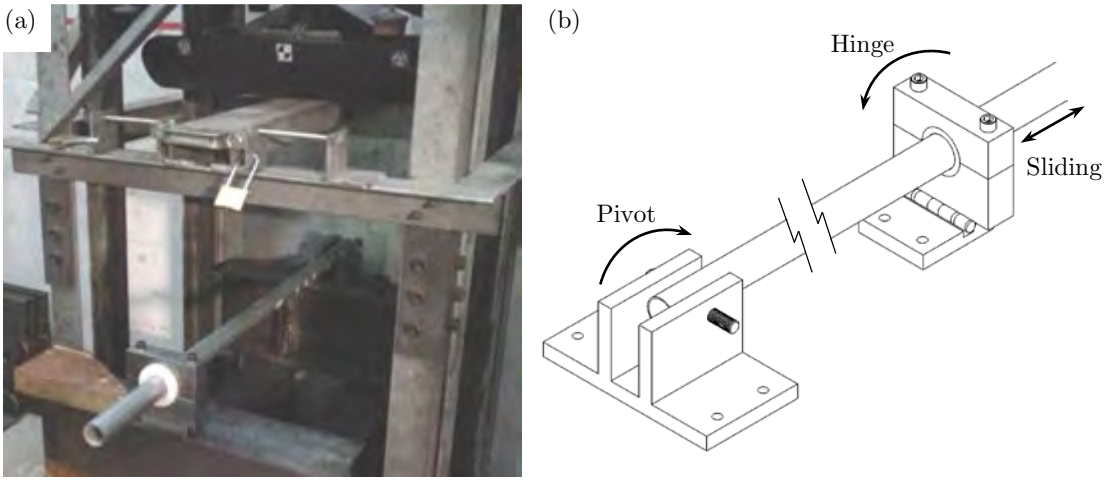

Figure 3.3: Experimental setup of side impact beam test rig with round tube test specimen installed by means of (a) photographic, and (b) schematic illustration.

Figure 3.4: Round (left) and square (right) Teflon inserts.

Teflon was chosen due to its low coefficient of friction with steel. It was assumed that the coefficient of friction between the sliding surfaces were in the range of 0.05-0.2 as per standard friction coefficient tables [82]. A total of 6 round tube and 22 Square tube specimens were tested experimentally at drop heights varying between 250-500 mm. The drop mass was kept constant at 200 kg.

Figure 3.5: Photographic illustration of the side impact beam drop testing rig after a drop test of a 200 kg mass from height of 250 mm onto a Ø43×2.3 mm steel tube.

Deflection measurements of the tube specimens were taken using two different methods; the first was by measuring the vertical displacement of the tube within the drop tester using an laser based distance meter placed flush with the base of the test rig, and the second, on an inspection table with a combination square and steel rule as illustrated in Figure 3.6.

Figure 3.6: Technique for measuring deflection of tube using combination square.

The reported deflections are the distance through which the centre of the unbuckled tube moved relative to the tube ends. An illustration of the reported deflection of the tube subjected to a drop test is shown in Figure 3.7(a). The laser deflection measurement was processed in the sketch utility of SolidWorks as shown in Figure 3.7(b) to account for fixed and sliding pivot boundary conditions of the test rig. The two techniques were compared with one another and results agreed within 1-3mm of each other.

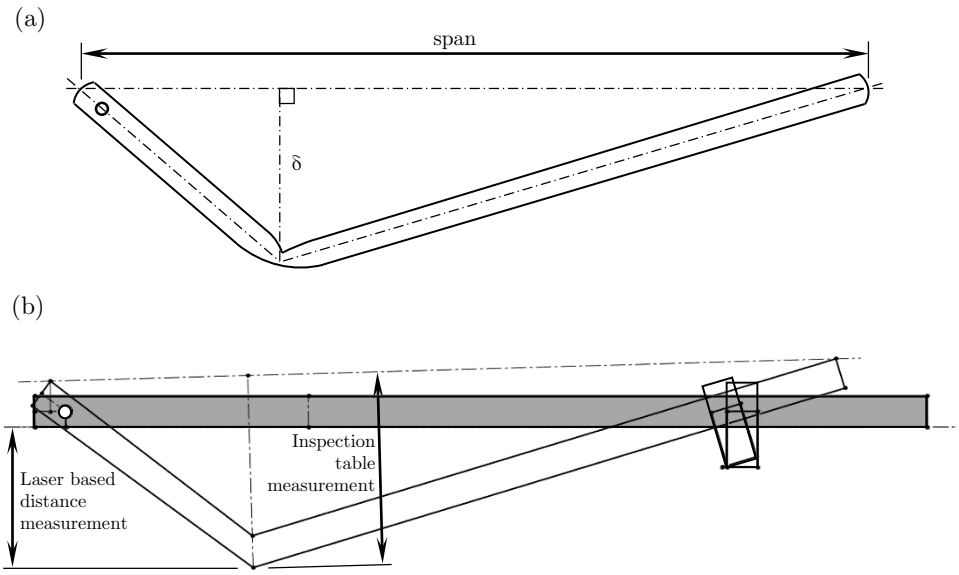

Figure 3.7: (a) Reported deflection (δ) of the tube as measured from the drop test, and (b) geometrically processed deflection measurement using SolidWorks sketch utility.

3.3 Material Characterisation

The square and round tube materials were characterised by means of Scanning Electron Microscopy (SEM) and quasi-static lateral compression tests. SEM was used to determine Young's modulus, while the compression tests were used to obtain the yield point and post-yield material properties.

3.3.1 Scanning Electron Microscopy

A Scanning Electron Microscope (SEM) produces images of a material sample with the use of a focussed electron beam. It is a visual aide with the additional capability to determine elemental composition by analysing the radiation signature from the sample [83]. Many elements have overlapping signatures throughout the reflective radiation spectrum which is also affected by the quality of the sample [83]. For this reason tests are performed on at least three different points on the sample in an attempt to control the effect of sample quality on the outcome [83]. Due to the emitted X-rays not all reflecting back to the receiver some elements may not be identified. One such example is carbon, which is an interstitial atom thus making identification and determination of the percentage thereof not possible using Energy-dispersive X-ray spectroscopy (EDS) [83]. The smoothness of the specimen also affected the accuracy of the results [83]. It was therefore important to prepare the sample before conducting SEM testing on it. This involved wet grinding and polishing the surface of the sample followed by dipping the sample in a solution to remove any moisture to prevent surface corrosion. Samples were stored and transported in a sample beaker to the Electron Microscope Unit (EMU).

3.3.2 Experimental Testing

In the interests of retaining the mechanical properties of the tube material a uniaxial tensile test would require the manufacture of curved specimen grips that would clamp the round tube in the materials testing machine. However, a second option was to conduct lateral compression testing of a sample length of tube. The latter required the least workshop and manufacturing time, and therefore was used to characterise the material. Furthermore, in the interests of coherency material properties for the square tube were obtained using the same method as the round tube.

50 mm length specimens were cut from the 40×2.0 mm square and Ø43×2.3 mm round tubes, and laterally crushed using a Zwick materials testing machine [84] as a means to characterise the material. The quasi-static tests were carried out at a crosshead speed of 5 mm/min for a duration of 240 seconds which was equivalent to a crush distance of 20 mm. The seam welds on the tubes were positioned as shown in Figure 3.8 across all tests. Three tests were carried out for each tube geometry to test for repeatability. A photographic illustration of the two tube specimen types tested in the Zwick materials testing machine [84] is shown in Figure 3.9.

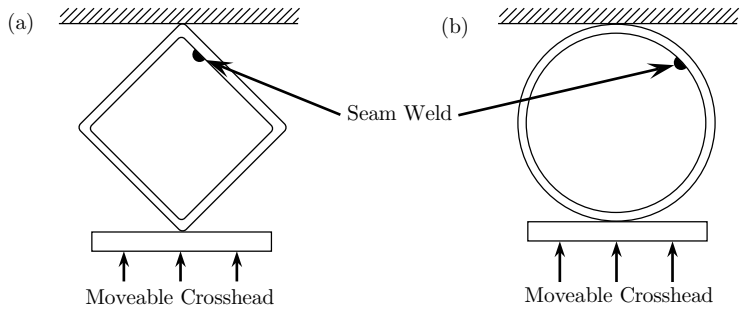

Figure 3.8: Seam weld positions for material characterisation tests of (a) 43×2.3 mm round and (b) Ø40×2.0 mm square tubes.

(a) (b)

Figure 3.9: **(a)** 30mm length of 40×2.0 mm Square and (b) Ø43×2.3 mm Round Tube in Zwick tensile testing machine prior to lateral compression.

The elastic modulus was determined from the material composition as described in the Scanning Electron Microscopy section. The analytical solution derived in Appendix B was determined for the elastic deflection of the round and square tubes and is repeated in equations 3.1 (B.37) and 3.2 (B.58) respectively.

$$\delta = \frac{0.1488FR^3}{2EI} \tag{3.1}$$

$$\delta = -\frac{Fw^3}{24\sqrt{2}EI} \tag{3.2}$$

The machine compliance was computed and subtracted from the force-deflection curve produced by the testing machine. The machine compliance is the elastic deformation of the machine under load. It was assumed that the machine is a spring with constant stiffness which was computed based on the experimental result and analytical solution to the problem, from which the machine stiffness was then computed and isolated. The machine compliance was subtracted using Equations 3.3 and 3.4.

$$k_{machine} = \left(\frac{1}{k_{effective}} - \frac{1}{k_{specimen}} \right)^{-1} \tag{3.3}$$

The effective stiffness is the linear elastic slope of the force versus deflection curve output from the Zwick [84], and the specimen stiffness is the analytically determined linear elastic slope of an ideal specimen, typically Young's Modulus of the material is required to determine this. The specimen deflection may then be calculated as given in Equation 3.4.

$$\delta_{specimen} = \delta_{effective} - \frac{F_{crosshead}}{k_{machine}} \tag{3.4}$$

This would yield the corrected deflection of the specimen without the effect of deformation of the machine. It should be noted that this is only necessary in the case where the deflection measurement is determined by means of the track of the moveable jaw of the machine. If an extensometer is used this would negate the need to remove machine deformation.

3.4 Summary of Experimental Method

Both the door and side impact beam experiments were carried out on the same apparatus in a vertical drop tester. The apparatus consisted of two transverse pairs of 254×146×31.1 I-beam girders bolted to a solid steel base. The door was bolted to a 150×150×12 equal leg angle on the hinged side, and bolted directly to the I-beam on the latch side. The drop mass and height for the door test was 385 kg and 1.274 m respectively. The drop mass and height for the side impact beam drop tests was 200 kg and 250-500 mm respectively. The tube materials were characterised by means of SEM and quasi-static lateral compression tests in a Zwick materials testing machine. SEM was used to determine Young's modulus, while the compression tests were used to obtain the yield point and post-yield material properties.

Chapter 4

Numerical and Experimental Results:

Finite element modelling
Planning of experiments
Validation of numerical model
Analysis of results

This chapter discusses the approach taken to determine the transient response of the front passenger door to a side impact in close conformance to the FMVSS 214 standard [15]. Subsequently, a simplified model consisting of only the door with strategically designed supports to emulate the behaviour of the door in the full vehicle model is discussed. This is followed by a side impact beam drop test study, along with the calibration of a numerical model to experimental data. Material characterisation using numerical modelling and experimental testing is also discussed. The numerical modelling was conducted in three phases and are summarised in Figure 4.1.

Phase one: - Simulation of a passenger car subjected to a side pole impact test at 29 km/h, in close conformation to the FMVSS 214 standard, to determine the impact characteristics of the door prior to optimisation.

Phase two: - A set of experiments coupled with numerical simulation of the vehicle door (door only) was undertaken to validate the door model. (With drop mass and drop height obtained based on the transient response of the door from the full vehicle model in Phase one)

Phase three: - Side Impact Beam Testing

- Characterising the materials of tubes by means of SEM and lateral compression tests for the material model used in finite element simulations,
- Experiments and simulations of the lateral impact of tubular structures (drop mass and drop heights chosen from simulations to give similar tube deflections as in phase two), and
- Parametric study on side impact beams

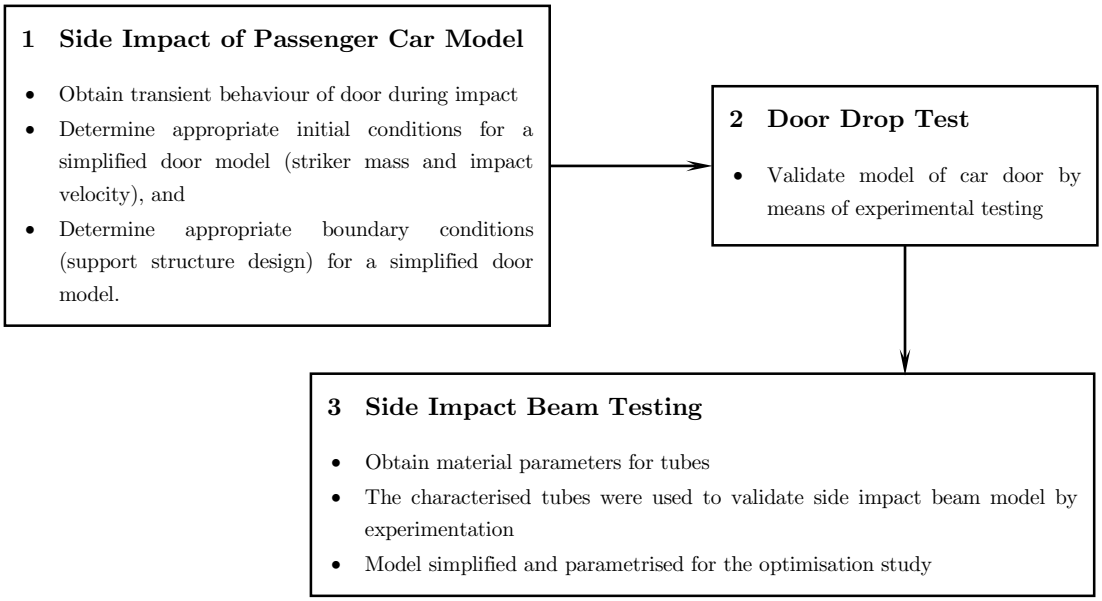

Figure 4.1: Flow chart of the finite element simulations and experiments.

LS-DYNA R7.1.1 was used to conduct the numerical simulations. The explicit solver was utilised to model brief transient dynamic effects (impact tests) and the implicit solver was employed to model quasi-static loading scenarios (material characterisation). The LS-DYNA solver simulates models by means of a set of commands from a structured input deck containing nodal and element details, contact algorithms, boundary conditions, material characteristics, and output requests. These results are recorded in either one, or a combination of binary, ASCII or text output files. The input deck can be generated in combination with a text editor, LS-PrePost, and ANSA 15.2.3. The latter two packages involve an interactive graphical environment used to produce and decompose the geometry into meshable regions, assign physical and material properties, and assign load and boundary conditions in a more visual manner.

4.1 Side Impact of Passenger Car Model

An FE model of a 2010 sedan (Vehicle Identification Number JTDBT4K37A4067025) developed by NCAC of The George Washington University under contract with the Federal Highway Administration (FHWA) and NHTSA of the US DOT [81], was used in this study. The complete model consisted of 771 parts with a total of 974,383 elements with a fully functional suspension and steering subsystem, as well as all major structural components, but excluded any interior components or restraint systems [81]. An illustration of the FE model is provided in Figure 4.2.

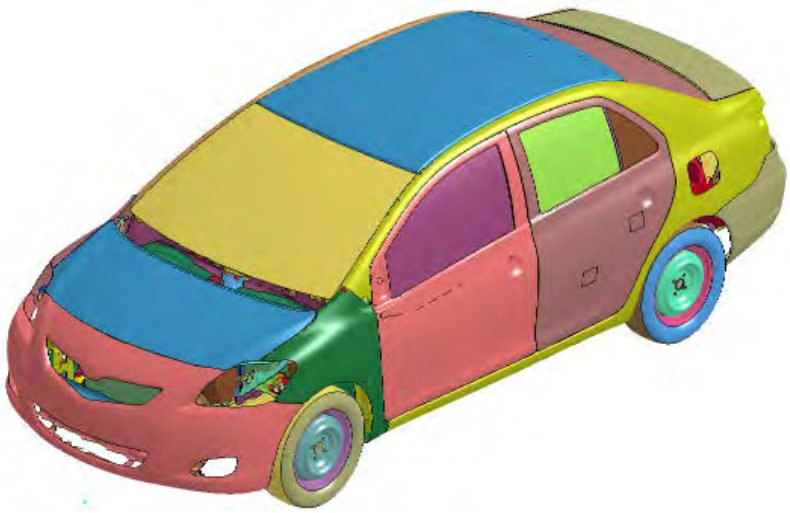

Figure 4.2: Finite element model of a 2010 sedan, obtained from the NCAC's finite element model archive [85].

Components were discretised so that the element size of components were represented in accordance with simulation processing time and accuracy relative to the rest of the vehicle [81]. For example, the engine was modelled with a comparatively coarse mesh as a solid block using hexa (brick) elements, with density chosen to reflect the same mass as the original engine [81]. The engine was modelled as an isotropic hypoelastic material body with solid elements as it remains largely undeformed in crashes. The windshield and door windows were modelled as a modified piecewise linear plasticity material without the inclusion of damage mechanics. The chassis was modelled with shell elements using the piecewise linear plasticity material model, and joined with spot-welds. The Heat Affected Zone (HAZ) of the spot-welds were accounted for by means of the spot-weld material definition in LS-DYNA. The tyres and damper joints were modelled as an elastic and nearly incompressible continuum material (Blatz and Ko Rubber [86]) respectively. Failure criteria were not set for any component definitions. Material data for all main mechanical components were obtained through testing of samples extracted from vehicle parts [81]. A comparison of the salient global static parameters are tabulated for the actual vehicle and the numerical model in Table 4.1.

Table 4.1: Actual vehicle and finite element model mass, inertia, and centre of gravity comparisons based upon data from testing at SEAS, Inc. [81].

	Actual Vehicle	**FE Model**
Weight (kg)	1078	1100
Pitch inertia (kg.m^2)	1498	1566
Yaw inertia (kg.m^2)	1647	1739
Roll inertia (kg.m^2)	388	395
Vehicle CG X (mm)	1022	1004
Vehicle CG Y (mm)	-8.3	-4.4
Vehicle CG Z (mm)	558	569

Figure 4.3 shows the internal structure of both the front and rear doors of a light passenger vehicle. Two side impact beams are mounted in the rear door with only one side impact beam fitted in the front door. In this study the front door was selected for analysis. The methodology developed and used in this study for the front door may be applied to the rear door.

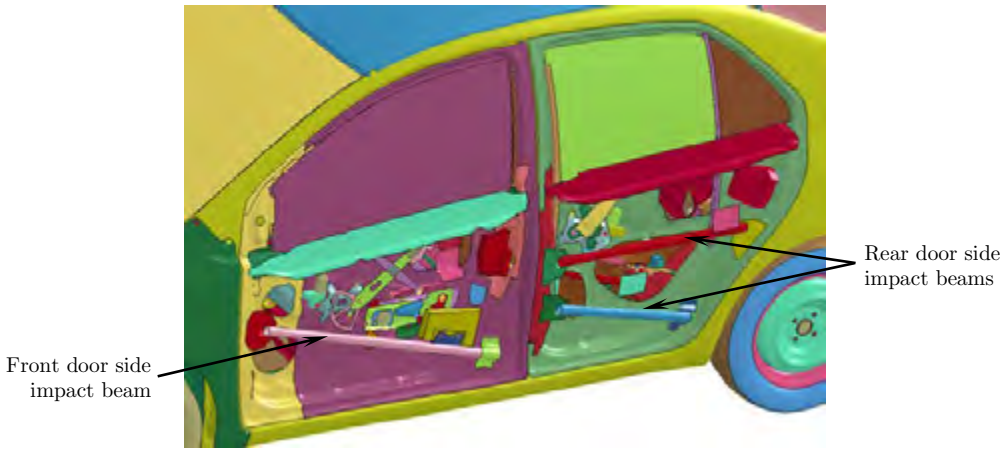

Figure 4.3: Internal structure of the front and rear passenger doors from a typical 4-door sedan [85].

The finite element model was validated by the NCAC in accordance with the frontal New Car Assessment Program (NCAP) conducted by the NHTSA. The model was validated by comparing accelerometer time histories of a frontal 35 mph impact of the actual test versus the numerical simulation with accelerometers mounted in the same location on the model.

The model of this vehicle conforms to the Manual for the Assessment of Safety Hardware (MASH) 1100C vehicle requirements, where 1100 refers to the standard mass of a small vehicle in kilograms [87]. MASH is a vehicular crashworthiness testing protocol progressively implemented between October 2009 to January 2011 in the United States to supersede the National Cooperative Highway Research Program (NCHRP) Report 350 first implemented in 1993 [87]. The new protocol was

adopted to account for changes in automotive design. The main differences are highlighted in Table 4.2. Some physical quantities of the finite element model as compared to the actual car are also provided courtesy of the NCAC in Table 4.3.

Table 4.2: Significant changes between NCHRP 350 and MASH test protocols [87].

Topic	**NCHRP 350**	**MASH**
Small car impact angle	20 degrees	25 degrees
Light truck test vehicle	2000P vehicle (4,400 lbs.)	2270P vehicle (5,000 lbs.)
Gating terminals and crash cushion impact angle	15 degrees	5 degrees
Variable message signs and arrow board trailers	No mention	Added to TMA crash test matrix
Support structure & work zone traffic control device testing	Only small car tested	Small car and light truck tested
Windshield damage criteria	Subjective/Qualitative	Objective/Quantitative
Vehicle rebound in crash cushion tests	None	Required

Table 4.3: Comparison of finite element model & vehicle parameters used in the NCAP tests [81].

	FE Model Test	**Test 5677**	**Test 6221**
Weight (kg)	1263	1271	1245
Engine Type	1.5L V4	1.5L V4	1.5L V4
Tire size	P185/60R15	P185/60R15	P185/60R15
Attitude (mm) (As delivered)	F – 668	F – 673	F – 675
	R – 673	R – 680	R – 673
Wheelbase (mm)	2538	2551	2463
CG (mm) Rear of front wheel centreline	1035	999	976
Body Style	4 Door Sedan	4 Door Sedan	3 Door Hatchback

More information regarding tests 5677 and 6221 can be obtained from the NHTSA's online archive at [88, 89]. The side impact beam serves to reduce the amount of intrusion to the occupant cell during a side impact, by increasing the ability of the door to absorb and disperse energy into the surrounding chassis [29]. It also serves the function of reducing structural damage and thus repair costs resulting from low speed accidents. This is a factor taken into consideration during the design phase of the car as it would affect insurance and running costs for the vehicle [29].

The first phase of numerical validation involved the crash testing of a passenger car into a rigid vertical pole. The FMVSS 201 standard specifies the use of a 10 inch outer diameter vertical pole The pole must be located such that the point of impact of the rigid pole lines up within two transverse planes located ±38 mm longitudinally of the position of centre of gravity of the crash test dummies head with respect to the car. The velocity vector of the vehicle must also line up within ±3° of the transverse plane of the centre of gravity of the vehicle [90], as illustrated in Figure 4.4.

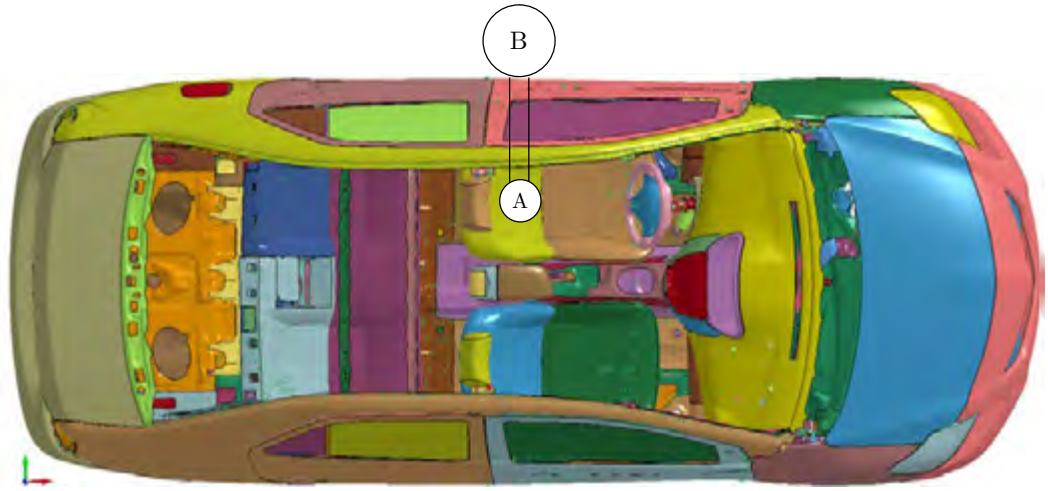

Figure 4.4: FMVSS 201 rigid pole location and test conditions for a 4-door sedan (A: Crash test dummy head, B: Rigid 254 mm diameter vertical pole).

For the purpose of this study, the original pole position shown in Figure 4.4 was not useful to perform side impact beam analysis and optimisation as the bulk of the impact energy would be dissipated through the B-Pillar instead of the door. For this reason the rigid pole was moved to a position more suitable to test the ability of the side impact beam to resist intrusion and disperse energy away from the occupant and into the chassis. Ideally it would be better to position the rigid pole so that it impacts the door at mid-span. However due to spatial constraints in the drop tester the position of the rigid pole was offset to one side as shown in Figure 4.5. The centreline of the pole at the new position was 1046 mm longitudinally from the front left axle (420 mm from the edge of the door), with the pole extending over the full height of the vehicle. The impact velocity was set to 29 km/h (8.056 m/s) with a simulation time of 100 milliseconds.

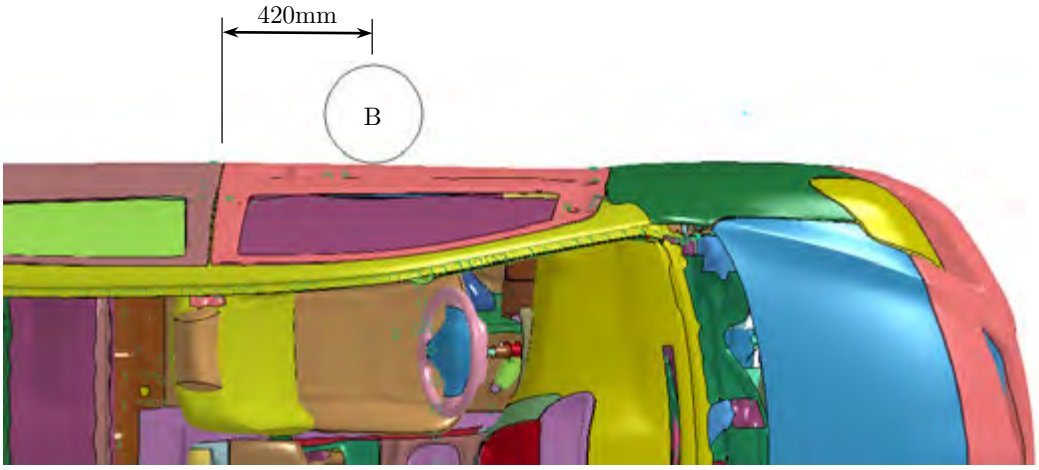

Figure 4.5: Position of rigid pole for the purpose of testing the impact beam's ability to absorb and deflect energy away from the occupants.

Given that during a side impact only the door separated occupants from the obstruction, performance of the vehicle was largely determined by its ability to resist intrusion to the occupant cell. Five appropriate performance criteria for the analysis of vehicular crashworthiness are:

- Energy Absorbed,
- Specific Energy Absorbed,
- Crash Force Efficiency,
- Transverse deflection, and
- Energy Absorption Effectiveness.

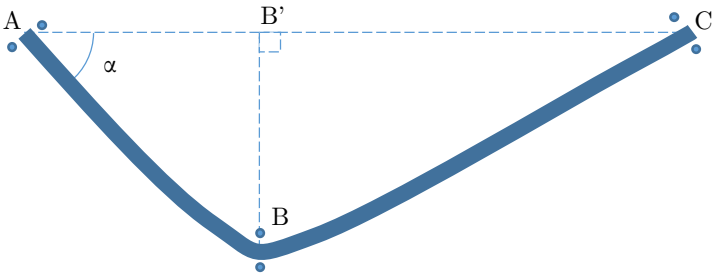

Figure 4.6: Graphical representation of the means through which transverse deflection (BB') is defined.

The transverse deflection of the door was calculated using the geometry shown in Figure 4.6. The positions of A, B and C are determined by means of obtaining positional coordinates of two diametrically opposite nodes at each of the three cross-sections. The position B' is then determined by setting the dot product of vectors AC and BB' to zero where the only unknowns were the three spatial coordinates of B'. However, point B' lies somewhere along line AC, thus the relationship

between each of the three coordinates was determined and solved for. The transverse deflection is the length of BB'. The equations used are given in 4.1, 4.2, and 4.3.

$$\alpha = \frac{(B_x - A_x)\overline{AC}_x + (B_y - A_y)\overline{AC}_y + (B_z - A_z)\overline{AC}_z}{\overline{AC}_x^2 + \overline{AC}_y^2 + \overline{AC}_z^2} \tag{4.1}$$

From where B' was calculated from Equation 4.2.

$$\boldsymbol{B' = A + \alpha\overline{AC}} \quad \begin{cases} B'_x = A_x + \alpha\overline{AC}_x \\ B'_y = A_y + \alpha\overline{AC}_y \\ B'_z = A_z + \alpha\overline{AC}_z \end{cases} \tag{4.2}$$

The perpendicular distance BB' was then calculated using points B and B' as given in Equation 4.3.

$$|BB'| = \sqrt{(B'_x - B_x)^2 + \left(B'_y - B_y\right)^2 + (B'_z - B_z)^2} \tag{4.3}$$

The internal energy of the beam is a measure of the total cumulative strain from each element in the beam relative to its unloaded state. This quantity was extracted from the results of the FE simulations. The vehicle was projected into a 273 mm diameter rigid vertical pole at 29 km/h. The vehicle was assumed to be on a sled with negligible mass such that the coefficient of friction between the tyres and ground was negligible. The resulting time history of the side impact beam deflection for the full vehicle model is shown in Figure 4.7. The result showed a transverse deflection of 443 mm at 92 milliseconds after the beam began to deform. The deformation of the full vehicle model at 92 milliseconds, corresponding to the result shown in Figure 4.7, is illustrated in Figure 4.8.

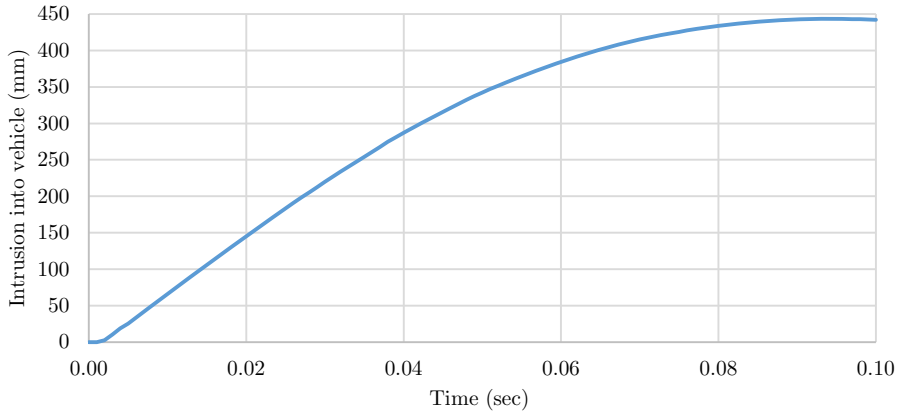

Figure 4.7: Time history of the intrusion of the 273 mm diameter pole into the vehicle, which was projected laterally into the pole at 29 km/h.

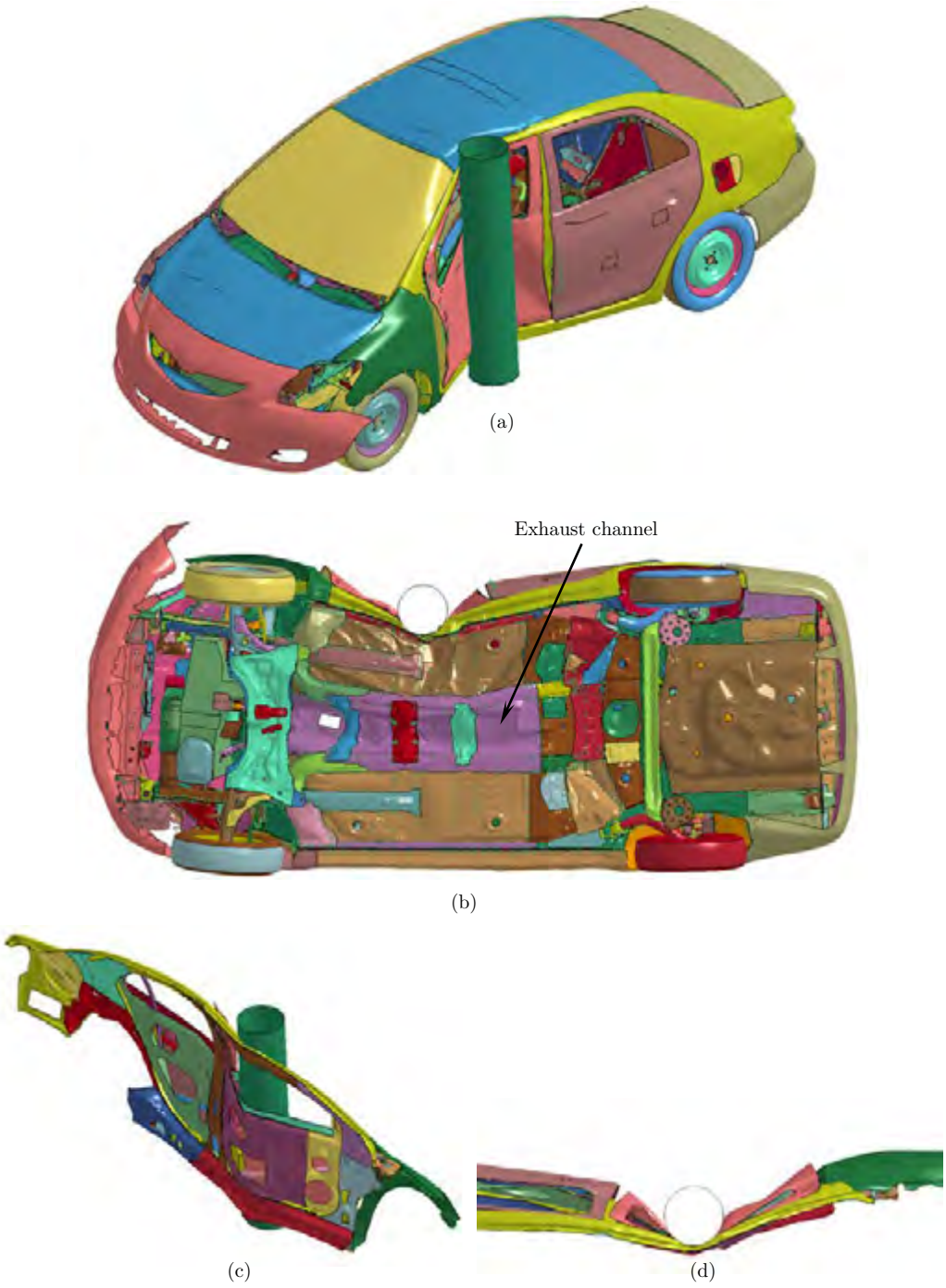

Figure 4.8: (a) Side impact test of a 4-door sedan at 29 km/h into a 273 mm diameter rigid vertical pole, (b) point of maximum intrusion of the full vehicle model subjected to a side pole test at 29 km/h, (c) isometric view, and (d) top view of full vehicle model impact where the side exposed to impact is isolated.

An isometric view of the simulation result at 92 milliseconds after impact is shown in Figure 4.8(a), and the underside of the vehicle is shown in Figure 4.8(b). The side of the vehicle, as illustrated in Figure 4.8(c) and (d), was isolated from the rest of the vehicle to highlight the deformation of the door and its surrounding support structure. The rigid pole caused deformation of the door, outer rocker panel, roof, floor, and windshield. The vehicle, upon impact, appeared to roll into the vertical pole with the top of the car undergoing marginally higher deformation than the floor. This may be attributed to the presence of more material resisting deformation near the floor than on the roof, with the side impact beam in the bottom third of the door. A damage model was not included in the windshield material, which resulted in ductile behaviour observed in Figure 4.8(a). The empty exhaust channel indicated in Figure 4.8(b) also deformed considerably (width/gap reduced by 36% from 237 mm to 85 mm), which may not deform as much with the inclusion of an exhaust system. The graphic in Figure 4.8(c) shows that most of the deformation occurred in the door, A-pillar and outer rocker panel. The illustration in Figure 4.8(d) shows the formation of a distinctive V-profile of the door, as it wrapped around the rigid pole.

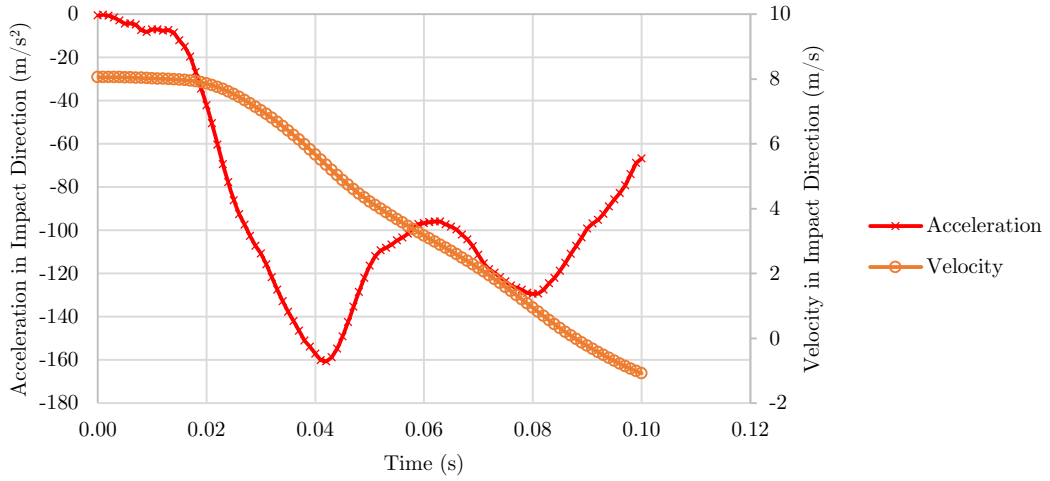

Figure 4.9: Vehicle kinematics of the centre of gravity during impact.

The impact kinematics for the side impact simulation of the full vehicle model are shown in Figure 4.9. The acceleration versus time history shows that a peak acceleration of approximately 16.3G's (Gravitational Acceleration) was experienced 0.04 seconds after impact. The effect of adding or removing ground on the deformation of the car during impact was also investigated. The results, illustrated in Figure 4.10, showed that the car in the simulation without ground rolled marginally more than the car in the simulation with ground in place. This was observed as the top of the vehicle leaning more into the rigid pole than the bottom of the vehicle.

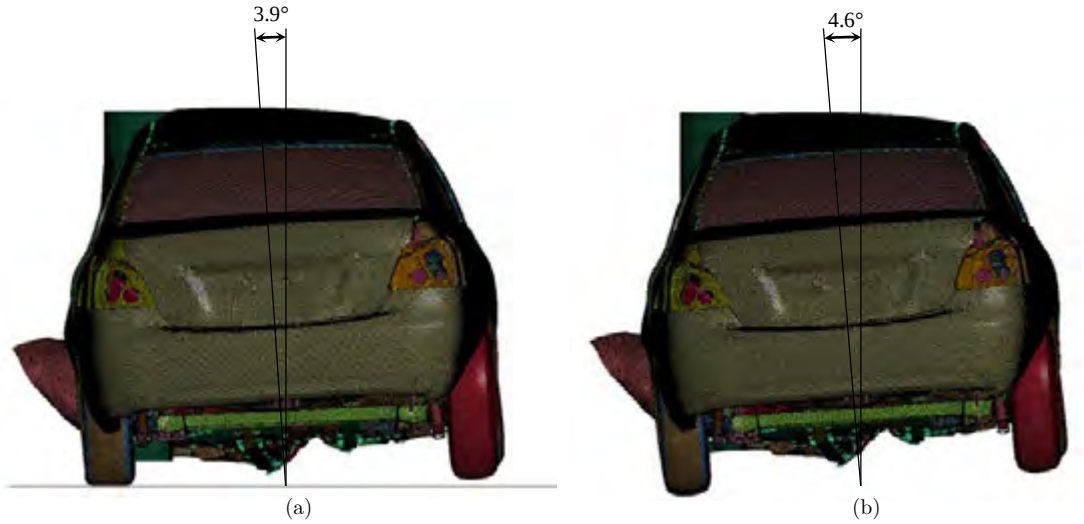

Figure 4.10: Side impact with rigid vertical pole at 29 km/h with ground (left), and without ground (right).

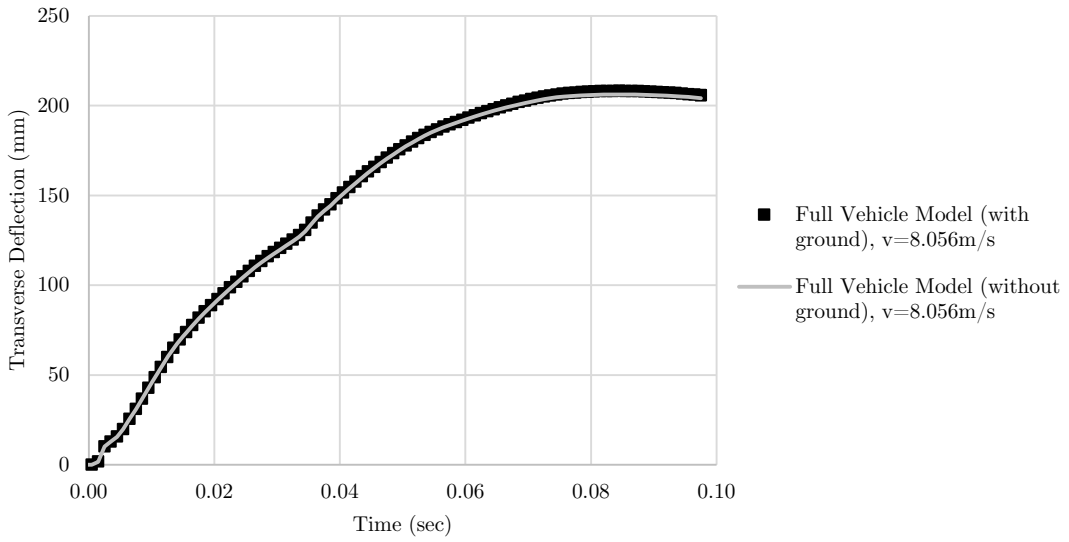

Figure 4.11: Transverse deflection time histories of impact beam.

The transient deflection of the side impact beam with and without ground are superimposed with one another in Figure 4.11. Despite a qualitative observation of the car without ground rolling more than the model with ground the plot of the transverse deflection of the side impact beam showed negligible effect of the ground on the behaviour of the beam during a collision. A breakdown of the distribution of energy absorbed in the side impact of the full vehicle model with ground is shown in Figure 4.12. The four highest absorbers of energy, namely floor and roof panels, door and side impact beam, accounted for over three quarters of the energy absorbed. The side impact beam was one of

the single highest energy absorbing components in this simulation, having absorbed 2.76 kJ of the total 33.1 kJ. The bulk of the impact energy (66%) is dissipated via bending of the sheet metals of the floor, roof and door panels.

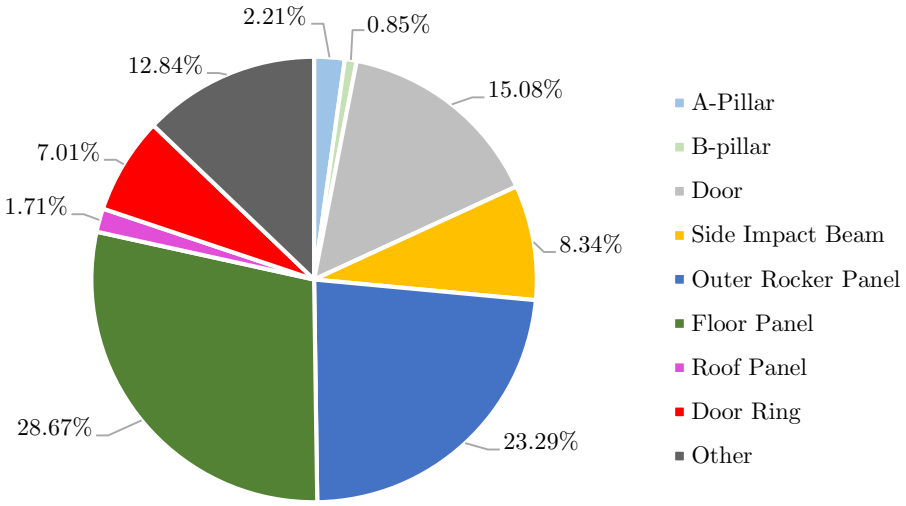

Figure 4.12: Breakdown of the largest contributing members to energy absorption in side impact test of the full vehicle model in this study.

4.2 Door Drop Test

The door shown in Figure 4.13(a) was extracted from the full vehicle model and modified to exclude the top frame as shown in Figure 4.13(b). A test bed was designed to fit within the framework of the drop-tester to carry out experiments to validate the finite element model of the door. The simplified test rig layout was designed to reproduce the V-profile of the door from the full vehicle simulation results illustrated in Figure 4.14, as well as the transient response of the side impact beam within the door. The transient response of the door was extracted from the results of the full vehicle model simulation to determine appropriate initial and boundary conditions for the car door experiment. The initial and boundary conditions included the effect of:

- Initial Conditions: - Mass of the impactor
  - Strike velocity of the impactor

- Boundary conditions: - Supporting and clamping conditions of the door in the test rig

(a) (b)

Figure 4.13: (a) Door model extracted from full car model, and (b) modified door model to exclude top frame to simulate experiments.

Figure 4.14: V-Profile formed in side door due to pole impact in full vehicle model.

The numerical model shown in Figure 4.15 replicated the relevant geometries of the test rig of the experimental test setup. Due to the complex nature of the door geometry the individual components were discretised using a mixed quadrilateral and triangular shell element configuration. The Belytschko-Lin-Tsay shell element formulation with five through thickness integration points was the chosen method of describing the quadrilateral elements as it was found to be the most computationally efficient [54], and the C^0 triangular shell element implementation with five through thickness integration points was chosen as it was a computationally efficient triangular element complement to the Belytschko-Lin-Tsay quadrilateral shell element in solving transient non-linear natured problems [54]. Preliminary calculations showed that the I-beams in the door test rig deflected minimally. Therefore only the parts of the test rig in contact with the door specimen were modelled for the first door test as shown in Figure 4.16.

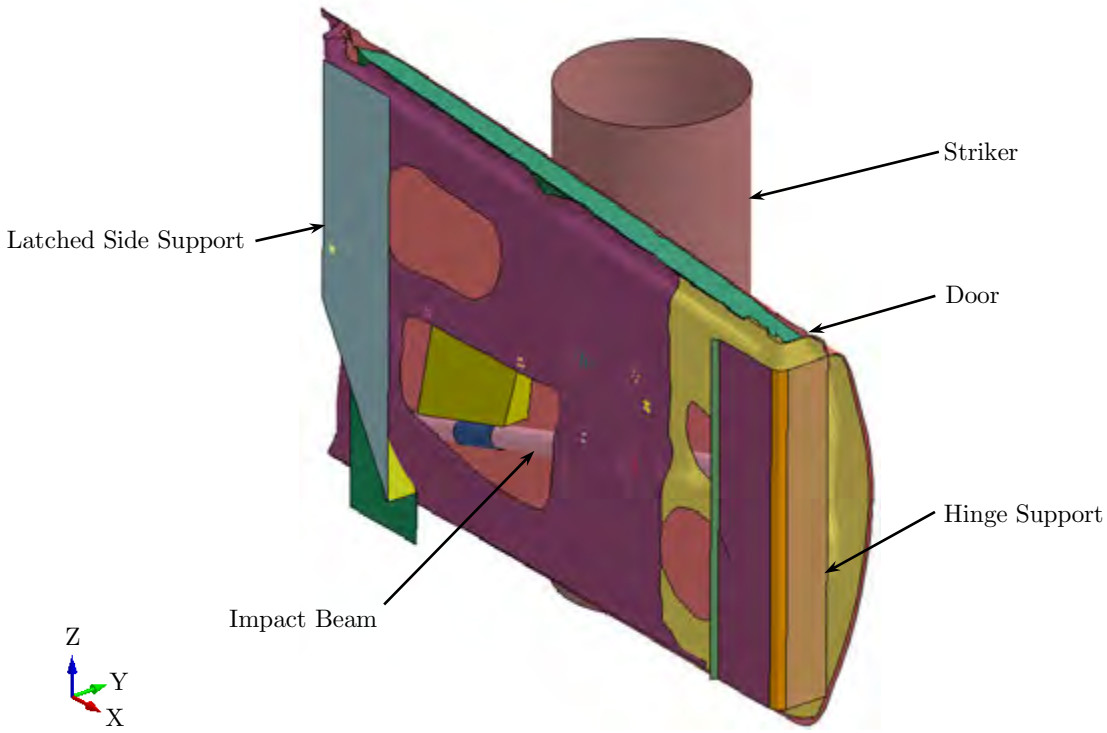

Figure 4.15: Finite element model of the experimental setup of the door impact test.

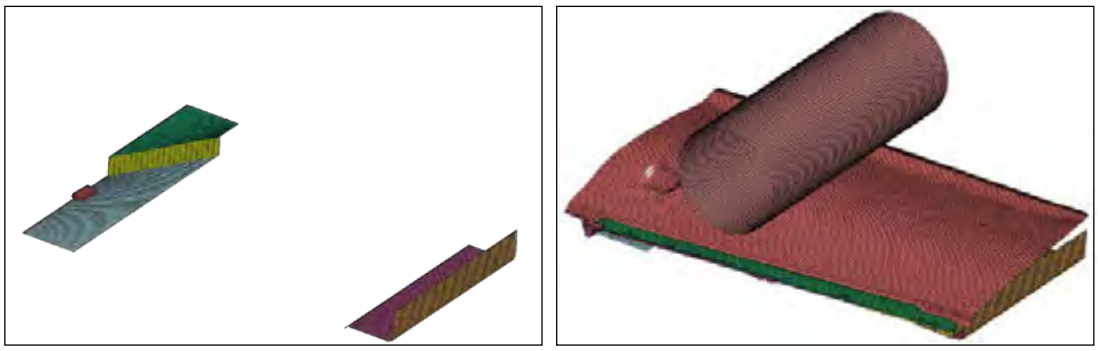

(a) (b)

Figure 4.16: Model of (a) rigid test rig components, and (b) rig with door and striker in place.

As the door and its components were made of a strain rate sensitive material (steel) it was important that both the rate of deformation and maximum transverse deflection of the beam be emulated in the drop tester as best possible. The model of the door test rig illustrated in Figure 4.15 was used to determine the drop height and mass through an iterative process. For the first iteration a 250 kg drop mass and a drop height of 3.3 m was chosen (corresponding to a freefall velocity at impact of 29 km/h). The results indicated that the maximum deflection was occurring approximately 0.04

seconds sooner than in the full vehicle side impact simulation which was at 0.09 seconds as shown in Figure 4.17 because the mass of the impactor was significantly smaller than the mass of the entire vehicle. As a result the natural frequency of the impact would be shorter for the same impact velocity.

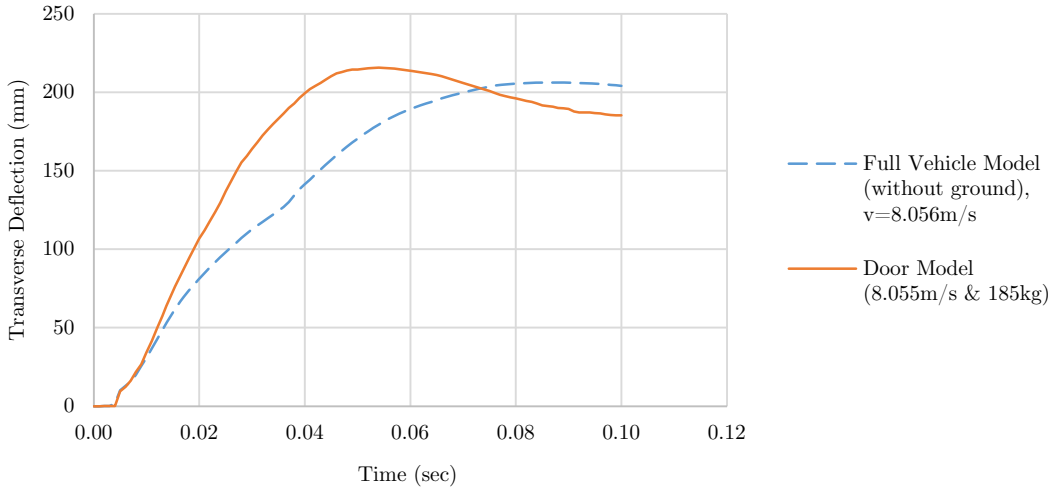

Figure 4.17: Transverse deflection time histories of impact beam with striker velocity and mass of 5 m/s and 390 kg respectively, at the point of impact.

The best combination of mass and impact velocity was determined by first adjusting the slope of the transient response of the transverse deflection of the side impact beam by altering the velocity of the striker. The impactor mass was then adjusted to obtain a similar deflection of the beam in the frameless door model when compared with the deformation of the beam in the full vehicle model. After several iterations the results, illustrated in Figure 4.18, showed good correlation between the transverse deflections of the impact beams from the full vehicle and door models. A drop mass of 385 kg and drop height of 1.274 m yielded best results and was used in the experiments.

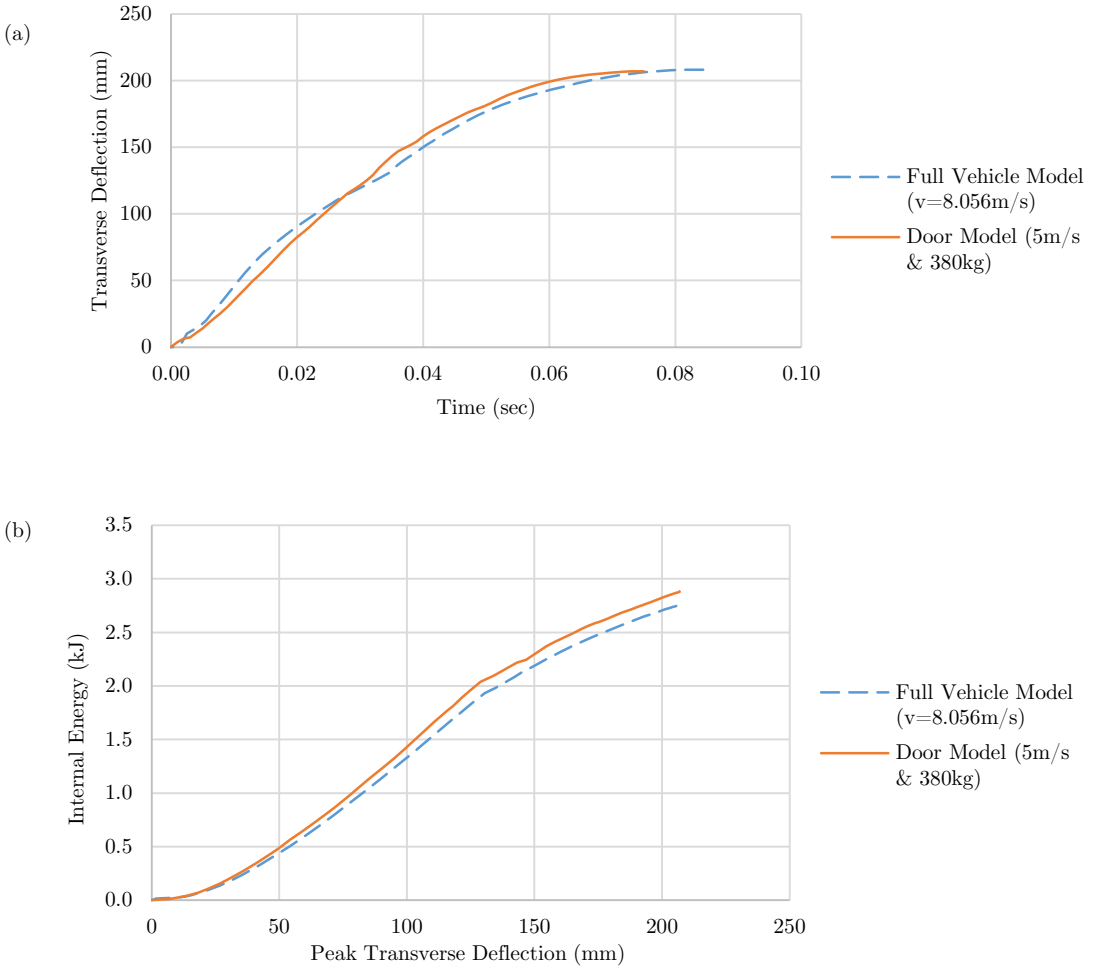

Figure 4.18: (a) Transverse deflection time histories of impact beam with striker velocity and mass of 5 m/s and 385 kg respectively at the point of impact, and (b) internal energy of the impact beam versus transverse deflection for the door and full vehicle models.

The maximum deflection of the side impact beam in the door model was 208.3 mm, and that of the full vehicle model was 208.1 mm. The variation in maximum deflection between the two models was considered acceptable. The internal energy in the impact beam expressed as a function of transverse deflection of the beam is plotted for the full vehicle model and the door model in Figure 4.18(b). Despite the absorbed energy of the impact beam in the simplified door model being larger than the beam in the full vehicle model, the error at maximum transverse deflection was still below 5%, showing good correlation between the two models.

A visual comparison of the two numerical setups is illustrated in Figure 4.19. Both setups produced a V-shape with subtle differences on the deformation profile on the hinged and latch sides of the door. This is expected because the door mountings in the passenger car plastically deformed along with the door, whereas the mounting for the door in the simplified door test rig model was rigid.

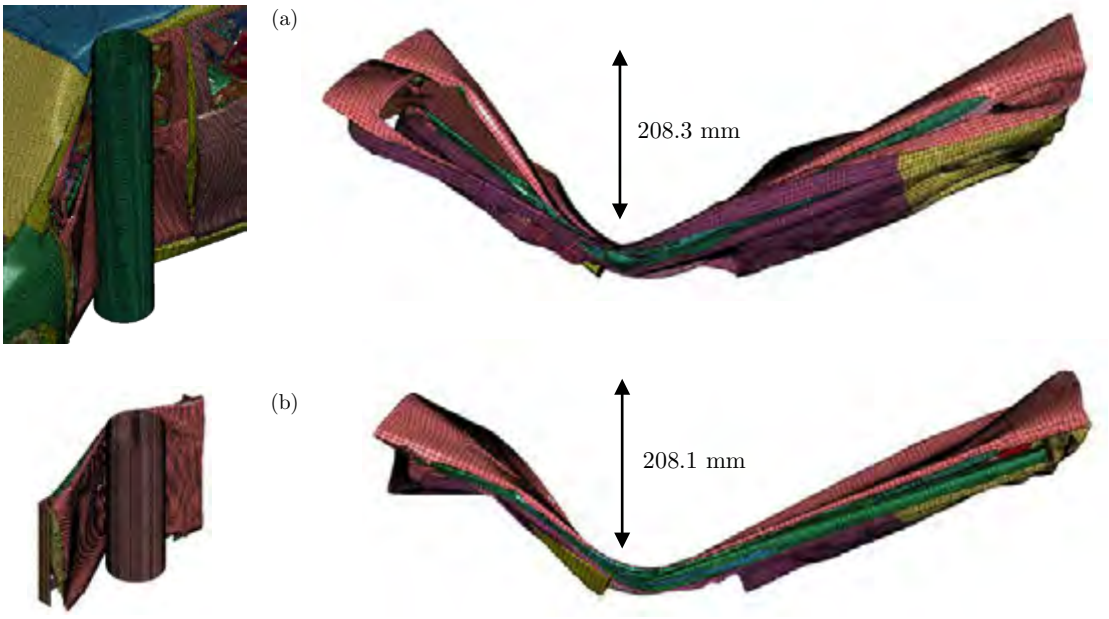

Figure 4.19: Post crash deformation of (a) side impact test of full vehicle model at 8.056 m/s into Rigid ø273 mm Pole, and (b) door drop test model with drop mass 385 kg, ø273 mm Pole at 5 m/s and 90° to door.

4.2.1 Impact test experiment on the modified car door

An impact test on the modified car door (top frame removed) was carried out to assess the validity of the numerical model. A time lapse of five frames from footage of the drop test recorded from a GoPro Hero 4 Black Edition at 120 frames per second (fps) is shown in Figure 4.20. Frame 0 in Figure 4.20(b) shows motion blur as the exposure time, which is fully automated on the GoPro, was not short enough to clearly capture the high striker impact velocity of 4.5 m/s at a distance of 1 m. Frames 11, 29 and 132 also show the equal leg angle changing position due to the deformation of the hinged side I-beam.

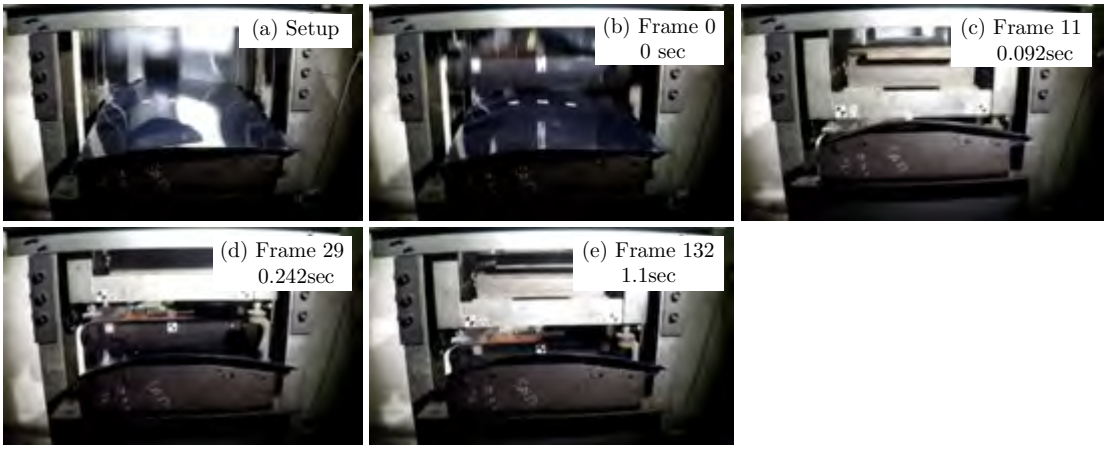

Figure 4.20: Time lapse of drop test impact, (a) before impact, (b) at the point of contact, (c) at maximum deflection, (d) first rebound, (e) once striker is at rest. Frame Rate = 119.8 fps.

The I-beams making up the test rig were observed to deform during impact. The two top I-beams underwent significant deformation, one of which deformed plastically by about 8.5° as shown in Figure 4.21. This made it impossible to compare with results of the numerical simulations with the experimental results as the test rig apparatus was not included in the numerical model. The numerical model was subsequently updated to include the I-beams as illustrated in Figure 4.22. The model was rerun and the inclusion of the I-beam in the model greatly improved the comparability of the simulation to the experiment.

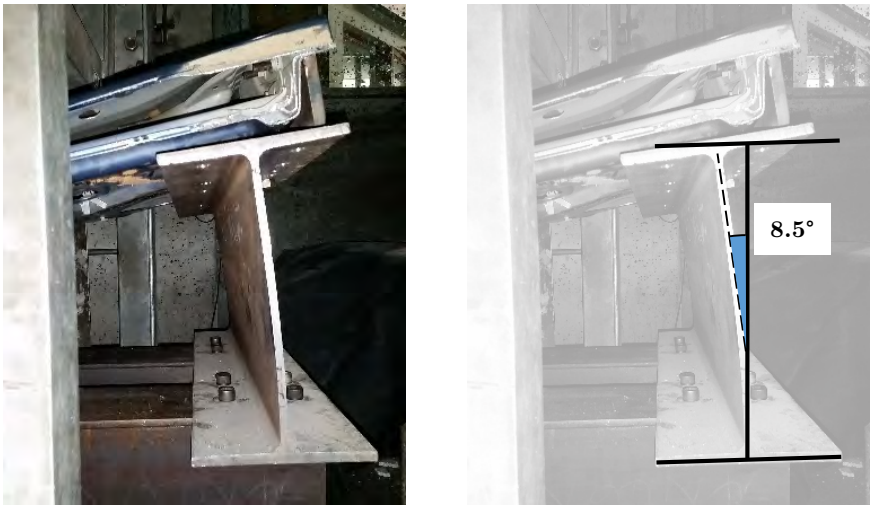

(a) (b)

Figure 4.21: Permanent onset of deformation in hinged side I-beam.

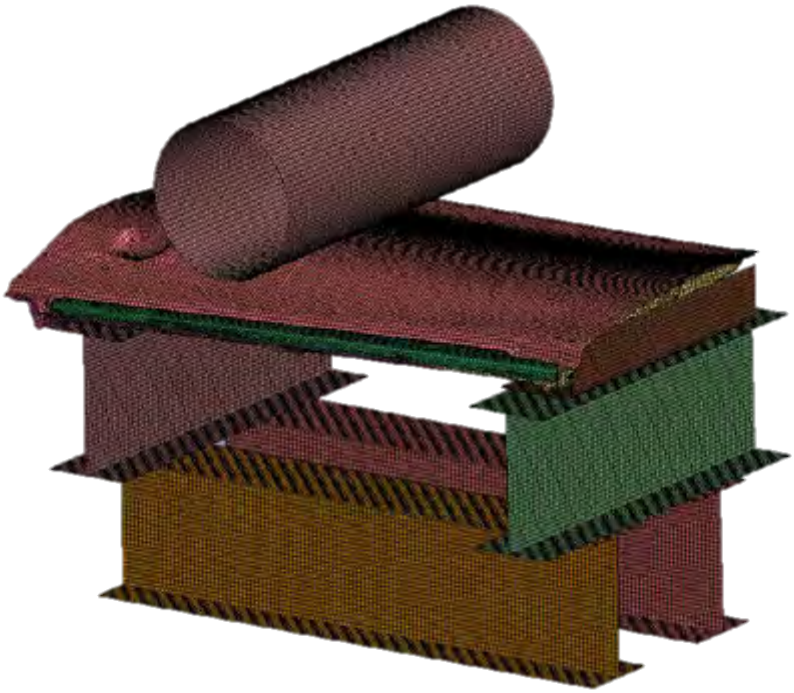

Figure 4.22: Updated numerical model of the experimental door impact test setup with flexible base structure.

Figure 4.23: Numerical versus experimental bend to hinge side I-beam with fully laden door and striker, door drop test with a drop mass of 385 kg, rigid ø273 mm pole at 5 m/s and 90° to the door.

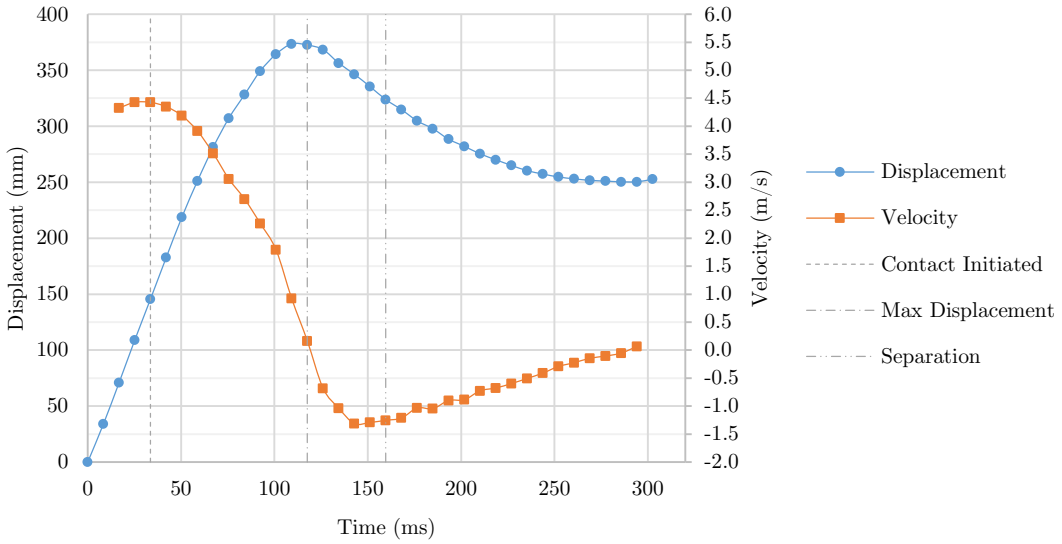

Figure 4.24: Displacement and velocity time histories of a Ø273 mm striker in an experimental drop test of a 4-door sedan front door with a 385 kg drop mass from a height of 1.274 m.

The displacement time histories were obtained from Go-Pro footage by tracking the markers mounted on the trolley and striker. The experimental transient data from the Go-Pro camera was calibrated by means of scaling the curves such that the freefall acceleration equalled 9.81 m/s^2. The resulting displacement and velocity time histories were obtained and plotted in Figure 4.24.

The velocity and acceleration time histories of the striker are shown in Figure 4.25. The acceleration was observed over five velocity frames, with velocity frames observed over three displacement frames. The results showed that the velocity peaked at approximately 4.5 m/s at 35 milliseconds while the acceleration was observed to cap at 80 g at 120 milliseconds. The acceleration time history in Figure 4.25 also showed one sharp peak followed by a constant acceleration, due to gravity as the striker was in freefall at that point.

Based on the results obtained in the experiments, the impact velocity of the striker in the numerical simulation was adjusted to match the experimental data because of frictional losses in the guideways that resulted in a lower impact velocity than expected from ideal free fall velocity. The resulting effect of changing the impact velocity of the striker on the deflection of the door is shown in Figure 4.26. It was found that an impact velocity of 4.8 m/s best fit the experimental data for a drop height of 1.174 m (for frictionless fall).

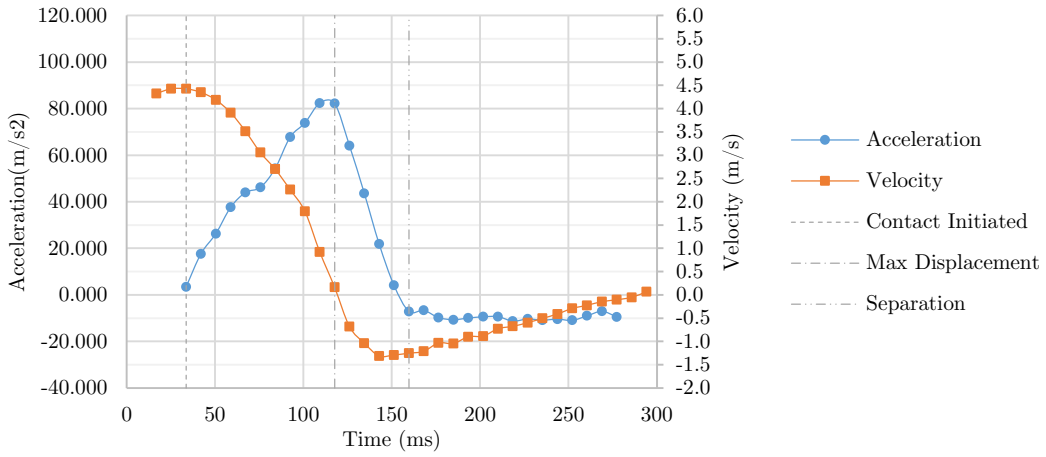

Figure 4.25: Velocity and acceleration time histories of a Ø273 mm striker in an experimental drop test of a 4-door sedan front door with a 385 kg drop mass from a height of 1.274 m.

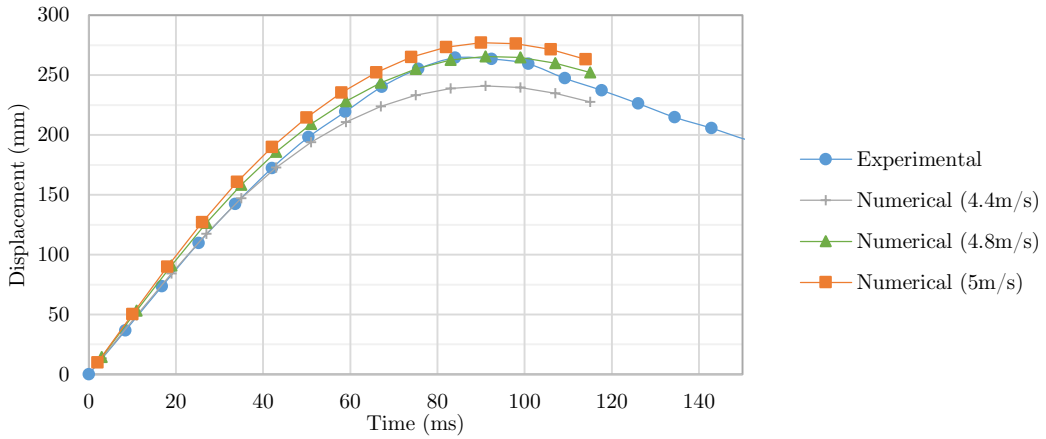

Figure 4.26: Comparison of different impact velocities on numerical deflection results when compared with experimental data of the striker for the unribbed door test rig.

In the subsequent test, the door was located onto I-beam supports, shown in Figure 4.27, which were straightened and reinforced with 10 mm thick steel ribs. Figure 4.28 shows the transient response of the modified door test rig subjected to the similar impact load (drop height of 1.274 m and drop mass of 385 kg). At approximately 200 milliseconds after impact (Figure 4.28(d)) the striker rebounded from the door after initial impact to cause a smaller secondary impact. The striker came to rest at about 498 milliseconds after impact Figure 4.28(e). Analysis of the footage revealed that the striker rebounded three times before coming to rest. The position time histories of the striker, shown in Figure 4.30, were obtained by digitizing the tracked markers from the footage and compared with the results from the numerical model. The deflection time histories of the striker showed excellent correlation between result from the experiment and numerical simulation, thus validating the door model.

Figure 4.27: Reinforced I-beam to stiffen the web section against side-on bending.

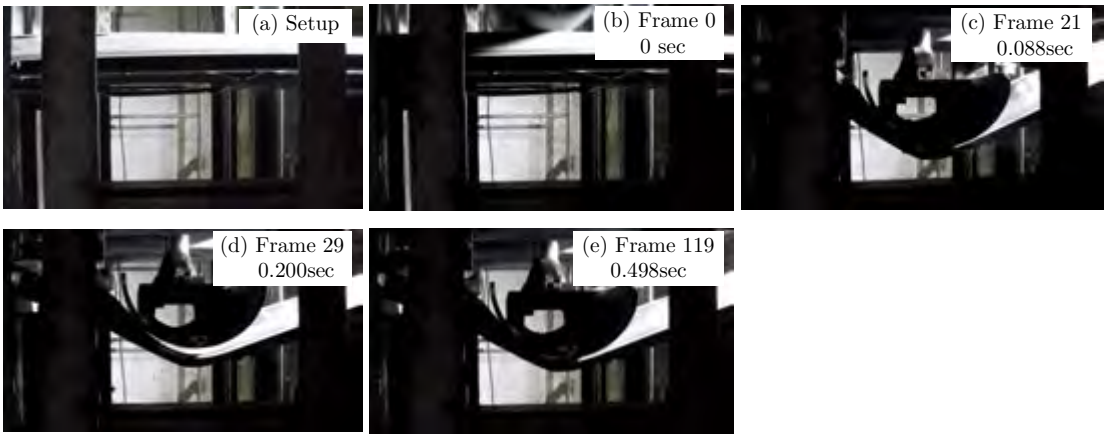

Figure 4.28: Time lapse of drop test impact, (a) before impact, (b) at the point of contact, (c) at maximum deflection, (d) first rebound, (e) once striker is at rest. Frame Rate = 239.0 fps.

An updated numerical model which included flexible ribbed I-beams was created. The updated model, shown in Figure 4.29, was rerun with the same striker mass and impact velocity as in the first experiment and found to deflect inwards by less than 4mm on both the hinged and latch sides of the door.

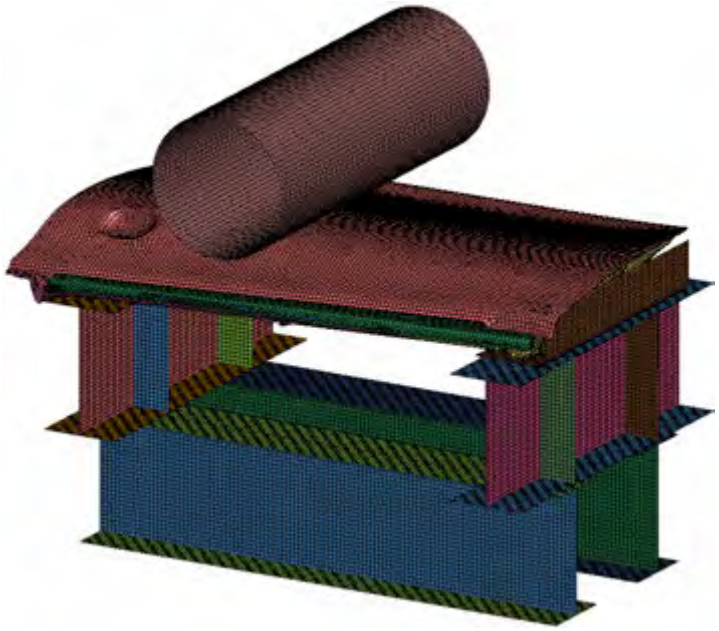

Figure 4.29: Updated numerical model of the experimental door impact test setup with flexible ribbed base structure.

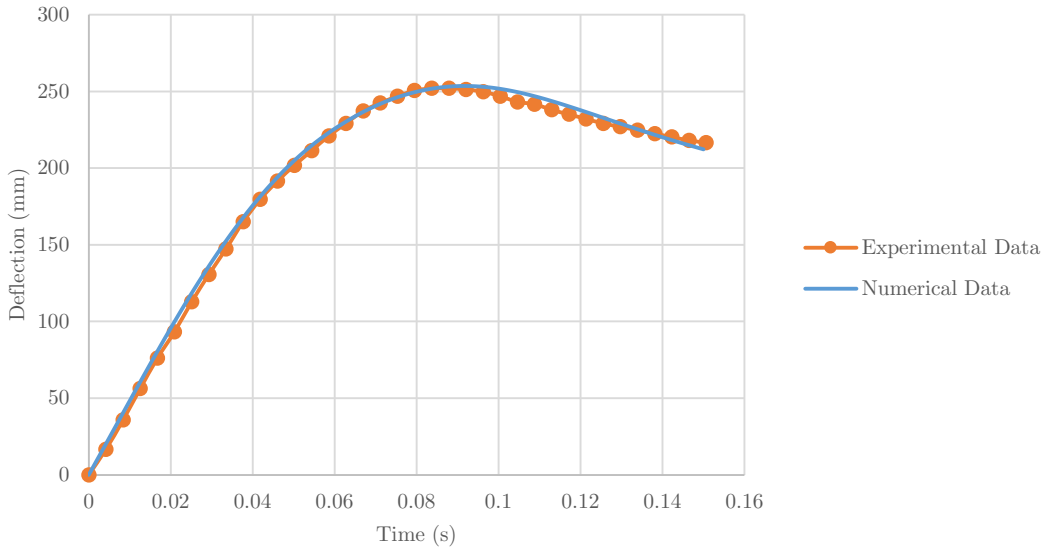

Figure 4.30: Comparison of the numerical and experimental position time histories of the striker for the second door drop test comprising ribbed I-beams for additional strength and rigidity.

4.3 Material Characterisation

The results of the square and round tube material characterisation by means of Scanning Electron Microscopy (SEM) and quasi-static lateral compression tests is discussed in this section.

4.3.1 Scanning Electron Microscopy

The results from the SEM analysis indicated that both square and round tubes had a similar material composition. A sample of the radiation signature from one of the three tests on the round tube is shown in Figure 4.31. The major constitutive material compositions of the square tube, round tube, and door shells using SEM are listed in Table 4.4. Given that the material in all three samples consisted predominantly of Iron, it was assumed that the material was a manganese alloying steel, with Young's Modulus in all three cases of 200 GPa.

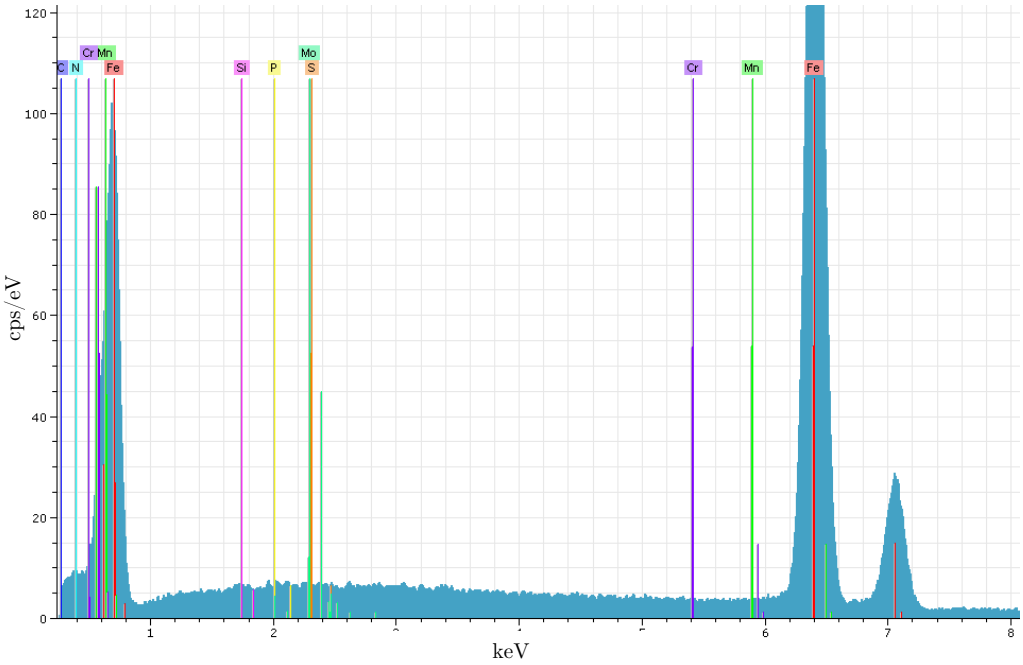

Figure 4.31: Sample results of material compositions test using Energy-Dispersive X-ray spectroscopy (EDS).

Table 4.4: Elemental distributions by weight of predominant elements reported for round tube, square tube, and vehicle outer door shell samples using SEM.

Element	**Round Tube**	**Square Tube**	**Door Shell**
	% by Weight		
Iron	97.6	97.9	98.0
Manganese	1.65	1.40	1.20
Chromium	0.67	0.67	0.71

4.3.2 Lateral Compression Experimental Testing

The force versus deflection histories from the lateral compression experimental tests are shown in Figures 4.32 and 4.33. The weld in the round and square tubes were positioned such that they were subjected to the lowest bending moment possible as per the calculations B.34 and B.40 respectively, in Appendix B1.

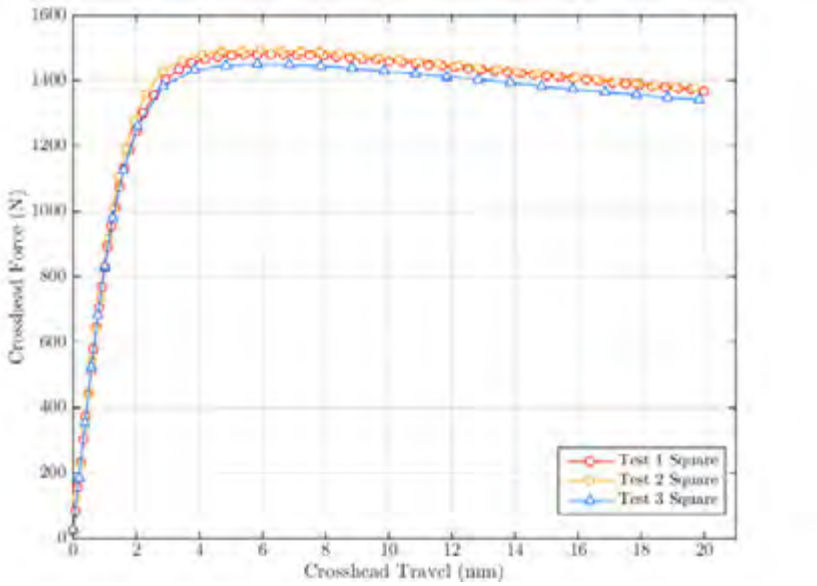

Figure 4.32: Force versus deflection experimental data of a lateral compression test of a square 40×2.0 mm steel tube loaded on its vertex obtained from the Zwick materials testing machine.

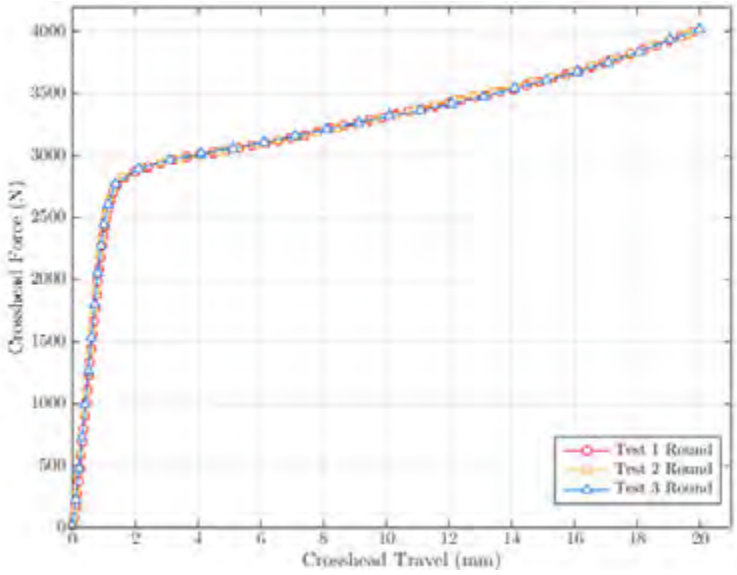

Figure 4.33: Force versus deflection experimental data of a lateral compression test of a round Ø43×2.3 mm steel tube loaded on its vertex obtained from the Zwick materials testing machine.

The Zwick [84] is an elastic entity, as a result the deflection reading from the machine travel comprises the deflection of both the machine and specimen. Consequently the data obtained from the Zwick was processed to subtract the machine compliance. This was achieved by using elastic square tube compression theory discussed in Appendix B2. The analytical solution for the elastic force versus deflection history used to remove the machine compliance and correct the distorted deflection data is given by Equation 4.4 (from equation B.58), assuming that the elastic deflection of the Zwick [84] was linear.

$$\delta = -\frac{Fw^3}{24\sqrt{2}EI} \tag{4.4}$$

Equation 4.4 was used to remove the machine compliance and correct the distorted deflection data. The elastic deflection of the Zwick [84] was assumed linear. The three compression tests conducted on the square tube geometry were averaged and the result was processed to produce the plot shown in Figure 4.34.

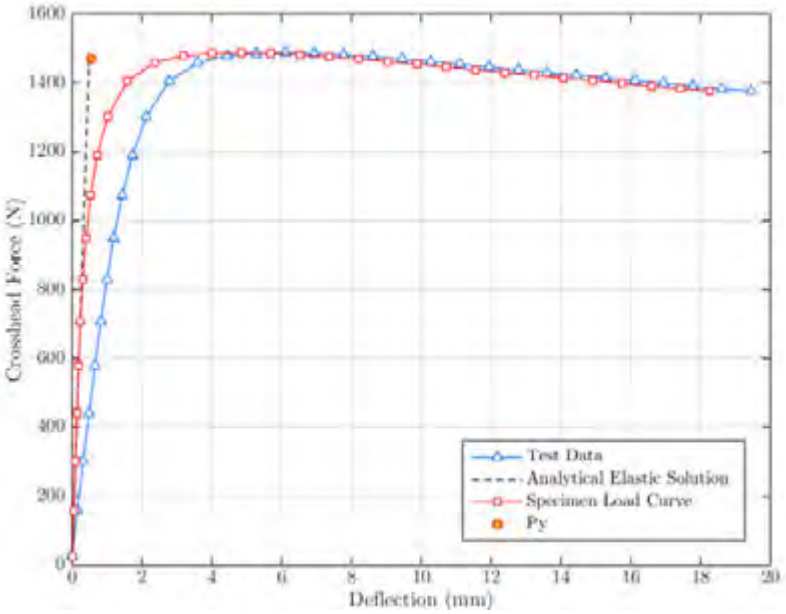

Figure 4.34: Square tube force versus deflection histories before (test data) and after (specimen load curve) removal of machine compliance.

The three compression tests conducted on the square tube geometry were averaged and the result was processed to produce the plot shown in Figure 4.34. The gradient of the Specimen Load Curve was higher than the unprocessed test data after adjusting for machine compliance. The analytical elastic solution from equation 4.4 is plotted in Figure 4.34 as well to show how the onset of plastic deformation causes a deviation from this line.

Similarly, the round tube compression theory as described in Appendix B.1 yields the elastic load deflection relationship given in Equation 4.5, which was used to subtract the machine compliance. The load versus deflection of the three tests was also averaged with similar observations as to the square tube results. The force versus deflection histories for the round tube are shown in Figure 4.35 (from equation B.37).

$$\delta = \frac{0.1488FR^3}{2EI} \tag{4.5}$$

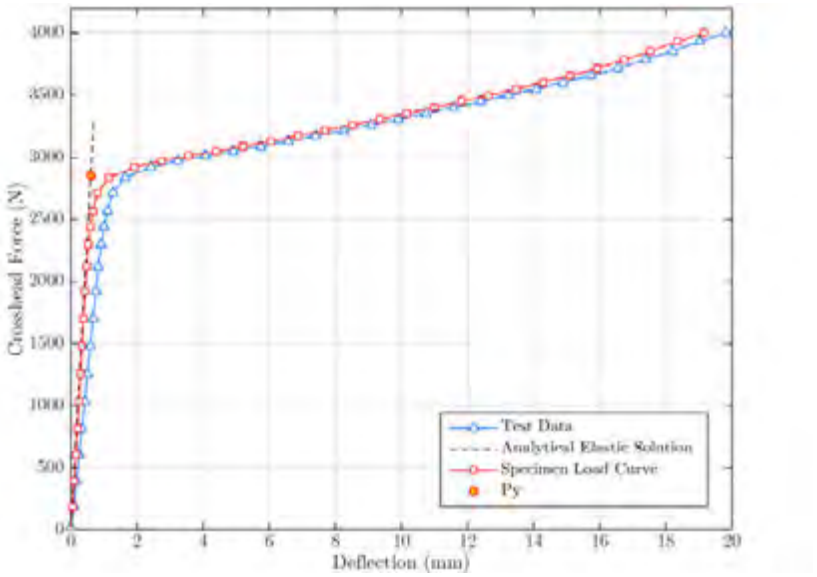

Figure 4.35: Round tube force versus deflection histories before (test data) and after (specimen load curve) removal of machine compliance.

In contrast to a simple tensile test it was only possible to directly determine the yield point from a lateral compression test. The post yield stress-strain relationship was obtained through the use of finite element analysis in conjunction with the experimental data. This was due to the non-linear nature of the resulting force versus deflection relationship obtained from the loading of the specimen geometry.

The lateral crush was simulated incorporating the power-law plasticity model to describe the material behaviour. An 8^{th} symmetry implicit finite element model comprising shell elements with six through thickness integration points and a fully integrated quad and tri element formulation was used to compute the strength coefficient and hardening exponent for the square and round tubes. The fixed and moveable crossheads were modelled as rigid plates. The mesh of the square and round tube specimens in their 8^{th} symmetry and full mirrored form are shown in Figure 4.36.

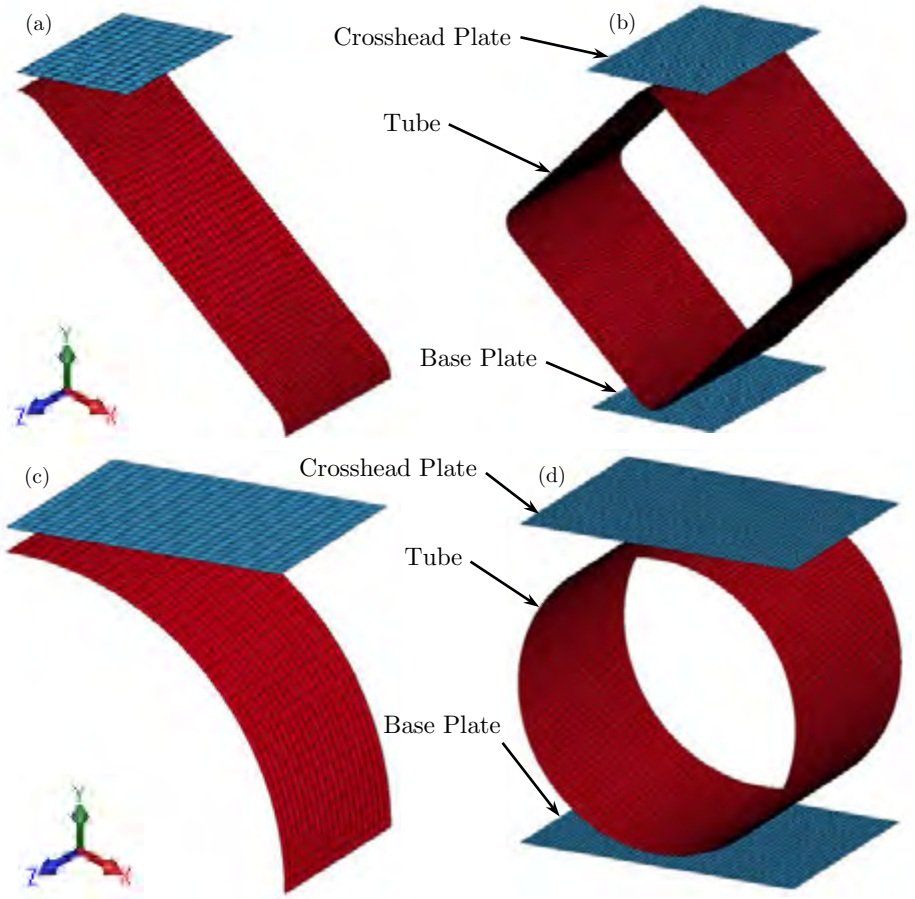

Figure 4.36: 8th Symmetry (a & c) and full mirrored mesh (b & d) for the square 40×2.0 mm steel tube (a & b) and Ø43×2.3 mm round tube (c & d).

A prescribed translational motion was added to the top crosshead plate with only one translational degree of freedom permitted. The displacement and interface force was set to report every 0.5 seconds. Appropriate translational and rotational degrees of freedom listed in Table 4.5 were applied to the symmetry boundaries.

Table 4.5: Degrees of freedom on symmetry boundaries (o: free, x: constrained).

Symmetry Plane	**Rotational Degree of Freedom**			**Translational Degree of Freedom**		
	x	**y**	**z**	**x**	**y**	**z**
x-y Plane	x	x	o	o	o	x
y-z Plane	o	x	x	x	o	o
x-z Plane	x	o	x	o	x	o

The applied rate of deflection of the 8th symmetry model was half that of the full symmetry model due to the x-z symmetry plane, and the resulting force measured at the interface boundary between the plate and tube is one quarter that of the full symmetry model due to the x-y and y-z planes. An automatic surface to surface contact card was used between the plate and tube.

The power-law plasticity model was then optimised to match the post-yield load curve. This was achieved through the use of a topological optimisation program LS-OPT coupled with the finite element solver LS-DYNA. The power-law plasticity model provides elastoplastic behaviour with isotropic hardening. The yield strength, which is a function of the plastic strain may be found from Equation 4.6 [73].

$$\sigma_y = k\varepsilon^n = k\left(\varepsilon_{yp} + \bar{\varepsilon}^p\right)^n \tag{4.6}$$

Elastic strain at yield is calculated using Equation 4.7,

$$\varepsilon_{yp} = \left(\frac{E}{k}\right)^{\left[\frac{1}{n-1}\right]} \tag{4.7}$$

where n is the hardening exponent, k is the strength coefficient and E is Young's Modulus. Due to the material characterisation tests being conducted in the quasistatic regime the effect of strain rate was disregarded. Thus LS-OPT was used to determine the strength coefficient and hardening exponent.

4.3.3 Square Tube Characterisation

A preliminary mesh sensitivity study was conducted on the square tube model using mild steel properties from literature to study and minimise inaccuracies introduced into the computed material parameters whilst keeping computational time within reasonable limits. A mesh sensitivity study is necessary when there is no closed loop feedback from experimental results. One example would be when the numerical simulations are used to determine a set of parameters that cannot be obtained from any other technique and the magnitude thereof is affected by the density of the mesh. In such cases, if there is no other way of verifying the results through experimentation or an analytical approach a mesh sensitivity study is necessary. A trade-off is typically made between accuracy and computational expense. A suitable mesh was then used to determine material parameters from the experiments, followed by a second mesh sensitivity study, this time with material parameters obtained from the optimisation.

Due to the non-linear nature of the problem it is difficult to obtain an analytical solution for the post-yield load versus deflection. However, it is possible to approximate the solution at zero grid spacing using Richardson extrapolation as described in Appendix D [91]. The models used in the mesh sensitivity study contained an average grid spacing of 0.4 mm, 0.2 mm, and 0.1 mm as

illustrated in Figure 4.37. All three meshes were scaled with respect to each other and contain a mix of quadrilateral and triangular elements. A total of 100 temporally evenly spaced crosshead force measurements summed to compute the numerical solution. The results are listed in Table 4.6.

(a) (b) (c)

Figure 4.37: (a) Coarse, (b) medium, and (c) fine meshes for the mesh convergence study of the square tube material characterisation model.

Table 4.6: Mesh convergence results for the square tube material characterisation numerical model.

Mesh	Mesh Spacing (mm)	Numerical Solution (N)	Accuracy (%)	CPU Time
Coarse	0.4	155.90	99.17	1 hr 17 min
Medium	0.2	155.45	99.47	11 hrs 47 min
Fine	0.1	155.15	99.66	81 hrs 45 min

The results showed that for even the coarsest mesh used the accuracy when compared with the mesh independent solution was 99.17%. A CPU time of 1 hour and 17 minutes was also acceptable given that 2 CPU's were used for each simulation and convergence of the material parameters occurred after approximately eight iterations. Thus making the total runtime for the determination of the material parameters at approximately 10 hours.

The coarse mesh was used to obtain the square tube material properties. A strength coefficient and hardening exponent of $k = 335\,MPa$ and $n = 0.065$ respectively, were found to best fit the experimental load curve. The experimental and optimised numerical load curve for the square tube is plotted in Figure 4.38. The sensitivity of the values of k and n are shown in Figures 4.39 and 4.40.

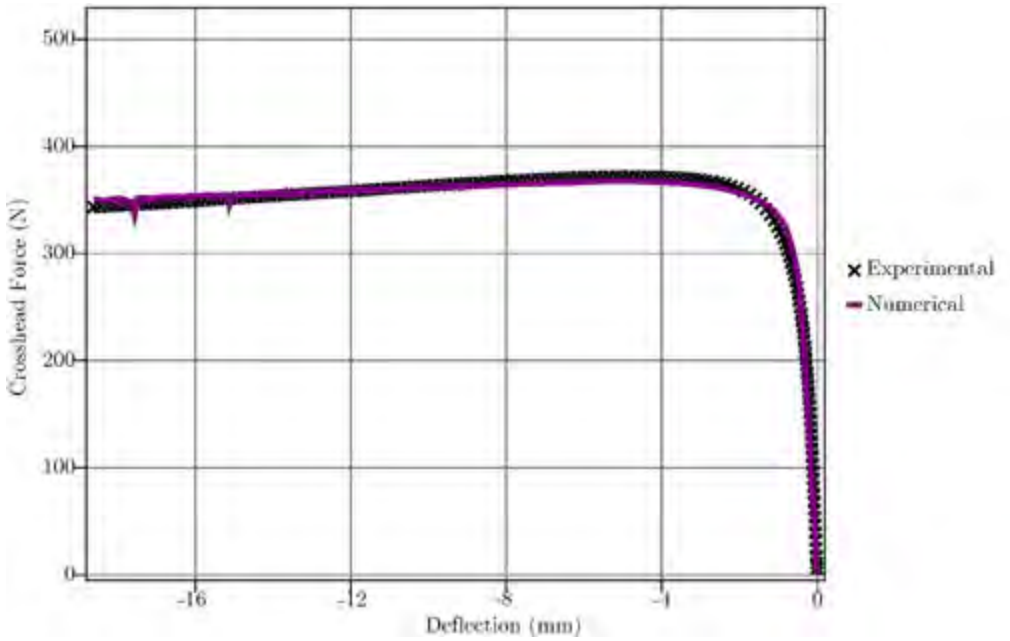

Figure 4.38: Square tube numerical and experimental force versus displacement curves for k=335 MPa and n=0.065.

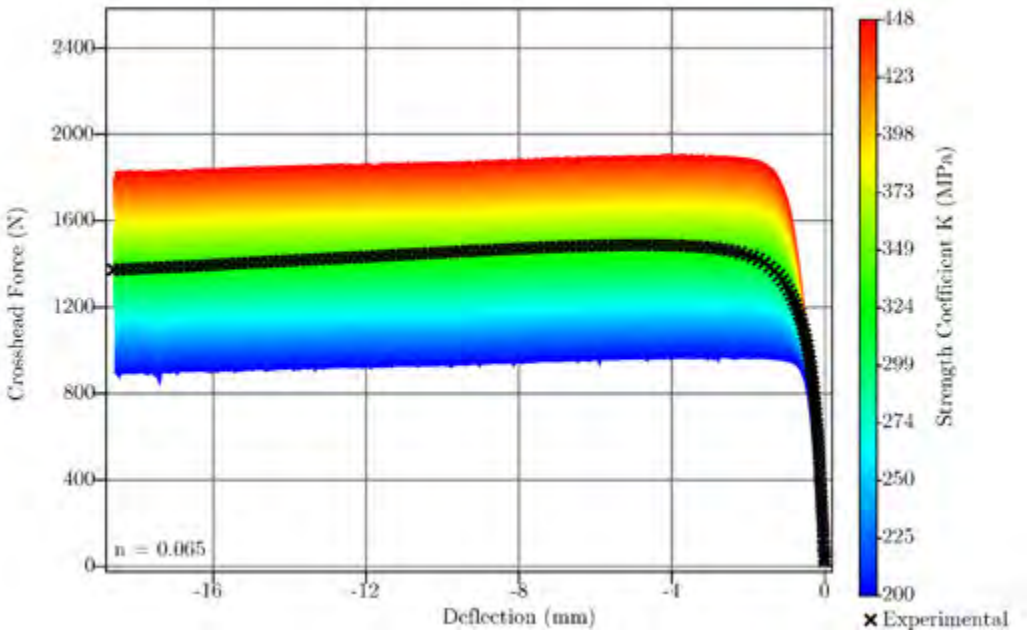

Figure 4.39: Effect of strength coefficient K on the force versus deflection for a hardening exponent n=0.065, for square tube.

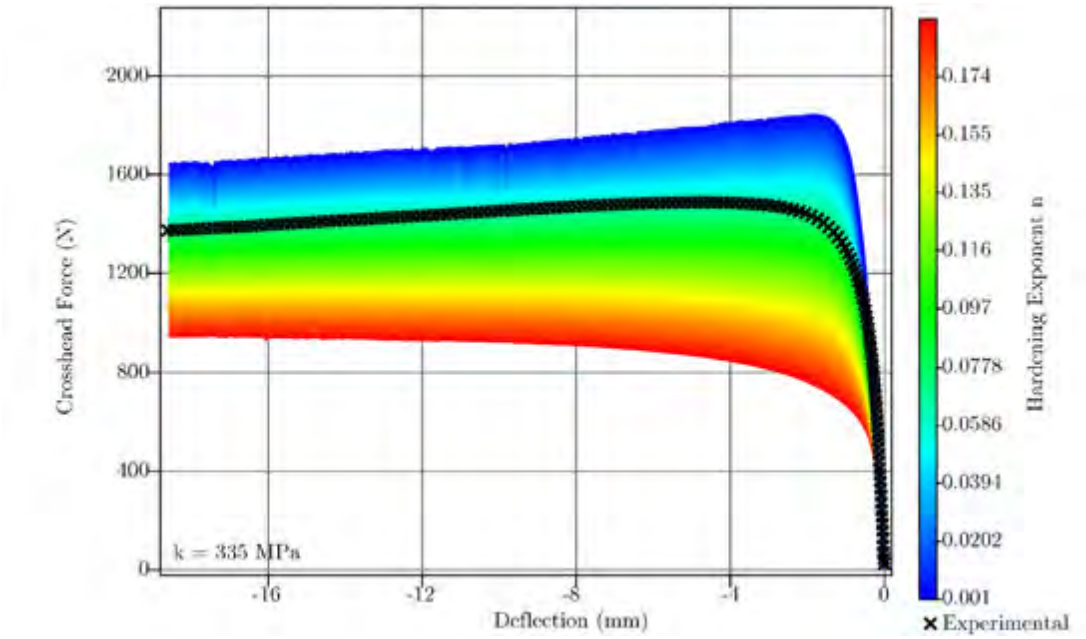

Figure 4.40: Effect of hardening exponent n on the force versus deflection for a strength coefficient of k=335 MPa, for square tube.

The contour plots illustrated in Figures 4.39 and 4.40 show that the hardening exponent affected the curvature of the yield point with a lower value exhibiting a sharper curvature, the overall post yield load also increased with a reduction in the hardening exponent. Converse to the hardening exponent the strength coefficient only affected the force on the crosshead after yield, giving a fairly consistent curve. A notable difference between the hardening exponent and strength coefficient is that although the hardening exponent had a strong effect at yield the bandwidth of results from n=0.001-0.174 narrowed as the post-yield deflection increased. This is in contrast with the strength coefficient which maintained a relatively constant bandwidth throughout the post-yield deflection range.

4.3.4 Round Tube Optimisation

Similar to the square tube material characterisation, a mesh convergence study was also conducted on the round tube using Richardson extrapolation to obtain the mesh independent solution for the purpose of determining the accuracy of the results from the round tube meshes. The three meshes illustrated in Figure 4.41, used grid spacing's of 0.8 mm, 0.4 mm, and 0.2 mm for the coarse, medium and fine meshes respectively. All three meshes were scaled with respect to each other and contain only quadrilateral elements.

Figure 4.41: (a) Coarse, (b) medium, and (c) fine meshes for the mesh convergence study of the round tube material characterisation model.

Results from the mesh sensitivity study as well as the Richardson extrapolation calculations are given in Table 4.7. The same approach as with the square tube mesh sensitivity study was used with 100 temporally evenly spaced crosshead force measurements summed to compute the numerical solution.

Table 4.7: Mesh convergence results for the round tube material characterisation numerical model.

Mesh	**Mesh Spacing (mm)**	**Numerical Solution (N)**	**Accuracy (%)**	**CPU Time**
Coarse	0.8	325.56	98.62	55 min
Medium	0.4	324.11	99.07	12 hrs 46 min
Fine	0.2	323.13	99.38	23 hrs 44 min

The coarsest mesh is sufficiently accurate at 98.62%. This is an acceptable variation with CPU time under 1 hour. The round tube optimisation study took approximately 15 iterations to converge as opposed to eight iterations for the square tube optimisation. This doubled the computational time despite having double the mesh spacing for the equivalent mesh when compared to the square tube numerical model. When superimposing the results from the three meshes on one another the variation was sufficiently small that the line thickness made it difficult to distinguish between results. A plot of the accuracy of each of the three solutions on a log scale is shown in Figure 4.42.

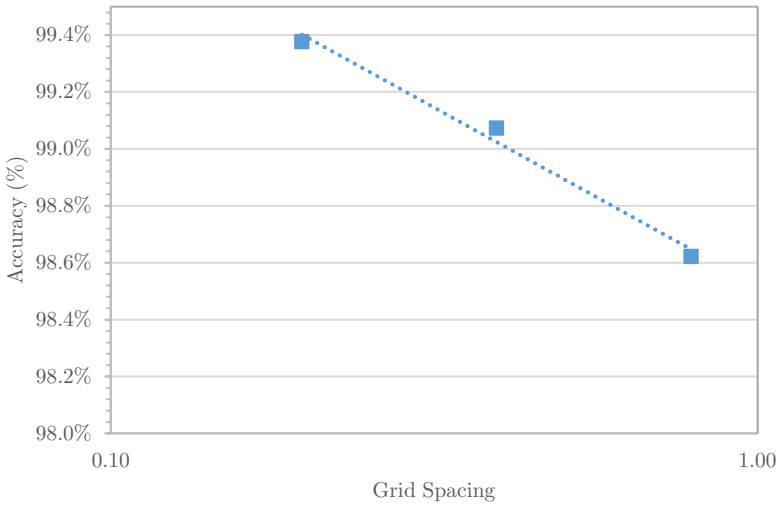

Figure 4.42: Comparison of the accuracies of the coarse, medium and fine meshes for the round tube material characterisation model.

The graph, plotted in Figure 4.42, shows that with decreasing grid size accuracy increases. A zero mesh size indicates that the results obtained from the numerical study are no longer subject to inaccuracies due to the mesh. The coarse mesh was used to conduct the round tube optimisation study. The optimal strength coefficient and hardening exponent were found to be $k = 472\,MPa$ and $n = 0.078$ respectively. The corresponding numerical and experimental geometric load curves are superimposed on one another in Figure 4.43. The sensitivities of the Strength coefficient and hardening exponent are shown in Figures 4.44 and 4.45. For the square tube results shown in Figure 4.44 and 4.45, the strength coefficient and hardening exponent have an inverse effect on the crosshead force with respect to each other. The hardening exponent had a far less effect on yield load curvature for the round tube than the square tube.

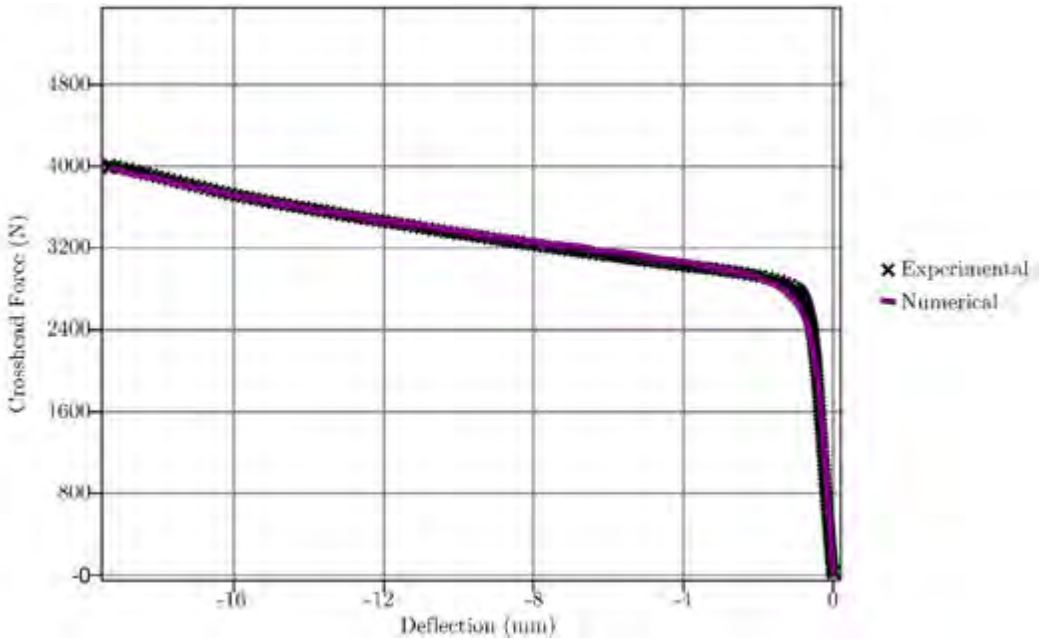

Figure 4.43: Round tube numerical and experimental force versus displacement curves for k=472 MPa and n=0.078.

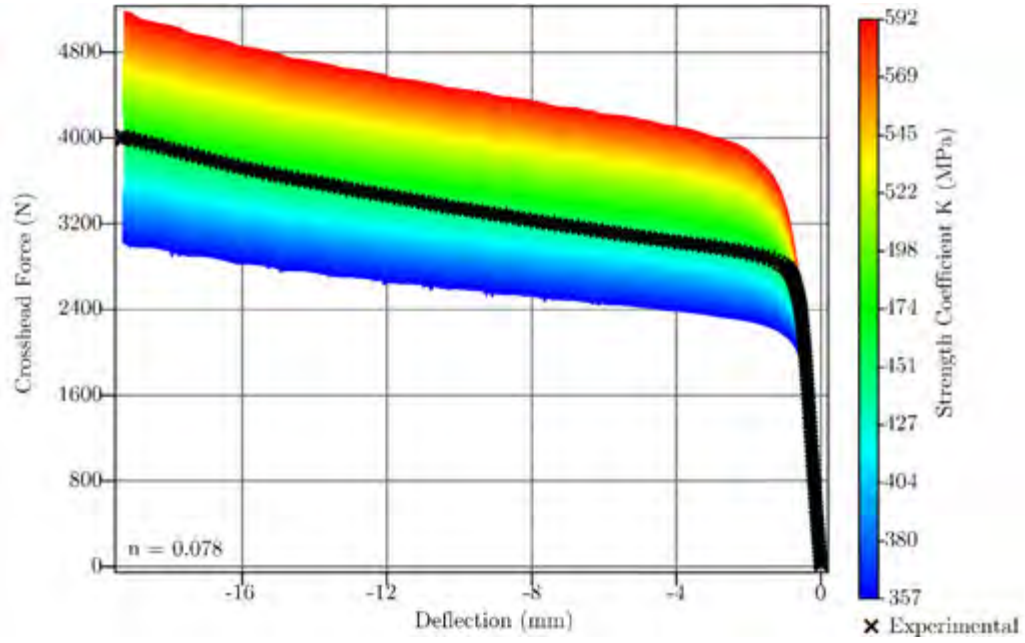

Figure 4.44: Effect of strength coefficient K on the force versus deflection for a hardening exponent n=0.078, for round tube.

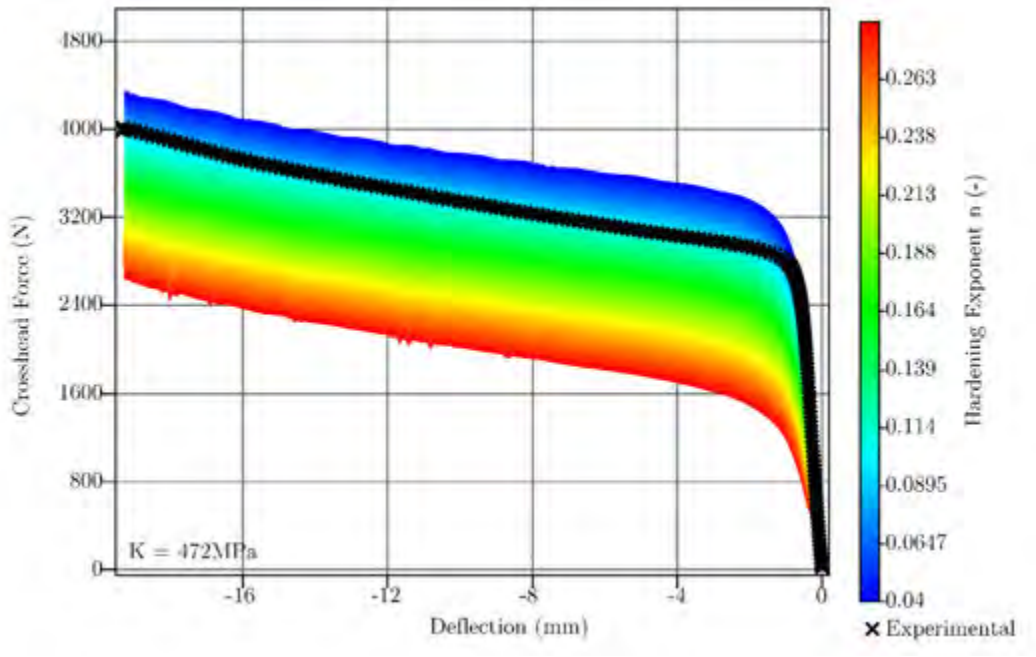

Figure 4.45: Effect of hardening exponent n on the force versus deflection for a strength coefficient of k=472 MPa, for round tube.

4.3.5 Summary of Material Characterisation Results

The strength coefficient and hardening exponent obtained from the quasi-static lateral compression tests on the square and round tube material is presented in Table 4.9.

Table 4.8: Result of material characterisation of the square and round tube materials.

Material	Strength Coefficient (MPa)	Hardening Exponent (-)
Square Tube	335	0.065
Round Tube	472	0.078

4.4 Side Impact Beam Drop Tests

The side impact beam was identified as one of the single highest energy absorbing components in a side impact collision and was chosen for optimisation. Consequently a separate finite element model of the side impact beam was developed to minimise computational expense. The side impact beam model was setup to subject the tube to lateral impact of a striker similar to that of the simplified door model. The tube exhibited bending behaviour characteristic of a simply supported beam subjected to an off centre impact load. Therefore a simple support mechanism, shown in Figure 4.46, was designed to support the tube on the existing door test rig. The resulting design was bolted directly to the I-beam structure from the door test rig. The support structure consisted of a M16 hex socket bolt and nut on one end, and a pivoted pillow block on the other end with an interchangeable Teflon insert. The Teflon insert facilitated testing of square and round tubes of size 40×2.0 mm and 43×2.3 mm respectively. The bolted end allowed for a maximum angular rotation of 43.6° for the 43mm diameter round tube.

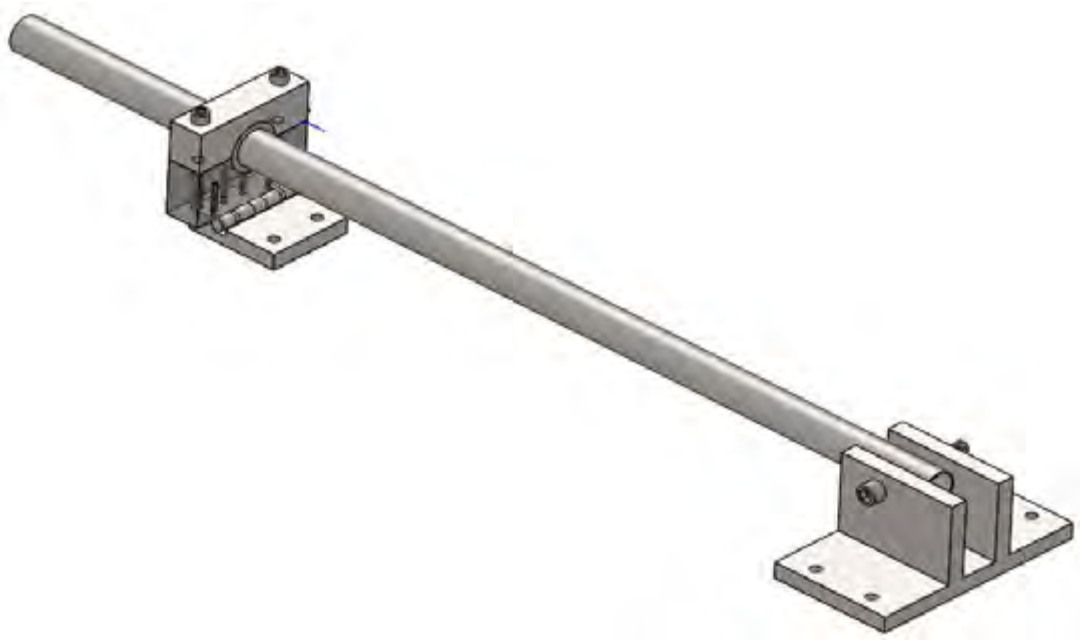

Figure 4.46: Side impact beam and support structure to be bolted to the existing I-beam support base.

4.4.1 Numerical Model Setup

An explicit finite element model with shell elements containing six through thickness integration points and a fully integrated quad and tri element formulation was used to simulate the side impact beam. The model provided the transient response of the square and round tubes subjected to impact of a 200 kg drop mass at velocities ranging between 1.8-2.8 m/s. The striker, endplate and pillow block were modelled as rigid material to keep computational times to a minimum. The endplate was an idealisation of an M16 bolted pivot, where the bolt was lightly greased to facilitate free rotation. The purpose of the endplate was to connect the end nodes to facilitate rigid body motion of the nodes. One node in the centre of the endplate was constrained about all degrees of freedom except the rotational x-axis to impose the bolted pivot boundary condition. The pillow block was free to rotate about its pivoted edge. The square and round tube meshes are shown in Figure 4.47.

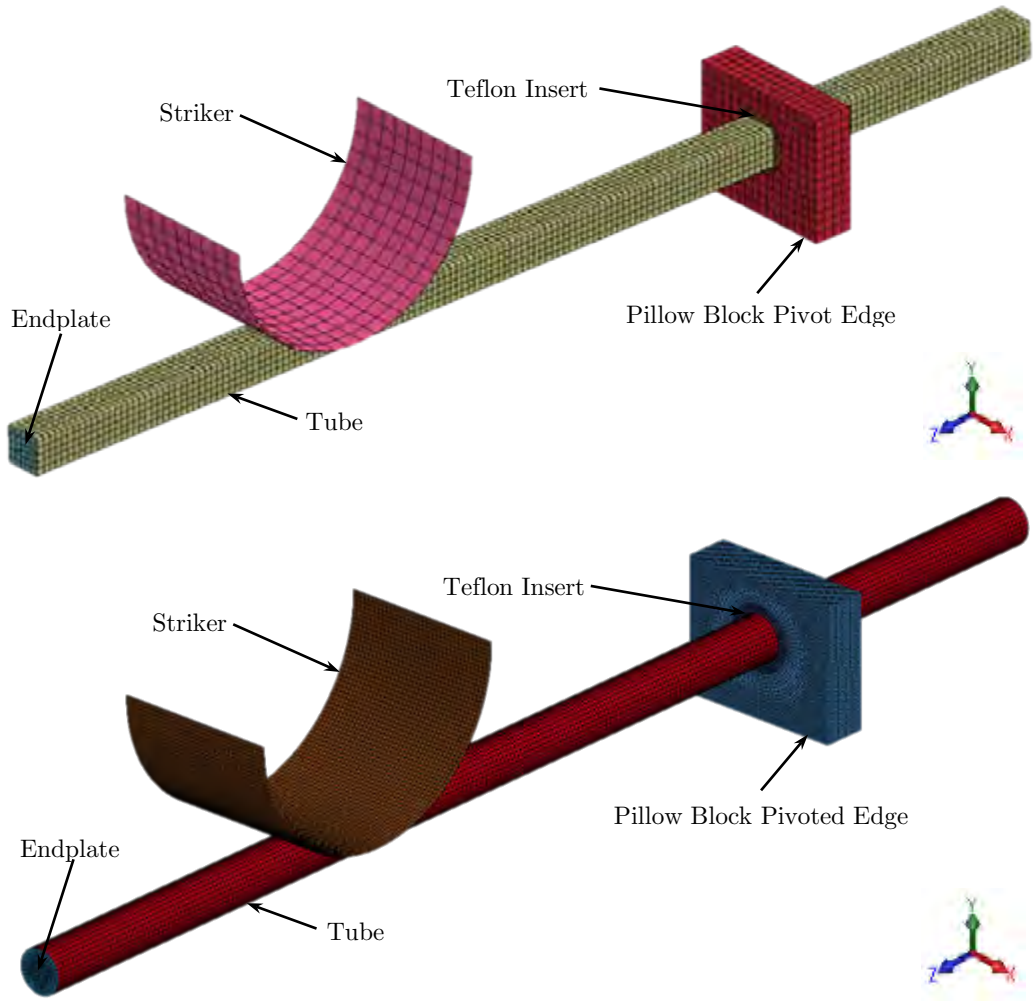

Figure 4.47: 40×2.0 mm Square tube (6.9 mm mesh spacing) and Ø43×2.3 mm round tube (4 mm mesh spacing) side impact beam finite element model and setup.

The striker is modelled as a 1mm thick shell with scaled density for a mass of 200 kg. Gravity was also added to the model in the y-direction. An automatic surface to surface contact was used between the striker and tube, pillow block and Teflon insert, as well as Teflon insert to tube. Nodes were merged between the endplate and tube enabling a rigid coupling. The impact duration of the simulations was initially set to 0.15 seconds but later varied for each drop height as the tubes were found to reach a state of equilibrium at different times depending on the impact conditions. These durations are given in Table 4.9.

Table 4.9: Simulation times for square and round tube drop tests based on high speed camera footage for different drop heights.

	Simulation Duration (Seconds)	
Drop Height (mm)	**Round Tube**	**Square Tube**
250	0.12	0.09
300	0.12	0.09
350	0.13	0.11
400	0.14	0.12
450	0.17	0.13
500	0.18	0.14

4.4.2 Mesh Sensitivity Studies

Mesh sensitivity studies were conducted on the square and round tube numerical models to study the effect of friction between the tube and striker. The coefficient and exponent values for the Plastic Kinematic Hardening component of the Power-Law plasticity model for mild steel were employed. The Richardson extrapolation technique was used to determine the mesh independent solution to calculate the error of each of three progressively refined meshes. The studies conducted on the square and round tubes are presented in tandem for comparative purposes. A sample of the scale of the element sizes for the six meshes used are shown in Figure 4.48.

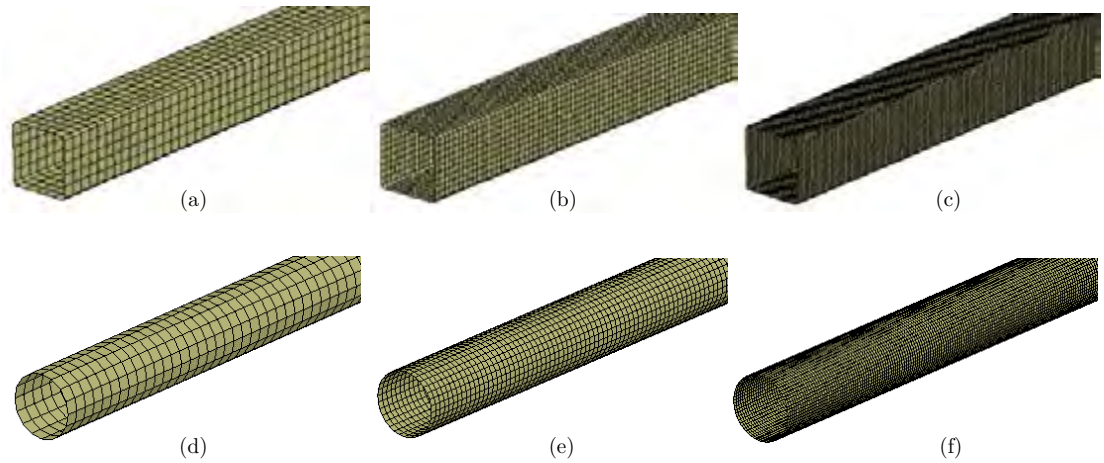

Figure 4.48: Sample of three square tube meshes and three round tube meshes for the mesh sensitivity studies for the tube drop tests, with average grid spacing (a) 6.9 mm square, (b) 3.8 mm square, (c) 2.0 mm square, (d) 8 mm round, (e) 4 mm round, (f) 2 mm round tube meshes.

Each simulation was run on four AMD Opteron 6274 CPU's clocked at 2.20 GHz on a Dell Enterprise C6145 machine with results listed in Table 4.10. The numerical solution used by the Richardson extrapolation technique was the maximum absorbed energy of the model. The results showed a variation in the maximum absorbed energy of 2.80% for the square tube and 2.09% for the round tube with respect to the mesh independent solution. The coarsest (6.9 mm) square tube mesh and the medium round tube mesh (4 mm) was chosen from the mesh sensitivity studies. Although the error was small for the coarse round tube mesh, a qualitative observation revealed that there were too few elements to adequately capture buckling, as illustrated in Figure 4.49(b).

Table 4.10: Mesh convergence results for the square and round tube drop test numerical models.

Geometry	**Mesh**	**Mesh Spacing (mm)**	**Energy Absorption (kJ)**	**Accuracy (%)**	**CPU Time**
Square Tube	Coarse	6.9	733	97.20	8 hrs 39 min
	Medium	3.8	721	98.88	29 hrs 57 min
	Fine	2.0	716	99.58	256 hrs 41 min
Round Tube	Coarse	8.0	704	97.91	1 hr 43 min
	Medium	4.0	692	99.65	13 hrs 59 min
	Fine	2.0	690	99.94	101 hrs 5 min

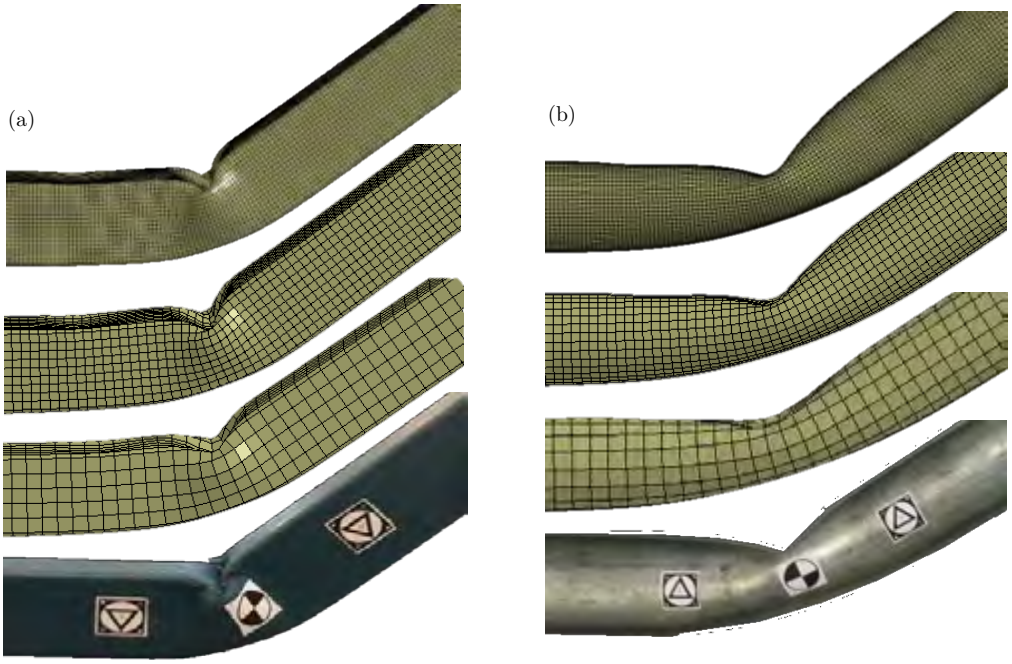

Figure 4.49: Comparison of buckled (a) square and (b) round tubes from 500 mm drop height.

4.4.3 Numerical Validation

The FE model of the lateral impact test was compared to an analytical solution in the linear elastic loading regime early on during model creation (prior to modelling plastic deformation) to determine whether the model was producing plausible results. Two solutions were derived, one by using the internal energy method and the other by applying the linear load deflection assumption. The derivation of each of the two solutions is given in Appendix A. The result of the two analytical solutions were compared against the output from the numerical solver and are given in Table 4.11.

Table 4.11: Comparison of different methods of determining the maximum transverse deflection given the application of an impact load.

		Analytical Solution		**Numerical Solution**
Drop Mass (kg)	**Impact Velocity (m/s)**	**Internal energy Method (mm)**	**linear load deflection assumption (mm)**	**LS-DYNA (mm)**
50	1	8.8	7.9	8.5
250	1	19.7	19.3	21.1

Once the material exceeded the yield point or there were any non-linear geometric effects the solver solution began to diverge from the analytical solution.

A study was conducted to determine the effect, if any, of friction between the striker and side impact beam on the outcome of the simulation. The result for two cases, namely zero friction, and steel-to-steel friction coefficient as per the literature [92] is shown in Figure 4.50. Figure 4.50(a) shows the response of the tube within the passenger door from the impact simulation of the full vehicle model. Figure 4.50(b) shows the response of a tube out of the door to impact loading where friction is defined as 0.57 and 0.74 for dynamic and static coefficients of friction respectively, as per the literature for contact between two steel specimens [92]. Although the tube buckled in approximately the same location as the tube in the door, it was also subjected to tube flattening which was not apparent in the tube-in-door simulation in Figure 4.50(a).

The result of an updated side impact beam model with a finer mesh (64 circumferential nodes) and without friction is shown in Figure 4.50(c). The tube with finer mesh deflected 12% more with the striker appearing to climb up one side of the tube away from the buckling point as shown in Figure 4.50(c). In the results shown Figure 4.50(d), the same co-efficient of friction as used for Figure 4.50(b) was applied and a finer mesh (64 circumferential nodes) was used for the side impact beam. The finer mesh did not produce different results as both setups yielded the same results for SEA and transverse deflection. It was found that that the performance of the tube was very dependent on the contact friction coefficient between the striker and tube. It also showed that higher coefficients of friction result in tube flattening which was not consistent with the tube within the door.

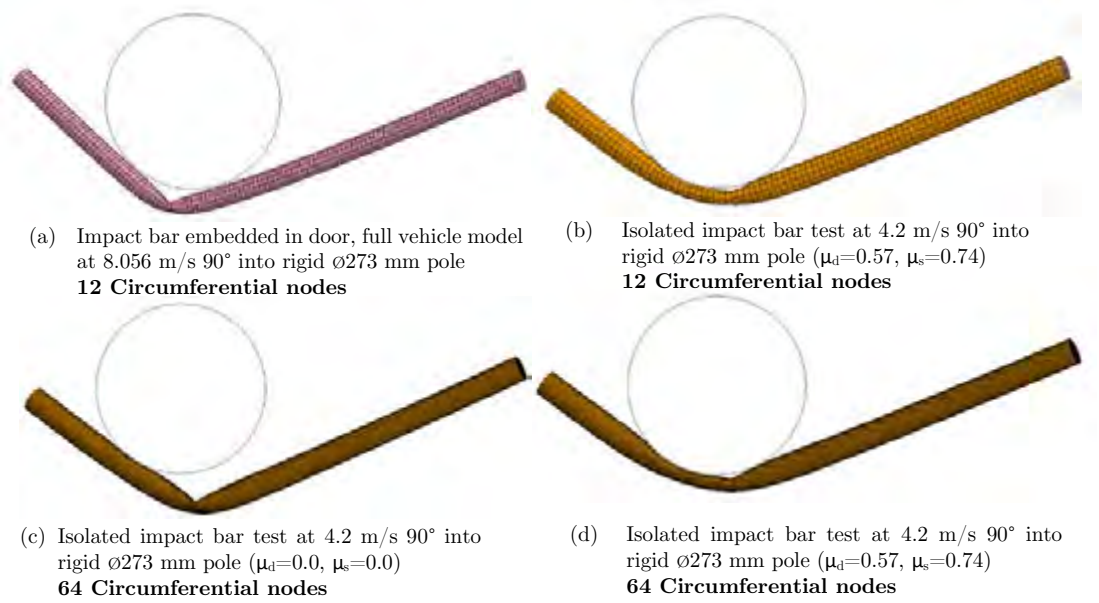

(a) Impact bar embedded in door, full vehicle model at 8.056 m/s 90° into rigid ø273 mm pole
12 Circumferential nodes

(b) Isolated impact bar test at 4.2 m/s 90° into rigid ø273 mm pole (μ_d=0.57, μ_s=0.74)
12 Circumferential nodes

(c) Isolated impact bar test at 4.2 m/s 90° into rigid ø273 mm pole (μ_d=0.0, μ_s=0.0)
64 Circumferential nodes

(d) Isolated impact bar test at 4.2 m/s 90° into rigid ø273 mm pole (μ_d=0.57, μ_s=0.74)
64 Circumferential nodes

Figure 4.50: Comparison of different simulations with each other.

4.4.4 Frictional Effects

In the simplified side impact beam model the tube began to buckle at 0.018 seconds after impact for a 400 kg drop mass with static and dynamic friction coefficients of 0.74 and 0.57 respectively [92], as opposed to 0.03 seconds with the impact beam embedded in the door. Local flattening of the tube was observed in the region where contact was made with the striker. The resulting variation in modes of failure caused a large discrepancy in the total energy absorbed between the two tests. The observed tube flattening was strongly affected by the magnitude of the coefficients of friction. For this reason the contact surfaces of the striker and impact beam are lubricated to minimise this effect. According to the literature the coefficient of friction for steel on steel contact for greasy surfaces is in the range of 0.09-0.19 [92]. A parametric study was subsequently conducted to study the effect of friction coefficients in the range of 0.1-0.18 for different drop masses at an impact velocity of 4.2 m/s.

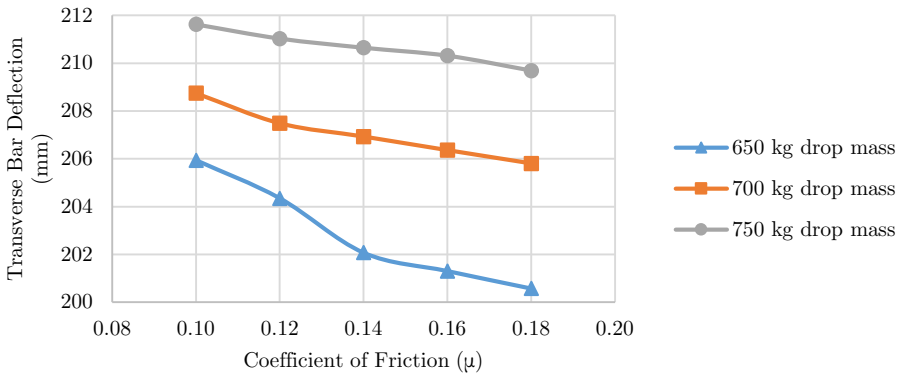

Figure 4.51: Transverse beam deflection versus coefficient of friction for different drop masses at an impact velocity of 4.2 m/s onto a simply supported impact beam.

Figure 4.51 shows that for a 650 kg drop mass the deflection varied by approximately 3% over the range of friction coefficients while the deflection due to the 700 kg and 750 kg drop masses varied by approximately 1.3% and 0.9% respectively. This showed that the effect of friction for higher drop masses reduced within a friction coefficient range of 0.10 and 0.18.

4.4.5 Experimental Testing of Square and Round Tubes

Square 40×2.0 mm and round 43×2.3 mm side impact beam tubes were experimentally tested. The tubes were impacted with a striker of mass 200 kg at incrementally varying heights of 250 mm, 300 mm, 350 mm, 400 mm, 450 mm and 500 mm. Due to frictional losses between the guides the impact velocities were lower than the theoretical maximum. The impact velocities in the numerical models were set as design parameters and optimised in LS-Opt to match the transient response of the tubes obtained from footage of the experimental tests. The results are tabulated in Table 4.12.

Table 4.12: Round and square tube impact velocities, idealised based on drop height and inferred through displacement measurements versus time.

Experimental Drop Height (mm)	Idealised Impact Velocity (m/s)	Actual Impact Velocity (m/s)		Maximum Deflection (mm)	
		Round Tube	Square Tube	Round Tube	Square Tube
250	2.215	1.914	1.831	65	67
300	2.426	1.933	2.098	74	79
350	2.620	2.139	2.250	91	100
400	2.801	2.355	2.575	116	117
450	2.971	2.542	2.684	149	145
500	3.132	2.728	2.721	208	167

A total of six round tubes and 22 square tubes were tested. The tubes were seam welded along one edge. The effect of the seam weld on the response of the tube to lateral impact was studied by means of orientating the welds at different edges relative to the impacted side. The tube deflection was

measured as the maximum transverse deflection of the beam from its unstressed pre-test state. Figure 4.52 shows the round tubes after impact testing placed side-by-side. The impacted tubes, shown in Figure 4.52, were placed in decreasing drop height from top to bottom. The results showed that with increasing drop height (and impact velocities) the transverse deflection also increased as expected. Buckling was observed for all six round tubes at approximately 835mm from the free end (where the impactor struck the side impact beam). The maximum deflections for each round tube test was plotted in Figure 4.53. The data fitted a quadratic trend with an R-square value of 0.96. A quadratic fit was a better option because of the square velocity relationship with drop height.

Figure 4.52: Ø43×2.3 mm Round tube drop test results with incrementally varying drop heights from 250-500 mm.

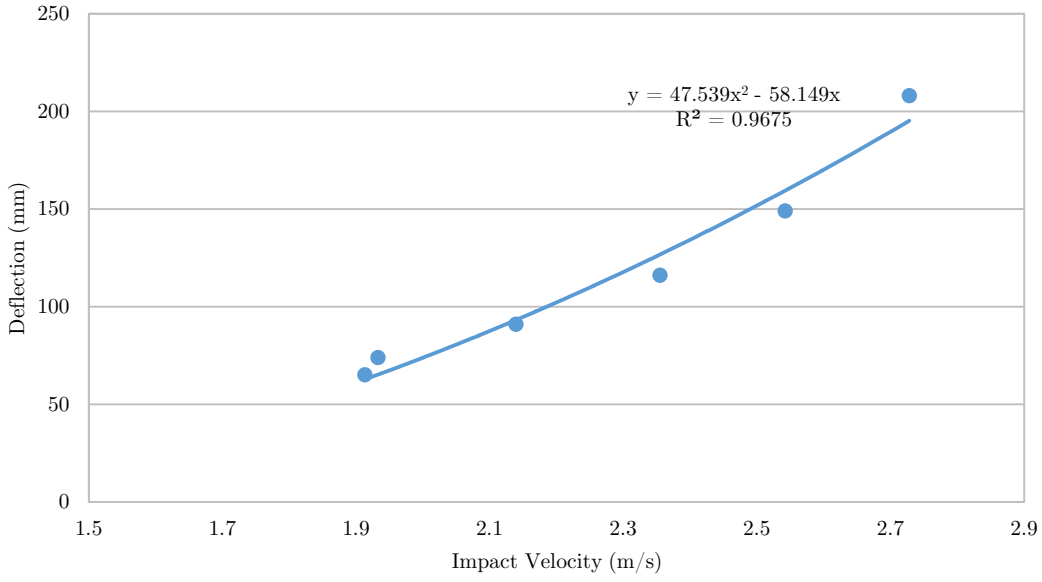

Figure 4.53: Effect of transverse deflection of a Ø43×2.3 mm round tube subjected to lateral impact of a 200 kg mass with different impact velocities.

A photograph picturing the deformed square tubes subjected to drop tests (drop mass 200 kg and drop heights ranging between 250 mm and 500 mm) is shown in Figure 4.54. Localised buckling in the impacted region was observed in all tests. The side of the tube in the buckling region bulged outwards while the top face indented. The deformation pattern the square tubes was similar to the round tubes. A plot of the maximum deflections versus impact velocities for the square tubes is shown in Figure 4.55. The data showed a similar trend as with the round tube tests, where the transverse deflection increased with increasing impact velocities. A quadratic trendline was fitted and found to have an R-square value of 0.92.

Figure 4.54: 40×2.0 mm Square tube drop test results with incrementally varying drop heights from 250-500 mm.

The two sets of results are superimposed in the graph shown in Figure 4.56 for comparison. The square and round tubes were found to deflect by the similar amount for impact velocities ranging between 1.9 and 2.2 m/s. For higher impact velocities, but the square tube deflected less than the round tube.

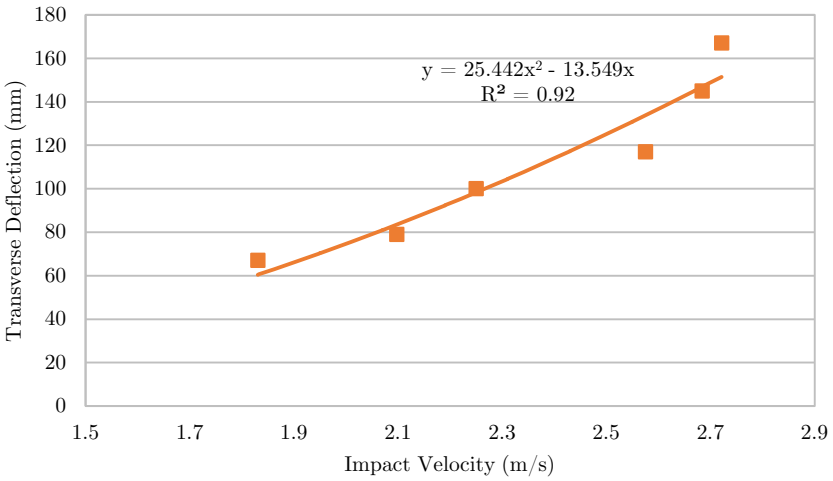

Figure 4.55: Effect of transverse deflection of a Ø40×2.0 mm square tube subjected to lateral impact of a 200 kg mass from different drop heights.

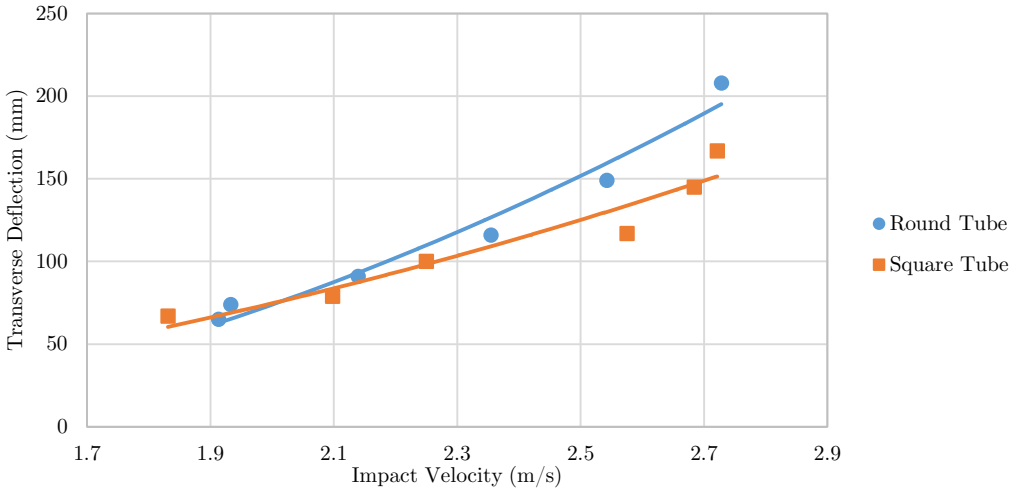

Figure 4.56: The superimposition of the result of the transverse deflection of a Ø40×2.0 mm square and Ø43×2.3 mm round tube subjected to lateral impact of a 200 kg mass from different drop heights.

The transient response of the tubes were recorded using the Photron FASTCAM-APX RS2 [93] at 7500 fps with a resolution of 768×528. The tube and striker were marked with laser printed tracking markers which were adhered to the surface with double sided tape. The markers were then tracked using a video analysis and modelling tool called Tracker 4.91 [94]. The transient displacement response of the square and round tubes are shown in Figure 4.57 and 4.58.

The graphs in Figures 4.57 and 4.58 showed that the tubes displaced to a maximum, and then oscillated about the maximum deflection before coming to rest. The final unstressed deflection was measured after the weight of the striker was removed. The displacement-time histories were differentiated to produce the velocity versus time histories, shown in Figures 4.59 and 4.60 for the square and circular tubes respectively. The velocity averaging over three displacement frames gave the best balance between noise and accuracy for both square and round tube histories. The results showed considerable transient vibration about the impact velocities in the first 20 milliseconds after impact due to noise/ringing in the system. Thereafter the velocity of the striker decreased upon contact with the tubes before oscillating about 0m/s and eventually came to a state of equilibrium.

The acceleration-time histories of the striker were obtained by differentiating the data from the velocity-time histories. The data processed over two velocity-time frames (equivalent to seven displacement-time frame). The results are shown in Figures 4.61 and 4.62 for both the square and circular tubes respectively. The magnitude of the acceleration for the test from a 500 mm drop height was at a maximum at impact until approximately 0.1 seconds for the test corresponding to the striker making contact to with the tubes. A second peak occurred in the opposite direction at approximately 0.18 seconds when the striker rebounded. Thereafter the acceleration went to 0 m/s^2 when the striker rested on the tube.

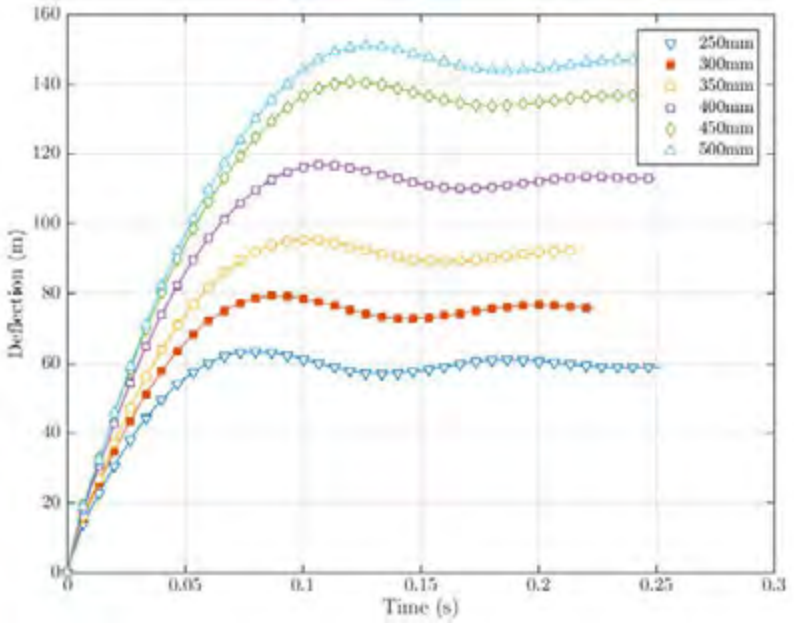

Figure 4.57: Transverse deflection time histories of a 40×2.0 mm square tube struck at approximately one third of the length from the fixed pivot with a mass of 200 kg at different drop heights.

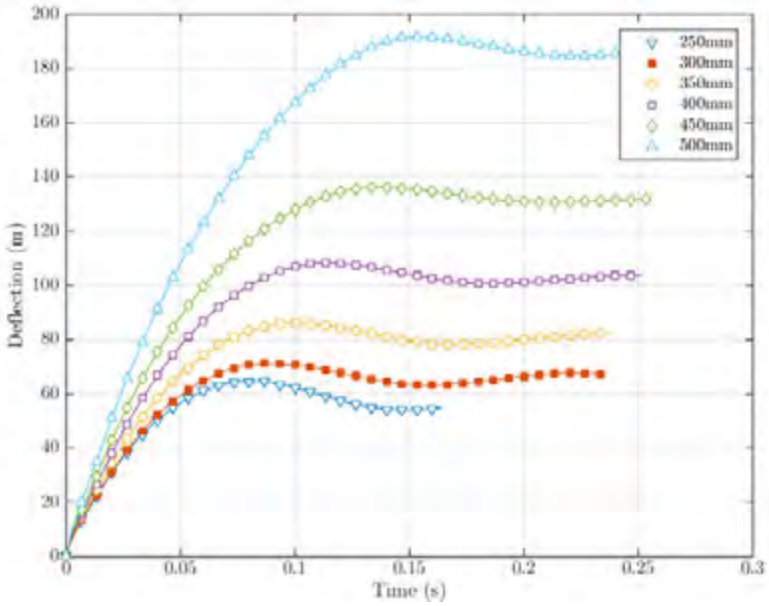

Figure 4.58: Transverse deflection time histories of a Ø43×2.3 mm round tube struck at approximately one third of the length from the fixed pivot with a mass of 200 kg at different drop heights.

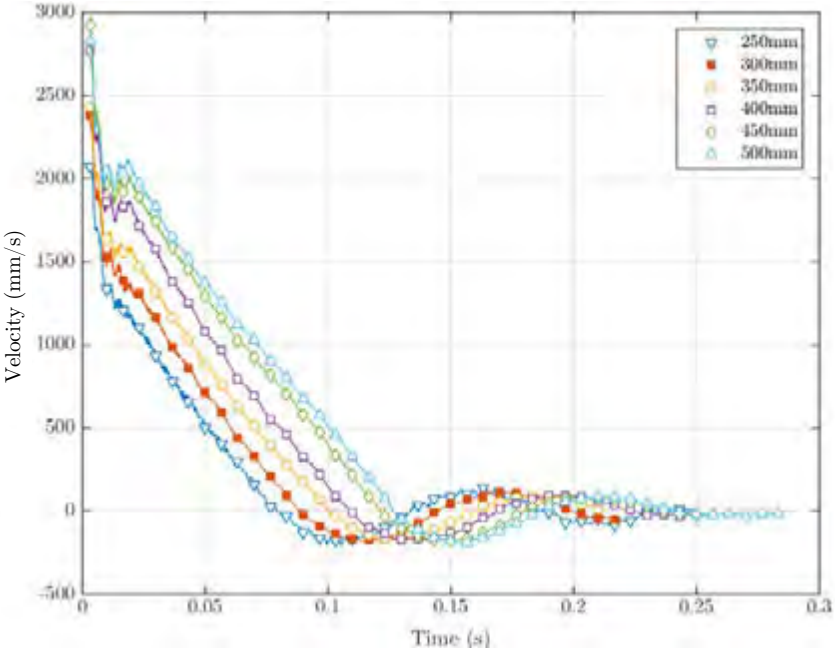

Figure 4.59: Striker velocity time histories of a 40×2.0 mm square tube struck at approximately one third of the length from the fixed pivot with a mass of 200 kg at different drop heights.

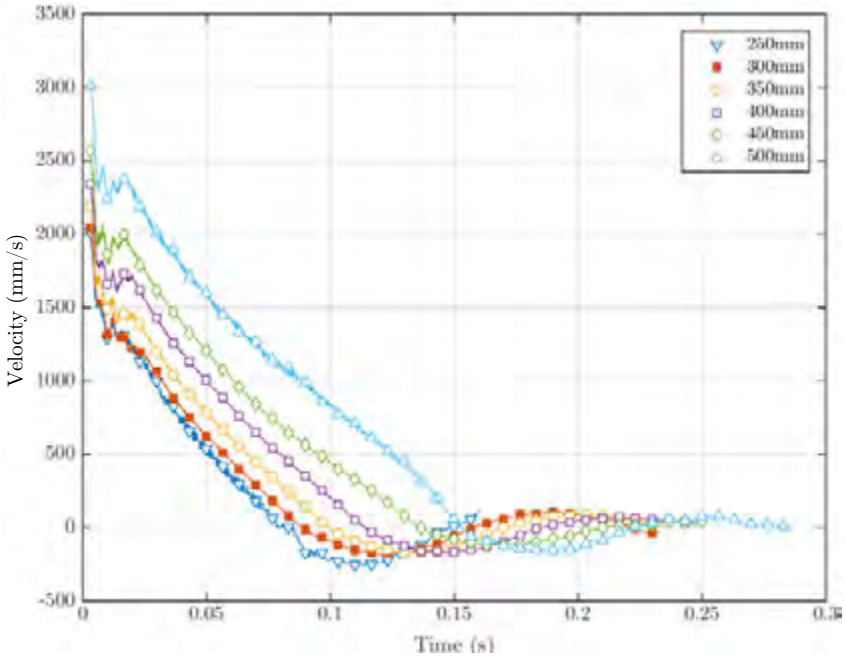

Figure 4.60: Striker velocity time histories of a Ø43×2.3 mm round tube struck at approximately one third of the length from the fixed pivot with a mass of 200 kg at different drop heights.

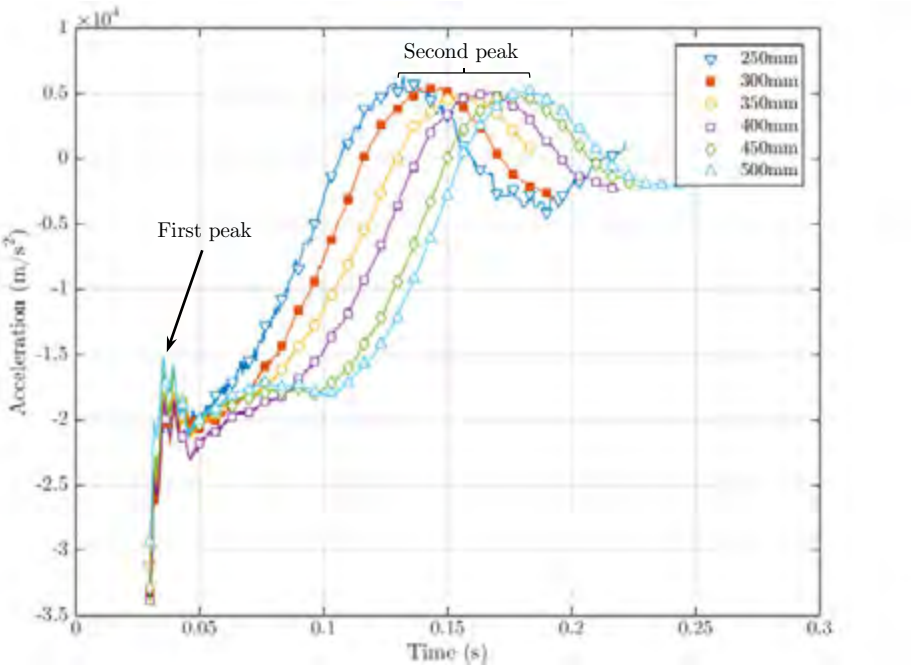

Figure 4.61: Striker acceleration time histories of a 40×2.0 mm square tube struck at approximately one third of the length from the fixed pivot with a mass of 200 kg at different drop heights.

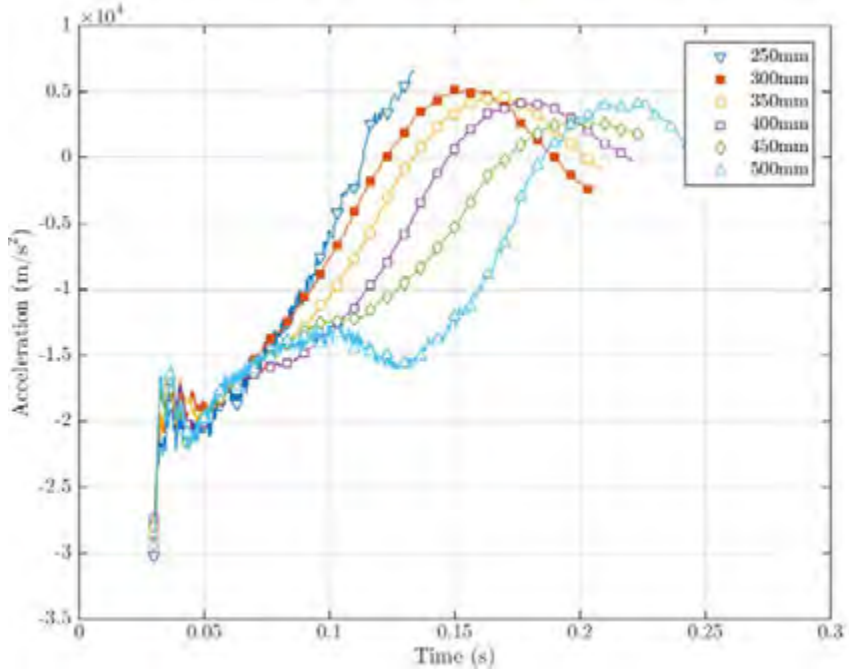

Figure 4.62: Striker acceleration time histories of a Ø43×2.3 mm round tube struck at approximately one third of the length from the fixed pivot with a mass of 200 kg at different drop heights.

4.4.6 Numerical Results of Beam Drop Tests

The impact tests of the square and round tubes were simulated, with results shown in Table 4.13. The average acceleration was calculated as the equivalent constant acceleration that would stop the striker in the same amount of time as it did in the impact.

Table 4.13: Unprocessed data from the numerical results for the square and round tubes.

	Drop Height (mm)	Encum-brance (mm)	Max Deflection		Energy Absorbed (J)	Impact Velocity (m/s)
			Time (sec)	Qty (mm)		
□	250	21.5	0.072	66.4	438.0	1.830
	300	29.6	0.09	88.1	559.0	2.097
	350	36.2	0.098	103.0	632.5	2.249
	400	50.9	0.108	134.0	773.0	2.574
	450	55.7	0.105	143.0	815.0	2.684
	500	57.2	0.105	145.0	829.0	2.721
○	250	23.9	0.079	71.6	489.0	1.913
	300	25.3	0.085	79.5	509.0	1.932
	350	30.3	0.092	93.3	609.0	2.139
	400	39.6	0.108	116.0	728.0	2.354
	450	52.3	0.121	140.0	835.0	2.542
	500	80.3	0.127	182.0	930.0	2.728

The maximum force is calculated from the maximum acceleration and the mass of the striker from the numerical results. The average force is calculated from the average acceleration and striker mass. The SEA, CFE and SPI were computed from the encumbrance, maximum deflection, and energy absorbed. Equations for CFE, SEA and SPI are restated from Chapter 2 (Equations 2.2, 2.3 and 2.4) in Equations 4.8, 4.9, and 4.10 respectively.

$$CFE = {P_{avg}(\delta L_{max})}\Big/{P_{max}(\delta L_{max})} \tag{4.8}$$

$$SEA = \frac{U_e}{Mass} \tag{4.9}$$

$$SPI = \frac{SEA(\delta L_{max}) \cdot \eta(\delta L_{max})}{W \cdot \delta L_{max}} \tag{4.10}$$

Table 4.14: Processed numerical results of drop tests of the square and round tubes as per experimental specification.

Geometry	Drop Height (mm)	Avg Acceleration (m/s^2)	Max Force (N)	Avg Force (N)	SEA (J/kg)	CFE (%)	SPI (kN/kg mm)
Square	250	25.4	4530.0	3814.3	158	84.20	0.093
	300	23.3	4575.0	3496.0	201	76.41	0.059
	350	23.0	5940.0	3443.8	228	57.98	0.035
	400	23.8	7380.0	3576.2	278	48.46	0.020
	450	25.6	7725.0	3834.4	293	49.64	0.018
	500	25.9	7815.0	3887.3	298	49.74	0.018
Round	250	24.2	5655.0	3632.4	172	64.23	0.065
	300	22.7	4695.0	3410.7	179	72.64	0.065
	350	23.3	5190.0	3488.2	214	67.21	0.051
	400	21.8	5175.0	3270.5	256	63.20	0.035
	450	21.0	4785.0	3151.3	294	65.86	0.026
	500	21.5	4590.0	3222.4	327	70.20	0.016

The average acceleration of the square tube drop tests was relatively constant across the range of drop heights, whereas the average acceleration of the round tube drop tests reduced with increasing drop height. The specific energy absorption for both square and round tube drop tests increased with drop height, which is expected as the mass of the tube remained constant across tests whilst the potential energy from the striker increased. The crash force efficiency for the square tube showed an inverse proportionality with drop height, as the CFE was highest at the lowest drop height. The SPI indicated that both square and round tubes performed best at the lowest drop heights. Some energy balance calculations based on potential and kinetic energies were conducted to validate the energy absorbed, and the results are compared with the experimental data in 4.4.7

4.4.7 Comparison of Experimental and Numerical Results

A topological optimisation was conducted using a linear polynomial metamodel with full factorial D-Optimal design point selection. A mean square error on the ordinate values of the deflection time histories of the experimental and numerical results were used as the objective function and optimised using the ASA optimisation algorithm.

The velocity at which the striker impacted the tube and contact friction between the striker and tube were optimised in LS-Opt. Three series of simulations using a coefficient of friction of 0.30, 0.50 and 0.74 were run. The lower most, and upper most friction coefficients were chosen based on the study by Ramsdale [92], and the friction coefficient of 0.50 referred to the LS-Opt averaged result.

The temporal deflection histories for each experiment of the square tubes were superimposed on the results from the numerical optimisation studies. The numerical result was plotted using the averaged coefficient of friction of 0.50 with error bars indicating the variation in the numerical result due to changing the friction coefficient to 0.30 or 0.74.

The results showed good correlation for the different drop heights with different levels of variation between tests, with some over predicting and some under predicting. The square tube test results from a drop height of 250 mm, plotted in Figure 4.64 showed the best correlation. Tests from drop heights of 300 mm and 400 mm, plotted in Figures 4.65 and 4.67 respectively showed a marginal over prediction. The drop test from a 350 mm height marginally under predicted the deflection time history as indicated in Figure 4.66 and a marginal mismatch in the period of the deflection time histories of the drop tests from heights of 450 mm and 500 mm as illustrated in Figures 4.68 and 4.69 respectively. The experimental deflection time histories of the square tubes are plotted in Figure 4.70, along with the numerical deflection time histories with error bars due to friction of all the drop tests.

It was possible to further improve the correlation of the deflection time histories between the numerical simulations and experimental results. This was achieved by varying the friction coefficient within the range of 0.3-0.74. This gave a good indication of role that friction played in the deflection of the tubes during impact. Furthermore, visual inspection of the tubes and striker after the experimental tests revealed scratching of the paint and steel on both surfaces, with scratching appearing more severe in the higher drop tests as shown in Figure 4.63. Therefore friction had a larger effect on the outcome of the test for higher drop heights, which is visible in the numerical results in Figure 4.70 as the error bar defining the friction bound became larger with increasing drop heights.

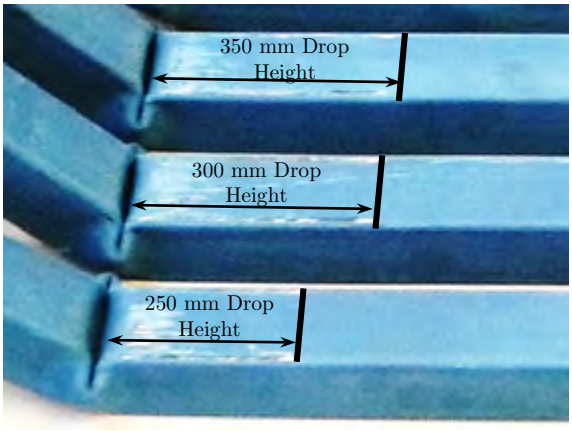

Figure 4.63: Increase in visible scratching of square tubes with increasing drop heights.

The numerical and experimental displacement-time histories were differentiated for the drop test from a height of 250 mm to produce the velocity-time histories shown in Figure 4.71. The velocity was at its maximum magnitude of approximately 2 m/s immediately after contact was established between the striker and tube. The data for the velocity-time history of the experimental results fluctuated about the numerical results. This was amplified upon differentiation to produce the acceleration-time histories shown in Figure 4.72. The deceleration was fairly constant at 20 m/s^2 throughout the duration of impact.

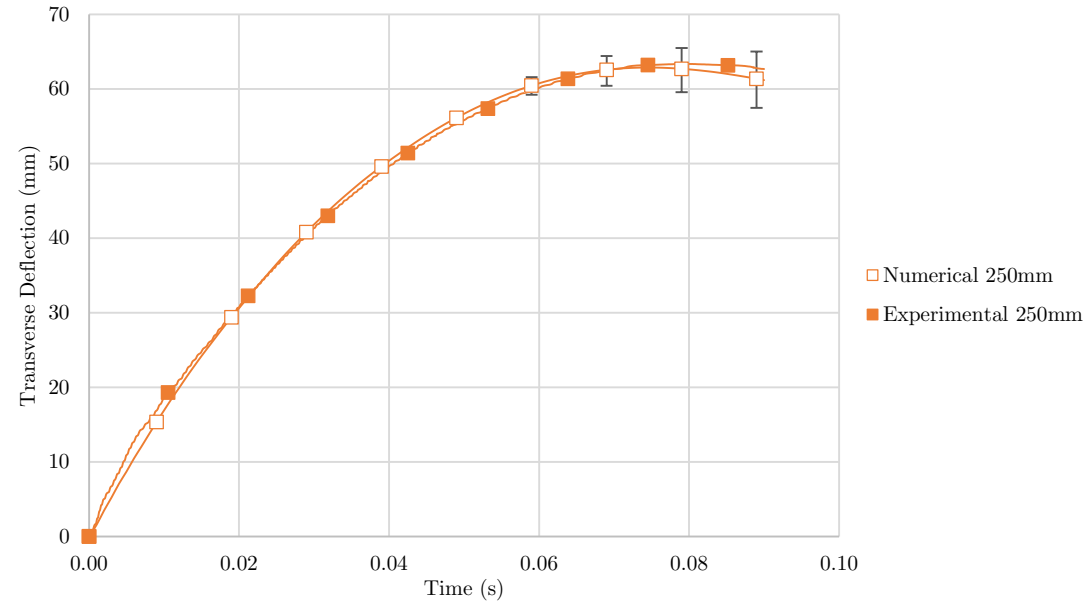

Figure 4.64: Numerical versus experimental temporal deflection histories of square tube drop test from a height of 250 mm, with plotted friction coefficient of friction of 0.50 and error bar indicating the effect of changing the friction coefficient to 0.30 or 0.74.

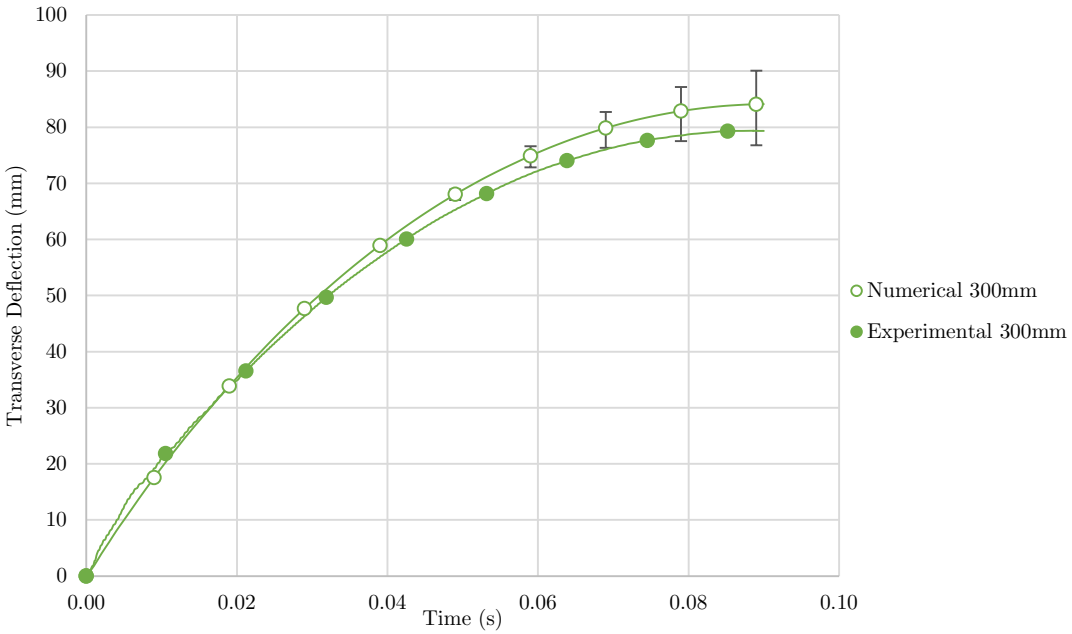

Figure 4.65: Numerical versus experimental temporal deflection histories of square tube drop test from a height of 300 mm, with plotted friction coefficient of friction of 0.50 and error bar indicating the effect of changing the friction coefficient to 0.30 or 0.74.

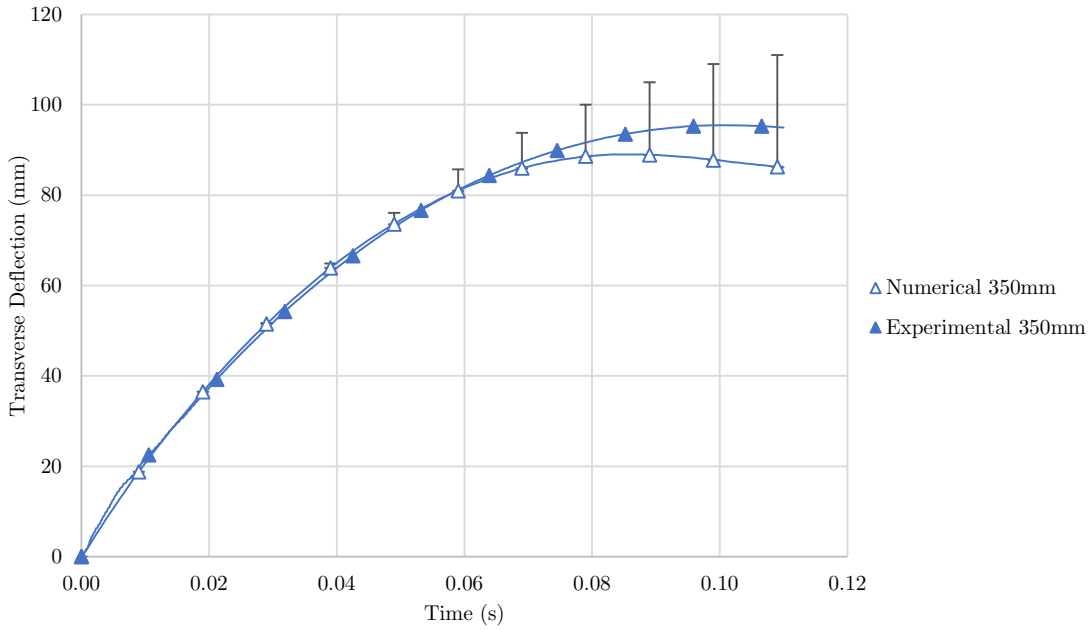

Figure 4.66: Numerical versus experimental temporal deflection histories of square tube drop test from a height of 350 mm, with plotted friction coefficient of friction of 0.50 and error bar indicating the effect of changing the friction coefficient to 0.30 or 0.74.

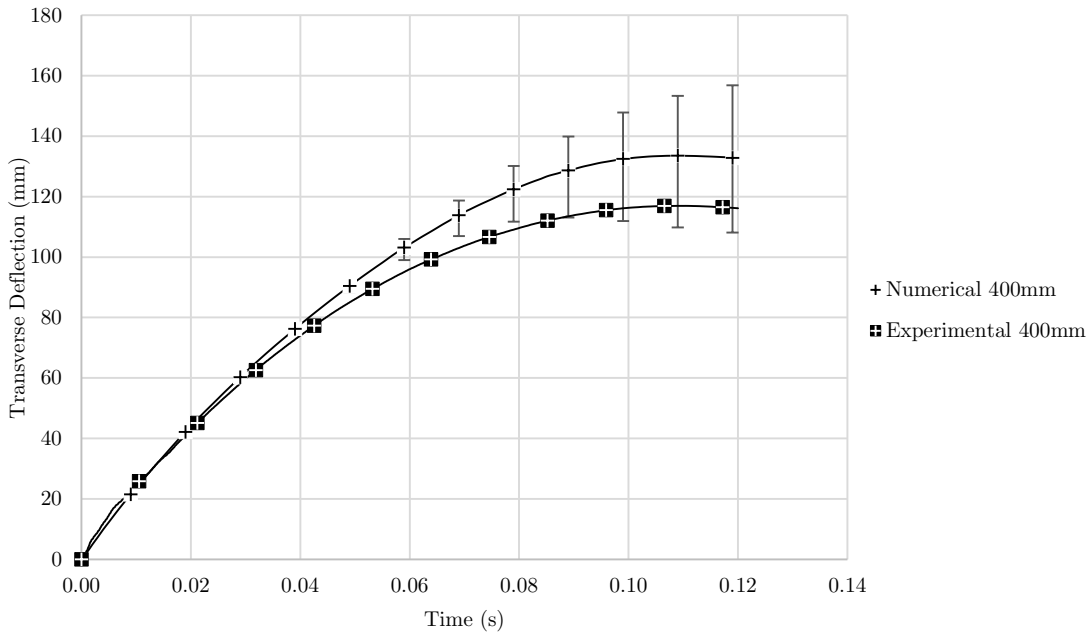

Figure 4.67: Numerical versus experimental temporal deflection histories of square tube drop test from a height of 400 mm, with plotted friction coefficient of friction of 0.50 and error bar indicating the effect of changing the friction coefficient to 0.30 or 0.74.

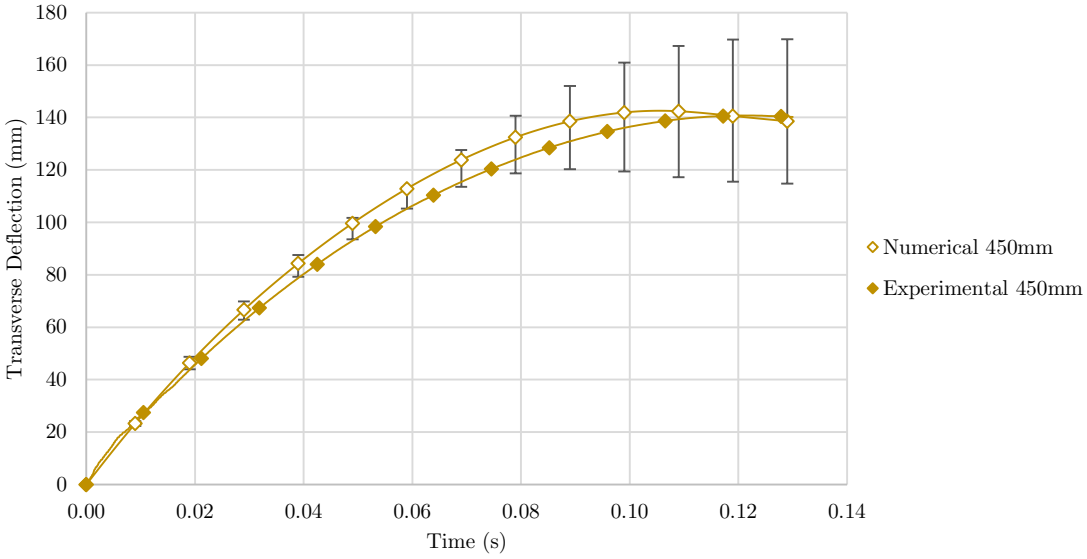

Figure 4.68: Numerical versus experimental temporal deflection histories of square tube drop test from a height of 450 mm, with plotted friction coefficient of friction of 0.50 and error bar indicating the effect of changing the friction coefficient to 0.30 or 0.74.

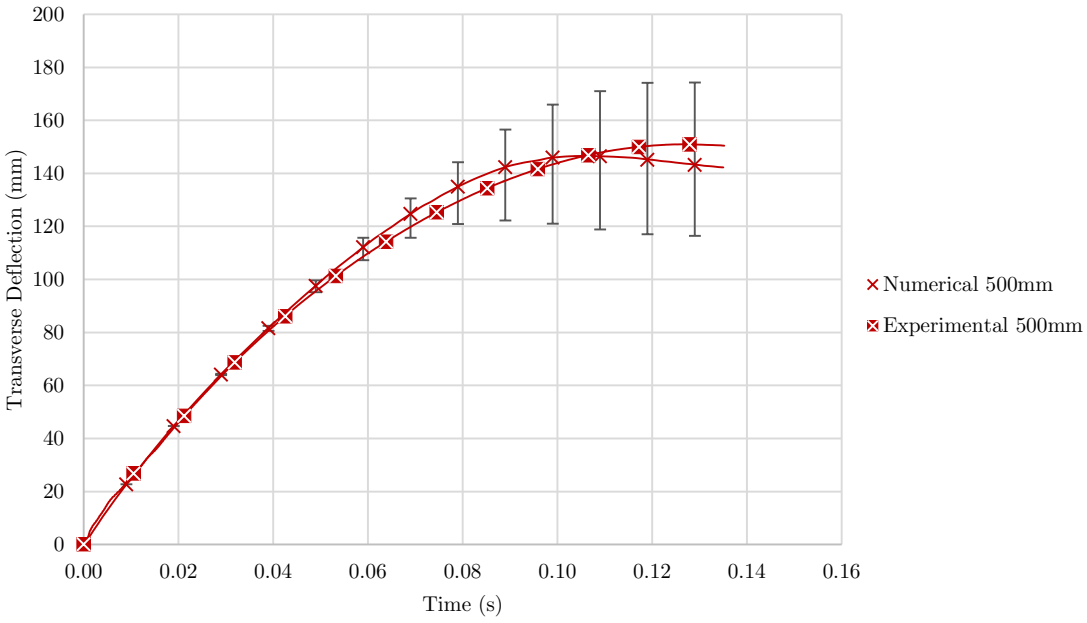

Figure 4.69: Numerical versus experimental temporal deflection histories of square tube drop test from a height of 500 mm, with plotted friction coefficient of friction of 0.50 and error bar indicating the effect of changing the friction coefficient to 0.30 or 0.74.

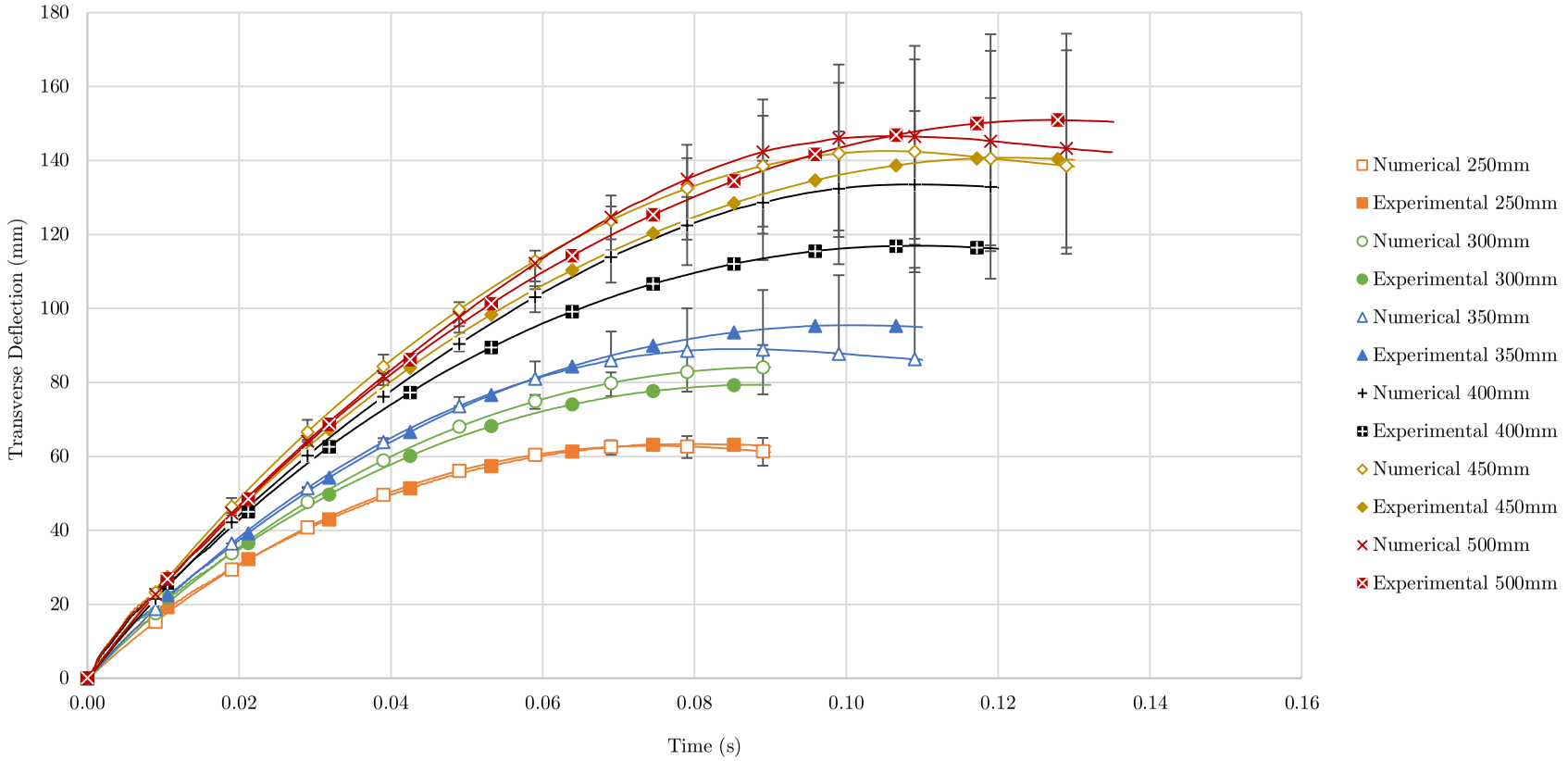

Figure 4.70: Numerical and experimental temporal deflection histories of square tube drop test from heights of 250 mm, 300 mm, 350 mm, 400 mm, 450 mm, and 500 mm, with plotted friction coefficient of friction of 0.50 for the numerical result and error bar indicating the effect of changing the friction coefficient to 0.30 or 0.74.

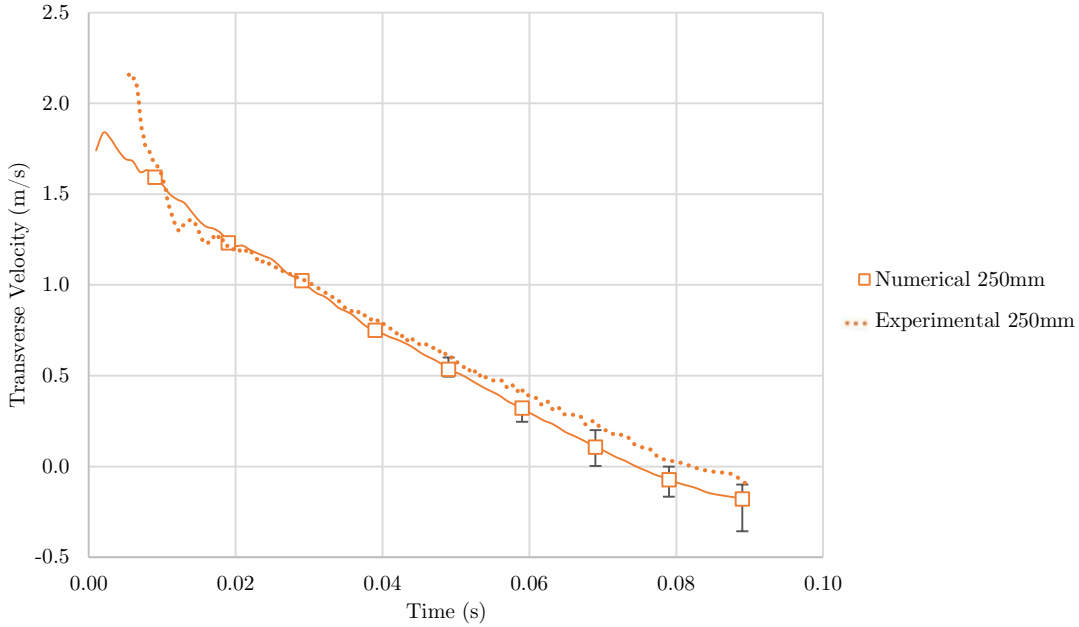

Figure 4.71: Numerical versus experimental temporal velocity histories of square tube drop test from a height of 250 mm, with plotted friction coefficient of friction of 0.50 and error bar indicating the effect of changing the friction coefficient to 0.30 or 0.74.

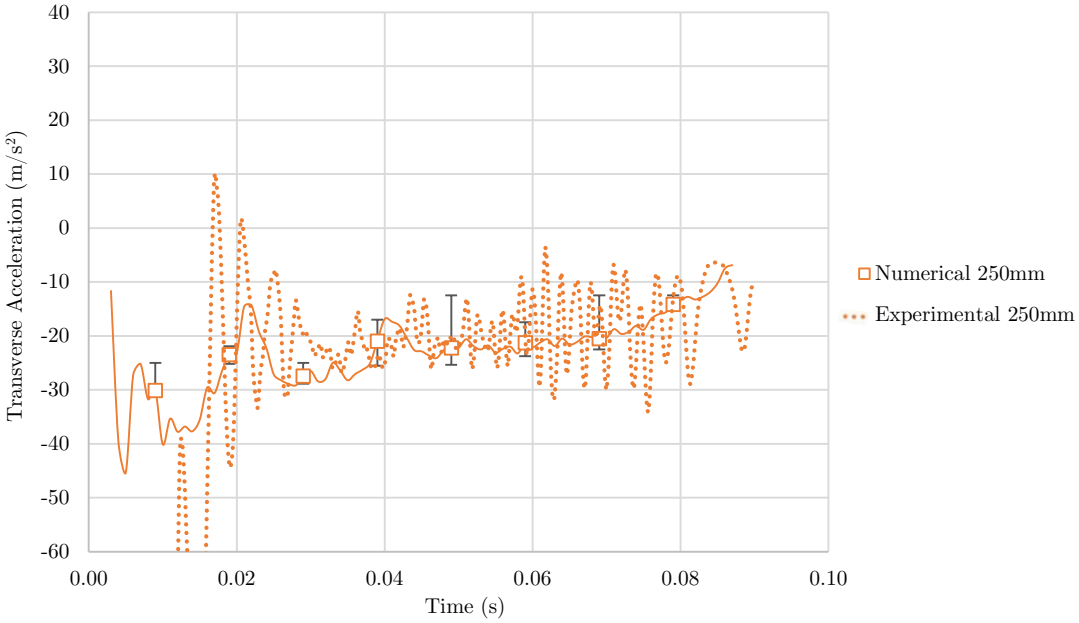

Figure 4.72: Numerical versus experimental temporal acceleration histories of square tube drop test from a height of 250 mm, with plotted friction coefficient of friction of 0.50 and error bar indicating the effect of changing the friction coefficient to 0.30 or 0.74.

4.4.8 Experimental Study of Effect of Seam Weld on Square Tubes

The effect of weld position on the square tube was studied as there were additionally available square tubes for testing. A total of three different positions, as shown in Figure 4.73 were experimentally tested to determine the effect on the resulting deflection. The three weld seam positions considered were on the lower face, side face with the weld toward the bottom, and top face. The striker impacted the tubes on the top face in all cases. In the case where results showed a significant deviation, repeated tests indicated by "Lower Side 2", and "Lower Side 3" were carried out. A photograph of all the square tubes placed side-by-side is shown in Figure 4.74.

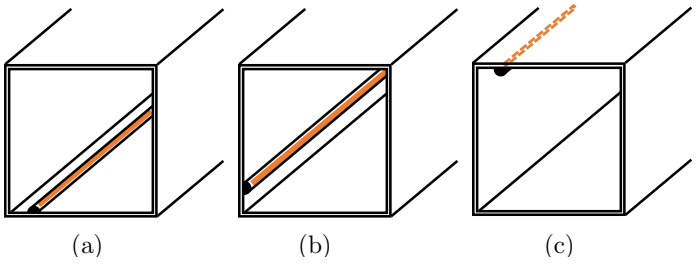

Figure 4.73: Seam weld positions, (a) weld seam on "Bottom", (b) weld seam on "Lower Side", (c) and weld seam on "Top".

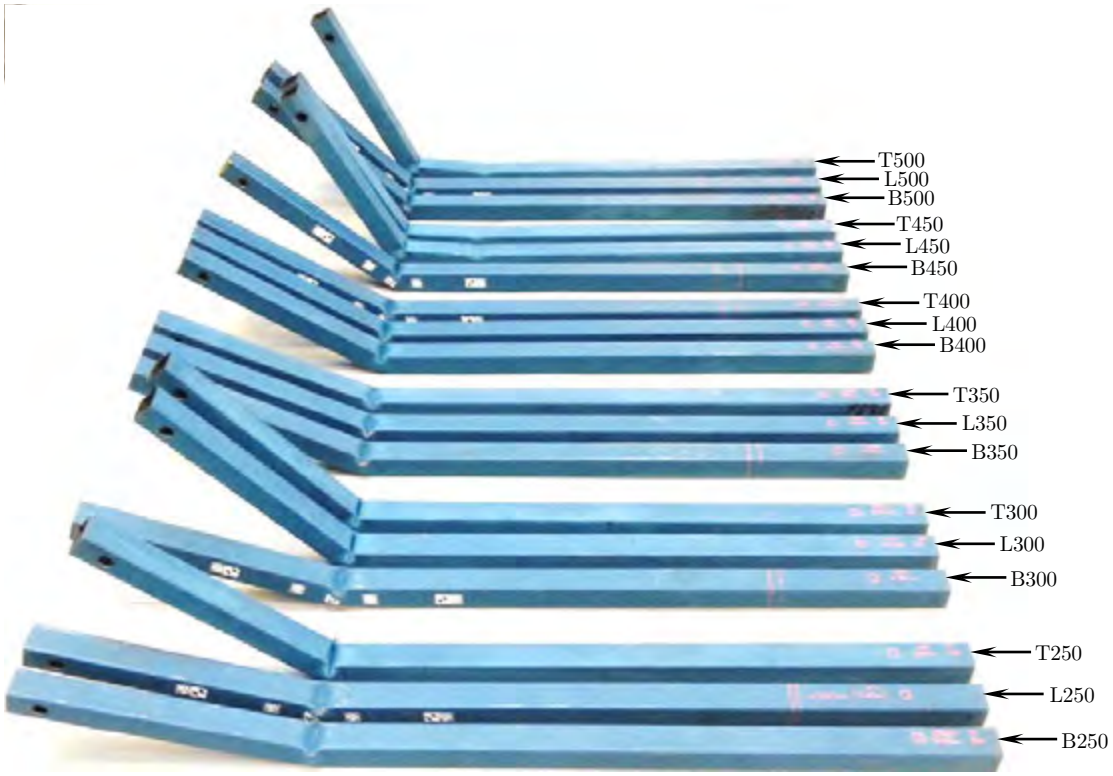

Figure 4.74: 40×2.0 mm Square tube drop test results with weld seam orientation altered with incrementally varying drop heights from 250-500 mm.

Each test was designated with one alphanumeric followed by a three digit number. The number refers to the height from which the striker was dropped in millimetres and a descriptor for the alphanumeric preceding the number is given for each as follows:

- T - Weld seam located on the struck face (I.e. on top),
- L - Weld seam located on the lower third of one of the two side faces (I.e. lower side), and
- B - Weld seam located on the bottom face toward one side (I.e. bottom face).

It was unclear as to why some tubes buckled more severely than the majority of tests, such as T250, T300, L300, T450, L450, T500 and L500. A further four tests were conducted, one T250, L300, and L450, as well as two L500's to investigate the more severe deformation. The results including the additional four tests are illustrated in the bar chart in Figure 4.75.

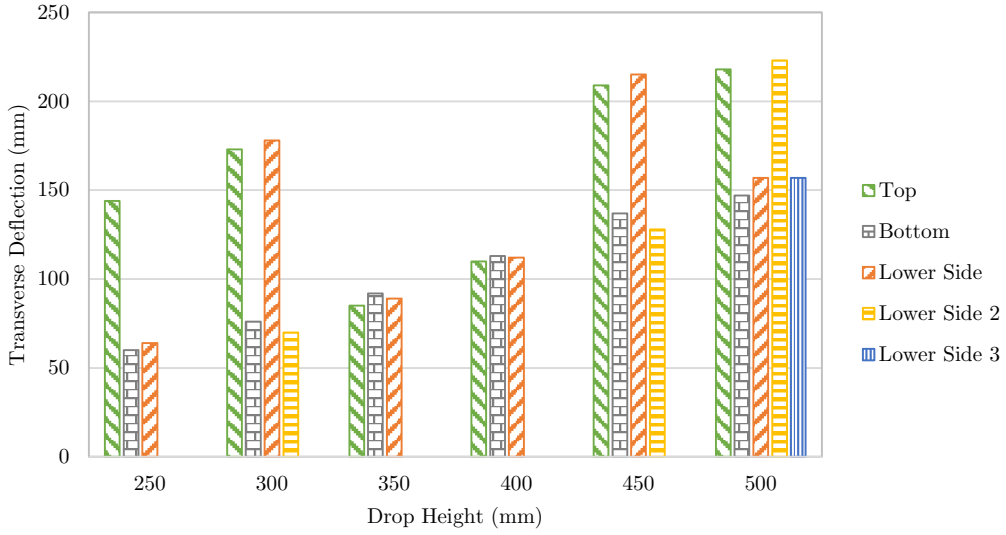

Figure 4.75: Effect of weld Seam position of deflection of Square 40×2.0 mm Steel Tube subjected to lateral impact of a 200 kg mass from different drop heights.

The results showed a total of seven higher than usual deformations, of which the weld seam was in the top position in four tests, and three when the weld was at the lower side. The seven tubes exhibiting higher deflection than the rest were separated from the batch and two separate plots were created. One plot for the remaining tube deflections, given in Figure 4.76(a), and another plot for the early buckling tubes, given in Figure 4.76(b). The deflections of the tubes which did not buckle early (Figure 4.76(a)) correlated best with the numerical deflections obtained. The early buckling tubes were not analysed further under the scope of this study.

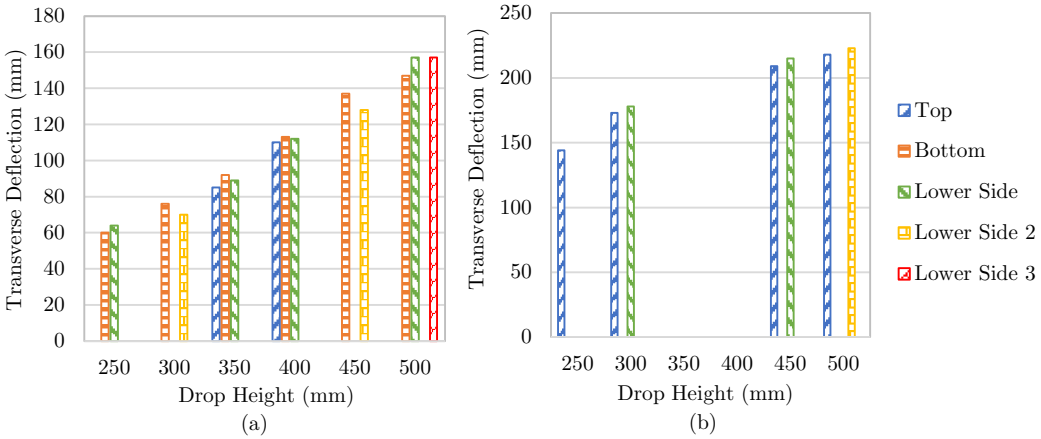

Figure 4.76: Effect of weld seam position of deflection of square 40×2.0 mm steel tube subjected to lateral impact of a 200 kg mass from different drop heights, (a) late buckling tubes, and (b) early buckling tubes.

The bar chart illustrated in Figure 4.76(a) shows that for a given drop height the weld seam increased the tubes resistance to deflection when at the top (on the struck face) by approximately 8% for the 350 mm drop height and 3% for the 400 mm drop height. However, repeatability tests for same drop height and weld position in each case was not carried out. As a result, it is not possible to make conclusive remarks as to the repeatability of a given test configuration. The local deformation on the top surface was highest, and the bottom surface was the lowest. This indicated that the weld seam served to increase the resistance to deformation in the region in which the seam presided, possibly due to the HAZ, although further testing would need to be carried out to confirm this. The experimental results are also listed in Table 4.15.

Table 4.15: Effect of weld seam position of deflection of square 40×2.0 mm steel tube subjected to lateral impact of a 200 kg mass from different drop heights.

Square Tube		
Drop Height (mm)	**Weld Seam Position**	**Deflection (mm)**
250	Top	0
	Lower Side	64
	Bottom	60
300	Top	0
	Lower Side 1	0
	Lower Side 2	70
	Bottom	76
350	Top	85
	Lower Side	89
	Bottom	92
400	Top	110
	Lower Side	112
	Bottom	113
450	Top	0
	Lower Side 1	0
	Lower Side 2	128
	Bottom	137
500	Top	0
	Lower Side 1	0
	Lower Side 2	223
	Lower Side 3	157
	Bottom	147

4.5 Summary of Numerical and Experimental Results

An FE model of a passenger sedan developed by the NCAC was used to investigate the transient behaviour of a side door during impact with a 10 inch rigid vertical pole from the side at 29 km/h. The contact point of the pole was 1046 mm longitudinally from the front left axle. The door was observed to deform into a distinct V-shape as it wrapped around the pole. The side impact beam was found to absorb 2.76 kJ of the total 33.1 kJ. The bulk of the impact energy (66%) was dissipated via bending of the floor, roof and door panels.

The model of the car door was validated by means of experiments. A test rig was designed to reproduce the deformation profile and transient response of the car door from the full vehicle simulation. A striker of mass 385 kg, dropped from a height of 1.274 m, was found to best reproduce the behaviour of the door from the full vehicle simulation. The car door model was validated with observed deflections in both the experiment and simulation of approximately 208 mm after 0.08 seconds.

The side impact beams used in the optimisation study were characterised by means for SEM and quasi-static lateral compression tests. The SEM results revealed that the materials of both the square and round tube were predominantly ferrous, with trace quantities of manganese and chromium. It was thus assumed that both geometries were made from a manganese alloying steel, with Young's Modulus of 200 GPa. The lateral compression tests on the square and round tube material yielded 335 MPa and 472 MPa for the strength coefficient, and a hardening exponent of 0.065 and 0.078, respectively.

The square and round tubes were used to validate the side impact beam model by means of drop test experiments. Rate effects were accounted for by means of the Cowper-Symmonds formulation, with parameters obtained from the literature [72]. The experimental validation was carried out by dropping a 200 kg mass from six different heights at increments of 50 mm between 250-500 mm. The effect of friction was investigated by varying the friction coefficient between 0.3-0.74. A coefficient of friction of 0.5 was found to best reproduce the transverse deflections observed in the experiments.

Chapter 5

Parametric Study

This chapter reports on the numerical simulations carried out to determine the effect of parameters not studied experimentally, such as the inner tube length on the SEA and total transverse deflection. The objectives were to investigate the SEA and deflection characteristics resulting from different side impact beam configurations.

5.1 Different tube thicknesses and materials

The original side impact beam was made from a steel alloy. An alternative in the form of aluminium was investigated as part of this parametric study, as it has a lower density thus allowing for a larger volume of material to be used for the equivalent mass of steel. The mean diameter of the round tube and mean width of the square tube for both steel and aluminium alternatives were kept constant whilst the thickness was varied.

Three materials, namely 6061-T6 Aluminium, unnamed square tube material, and unnamed round tube material were selected to study their effect on SEA and maximum deflection. The materials were applied to the square and round side impact beam models. The tube thickness was the only parameter varied for each of the two configurations. Material data for aluminium was obtained from Jones [32] and Roeder [95].

LS-DYNA finite element shells are defined at mean thickness. The original square and round tubes had dimensions 40.0×2.0 mm and Ø43.0×2.3 mm respectively. This corresponds to a mean width

and diameter of 38.0 mm and Ø40.7mm respectively. Therefore thickness variation in this study was extended evenly outward from the mean cross-section dimensions.

The results for deflection versus tube thickness for the square and round tube profiles are shown in Figure 5.1. The results showed that an increase in tube thickness correlated to a reduction in deflection and for all configurations (square and round, as well as aluminium and steel) the deflection tended asymptotically toward zero with increasing thickness, which may not necessarily have been the case if tearing were included in the model.

The results showed that aluminium performed worse for both round and square tube configurations when compared to their steel counterparts for the same tube thickness. This was expected as aluminium had lower strength properties and mass than steel for the same volume. When compared by means of the specific energy absorption metric as shown in Figure 5.2, however, the aluminium performed better than the steel due to its lower density.

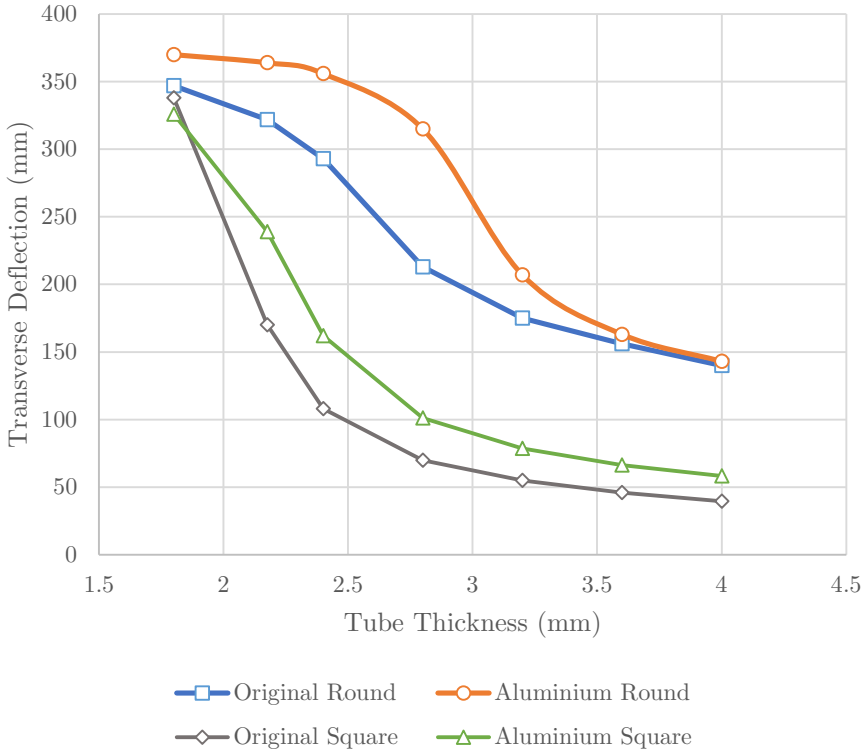

Figure 5.1: Transverse deflection versus tube thickness for the 40.7 mm mean diameter round tube and 38 mm mean width square tube.

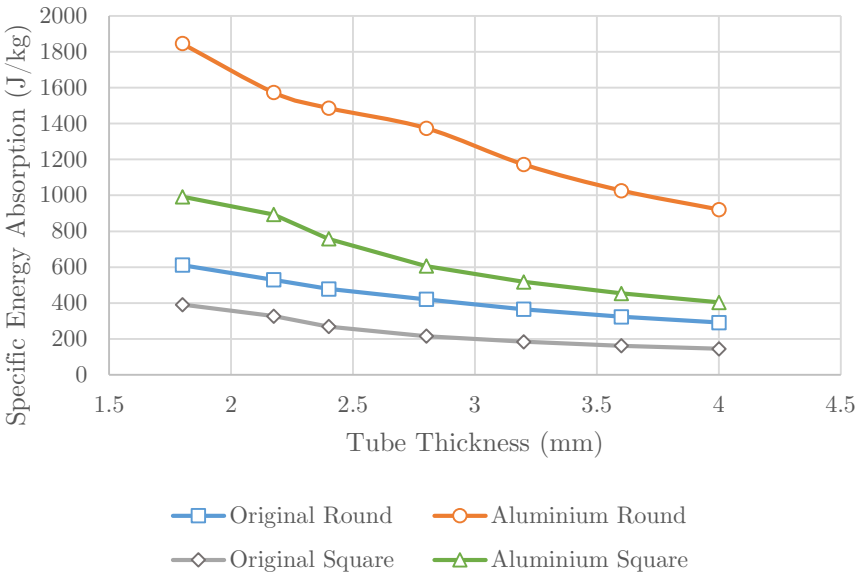

Figure 5.2: Specific energy absorption versus tube thickness for the 40.7 mm mean diameter round tube and 38 mm mean width square tube.

A comparison between the SEA to deflection of aluminium and steel tubes, illustrated in Figure 5.3, shows that the aluminium absorbed two or more times the energy per unit mass for the same transverse deflection. This is a significant improvement over the original material of the square and round tubes. However, thicker materials are more prone to tearing as opposed to deformation [96, 97], which was not considered in this study.

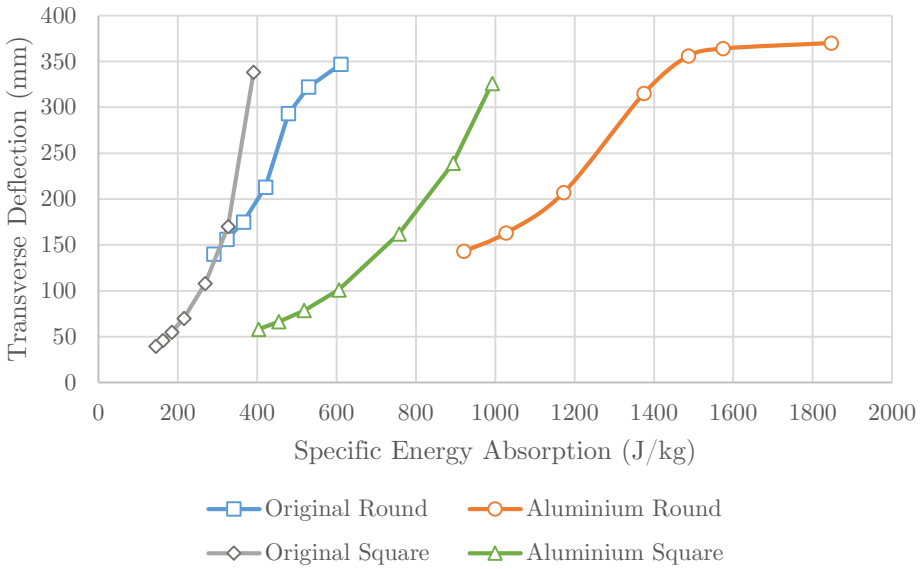

Figure 5.3: Transverse deflection versus specific energy absorption for the 40.7 mm mean diameter round tube and 38 mm mean width square tube.

As with any engineering project the economics and business incentive has an intimate coupling with the feasibility of the design. Aluminium performs better than steel, however, the cost of raw material is higher. The price of aluminium was approximately four times that of steel [98] as of the last quarter of 2015. However, despite the initial capital outlay the running and maintenance cost of aluminium is lower than steel as it is lighter and does not corrode as easily in most climates. Aluminium does however react with steel when in contact, which needs to be taken into consideration when using aluminium side impact beams in steel doors.

5.2 Inner tube length and outer tube thickness coupling of a compound tube

In this configuration an inner tube was inserted into an outer tube. The effect of the length of an inner tube in a compound tube configuration was studied. The mass of the compound tube configuration was kept constant and equal to that of the original single side impact beam. This was achieved by controlling the thickness of the outer tube with constant length such that with increasing length of the inner tube, which had constant thickness, there was a proportional reduction in thickness of the outer tube. The shortest length was dictated by the minimum span of the inner tube to extend beyond the line of action of the striker, and maximum length dictated approximately by the constant length outer tube. This corresponded to an outer tube thickness of between 2.0-0.5 mm respectively, and a constant inner tube thickness of 2mm. An illustration of the cross-sectional view of the inner and outer tube setup in the configuration that would emulate that of the side impact beam in the full vehicle model, is shown in Figure 5.4.

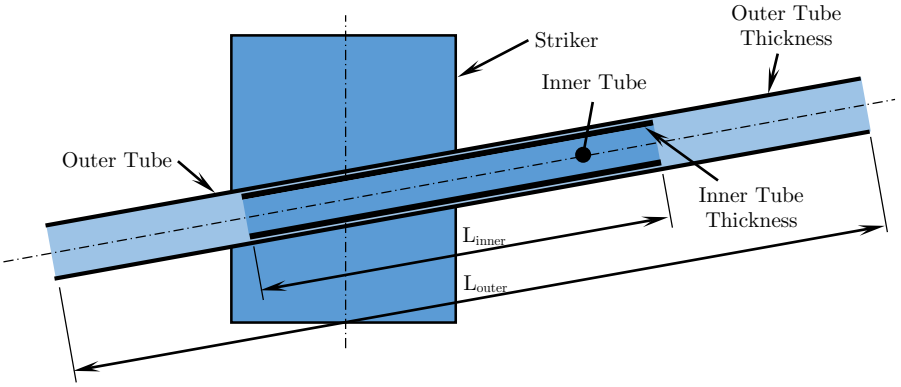

Figure 5.4: Illustration of compound tube configuration where inner tube has variable length and outer tube has variable thickness.

The inner tube mesh was contained within a morphing box with the relationship between the outer tube thickness and inner tube length controlled by a user defined function within the finite element pre-processor ANSA to maintain constant mass. The longitudinal centres of the inner and outer tubes coincided regardless of the length of the inner tube. Contact between the two tubes was by means of a light press fit to eliminate any slippage during the service life of the vehicle. Static and

dynamic contact friction between two steel components was assumed to be 0.74 and 0.57 respectively [92]. The same material parameters were used from the characterised round tube material. The mass of the compound tube was 1.51 kg and the length of the inner tube range was 143-895 mm.

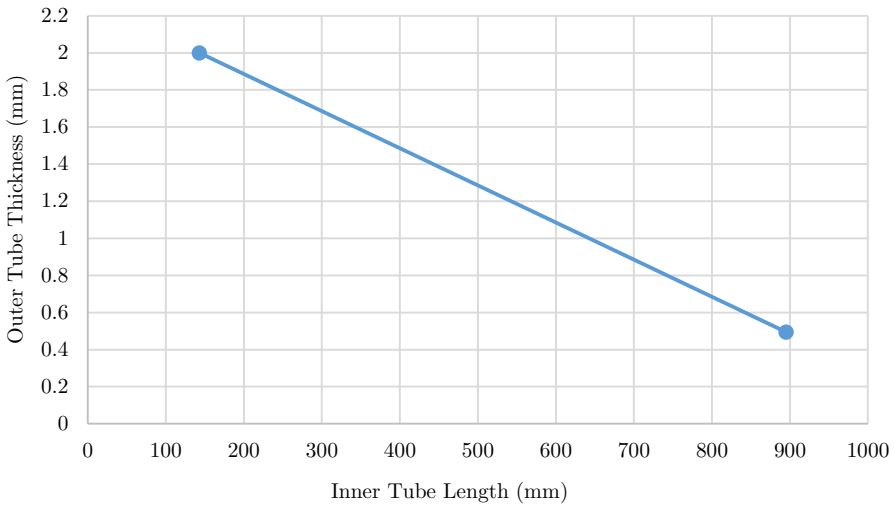

Figure 5.5: Relationship between inner tube length and outer tube thickness so as to maintain a constant mass.

The relationship between the inner tube length and outer tube thickness is shown in Figure 5.5. A mathematical representation of the relationship between the inner tube length and outer tube thickness so as to maintain a constant compound tube mass is given in Equation 5.1.

$$l_{inner\ tube} = 510 + 385 \times \frac{1.265 - t_{outer\ tube}}{0.77} \tag{5.1}$$

The graphic in Figure 5.6 shows the effect of varying the inner tube length and outer tube thickness so as to maintain a mass for the compound member. The configuration in Figure 5.6(a) performed the worst with a deflection of 323 mm, due to tube material being spread evenly throughout the length of the compound tube. In contrast, the inner tube length of the configuration in Figure 5.6(d) did not extend past the buckling point over the line of action of the striker resulting in the configuration performing poorly as well. The configuration that performed best is shown in Figure 5.6(b).

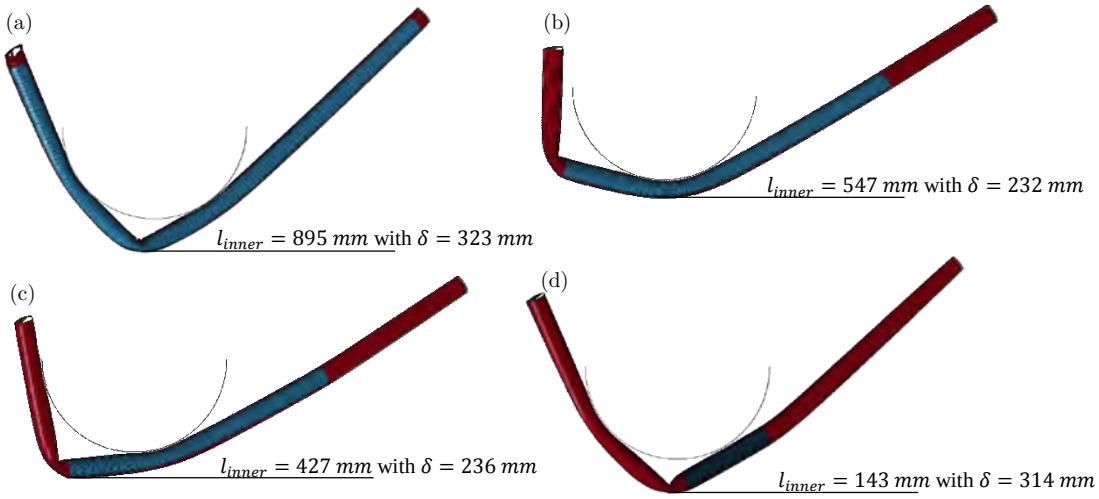

Figure 5.6: Effect of varying inner tube length with outer tube thickness.

Deflections were comparably high when the inner tube did not extend over the buckling point or when the inner tube was between 700-900 mm in length as this reduced the amount of material available to absorb energy in the region of buckling. Furthermore, buckling was observed in two separate locations when the inner tube length extended through the range of 700-800 mm. The relationship between inner tube length and transverse deflection is shown in Figure 5.7.

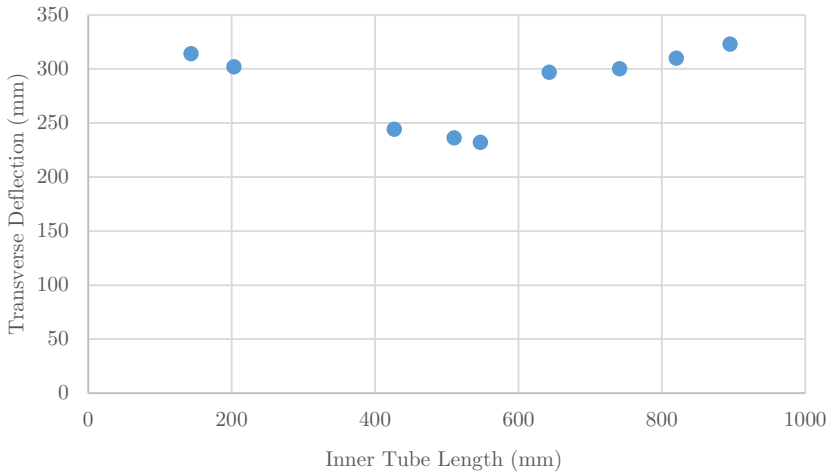

Figure 5.7: Deflection versus inner tube length for the compound tube configuration.

Both extremities of the inner tube length range of the compound member did not perform well. The best tube configuration deflected by 232 mm which was an improvement of approximately 39% over the worst configuration. The driving factor behind the optimal inner tube length was largely affected by the position of the striking body.

Table 5.1: Processed numerical results of compound tube parametric study.

Sim Num[4] (-)	Outer Tube Thickness (mm)	Inner Tube Length (mm)	Avg Acc (m/s^2)	Max Force (N)	Avg Force (N)	SEA (J/kg)	CFE (%)
1.2	0.50	895	34.9	13635	5230.9	624.5	38.4
1.3	0.65	820	34.9	11820	5230.9	603.3	44.3
2.2	0.80	741	34.6	10995	5183.8	588.1	47.2
4.2	1.00	643	33.4	10155	5003.5	621.9	49.3
19.1	1.19	547	38.7	10395	5812.1	628.5	55.9
1.1	1.27	510	40.0	11550	5993.8	627.8	51.9
4.4	1.43	427	44.6	19050	6690.7	557.0	35.1
2.3	1.88	203	37.6	15600	5641.2	631.1	36.2
1.4	2.00	143	36.5	14115	5480.0	633.1	38.8

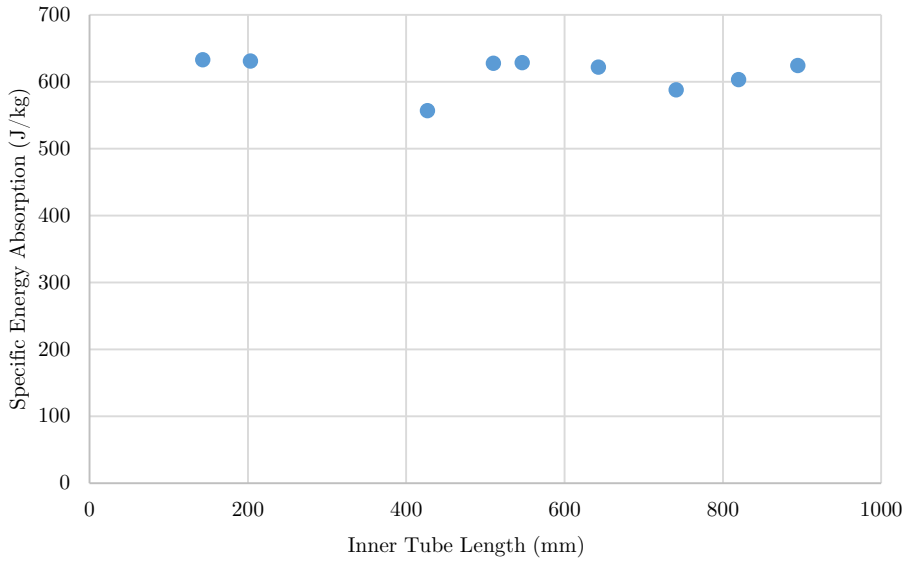

Figure 5.8: Specific energy absorption versus inner tube length for the compound tube side impact beam.

The best compound tube configuration was inserted into the full vehicle model and rerun. The rigid pole was found to intrude by 412 mm with the optimised configuration as compared with 413 mm for the original setup. The tube was also removed entirely from the model to investigate the behaviour of the vehicle without a side impact beam. This resulted in an intrusion of 438 mm. The results are listed in Table 5.2.

[4] Simulation number: The number preceding the point refers to iteration number, and the number after the point refers to the design case for a given iteration (four design cases per iteration)

Table 5.2: Result of optimised compound side impact beam configuration after insertion into full vehicle model.

Description	Deflection (mm)
Full vehicle model with original side impact beam	413
Full vehicle model with optimised compound side impact beam configuration	412
Full vehicle model without side impact beam	438

The original side impact beam in the full vehicle model absorbed approximately 8% of the total energy. As a result, a 10% improvement in the energy absorbing capability of the side impact beam correlates to a 0.8% improvement with respect to the full vehicle model. The compound tube mass during optimisation remained the same as that of the original side impact beam, which was an additional constraint against increasing the energy absorbing capability of the beam. As a result the overall improvement was only 1mm on the original full vehicle model.

5.3 Summary of Parametric Study

A parametric study of the drop test experiment was carried out on the square and round tube geometries to determine the effect of tube thickness on SEA, and overall deflection. Three materials were investigated, namely, 6061-T6 Aluminium, unnamed square tube material, and unnamed round tube material. The results showed that an increase in tube thickness correlated to a reduction in deflection, and for all configurations the deflection tended asymptotically toward zero with increasing thickness. The results showed that aluminium performed worse than steel for the same tube thickness. However, when compared using specific energy absorption the aluminium performed two or more times better than the steel due to its lower density.

In the second part of the parametric study the effect of the length of an inner tube in a compound tube configuration was studied. The mass of the compound tube configuration was kept constant at 1.51 kg (mass of the original side impact beam in the car door). The outer tube thickness was varied between 0.5-2.0 mm and inner tube length was varied between 143-895 mm. The best tube configuration corresponded to an inner tube length of 547 mm. This corresponded to a deflection of 232 mm which was an improvement of approximately 39% over the worst configuration. The best compound tube configuration was inserted into the full vehicle model and found to reduce the overall intrusion by 1 mm.

Chapter 6

Conclusions

The effect of different configurations on the performance of a side impact beam from a passenger sedan were investigated experimentally and numerically with a view to minimise intrusion into the passenger compartment. In this study a numerical model of a sedan was subjected to a side impact, in close conformation to the FMVSS 214 standard. The door was extracted from the full vehicle model and validated through experimentation, which was carried out in a vertical drop tester. A mass of 385 kg was dropped from a height of 1.274 m and found to cause a deflection of 253 mm at 0.088 seconds after impact.

The side impact beam was identified as the single largest energy absorbing component to side impact protection, absorbing over 8% of the total energy. The beam was numerically extracted from the door model for optimisation. A model was created to emulate the crash dynamics that the beam would experience in a side impact and was successfully validated by means of experiments. The validation process involved the characterisation of two beam materials using SEM, and a lateral tube compression test. Material parameters of a square and round tube were extracted through a numerical model which reproduced the lateral tube compression test conditions, which was used in the numerical side impact beam model. A strength coefficient of 335 MPa and hardening exponent of 0.065 was obtained from the quasi-static lateral compression tests for the square tube. Similarly, a strength coefficient and hardening exponent of 472 MPa and 0.078 was obtained for the round tube material, respectively. A numerical model of the side impact beam experimental test rig was used to study the effect of contact friction between the striker and tube. The friction appeared to affect the

mode of deformation. A high coefficient of friction resulted in flattening of the tubes whereas a low coefficient of friction resulted in a higher transverse deflection.

A parametric study was carried out on different tube configurations to determine the effect of length and thickness of a compound tube, material use, and tube profile on the performance in a lateral impact with reference to CFE and SEA.

The compound tube configuration in which the inner tube extended through the buckling point performed better provided that the inner tube did not extend near the full length of the outer tube. The result of the geometric optimisation of the side impact beam on the full vehicle model showed a 1 mm improvement over the singular tube configuration.

The tube thickness parametrisation study showed that thicker tubes of the same material were found to deflect less but have a lower SEA. Aluminium tubes absorbed more energy per unit mass than steel tubes. A round aluminium tube with a thickness of 2.175 mm was found to give the best balance between SEA and maximum deflection with magnitudes of 1.5 kJ/kg and 350 mm respectively. The square aluminium tube was the second highest performer in terms of its ability to absorb energy per unit mass with an optimal tube thickness of 1.8 mm. This resulted in an SEA and maximum deflection of approximately 0.99 kJ/kg and 326 mm respectively.

The model approach taken in this study proved successful in the optimisation of a side impact beam in a lateral collision of a passenger sedan. The simulation of the full vehicle model gave a good indication of the deformation and transient behaviour of the side impact beam. The approach to isolate different components can be beneficial in terms of cost savings from a computational perspective, provided that proper initial and boundary conditions are applied.

Chapter 7

Recommendations

This study served to provide better understanding of the mechanical response of the side impact protection measures in place in a typical passenger sedan, and how different parameters affect the behaviour of the system. Based on the findings and conclusions, some recommendations are made for further study.

- A damage model should be incorporated into the full vehicle model to capture brittle failure in components such as the windshield.
- The effect of residual stresses imparted on the door structure due to manufacturing should be investigated.
- More tests should be carried out in the region where the inner tube extends over the buckling point of the compound tube structure, as shown in Figure 5.7, to better capture the nonlinearity at the crossover.
- The degree of anisotropy in the tube material should be studied by means of grain structure analysis or cutting orthogonal specimens for testing.
- Variation of material properties across the batch of tubes should be investigated.
- The accelerations and forces in the tube and door experiments were calculated from the displacements measured for this thesis, accelerometers and load cells could be used instead to measure accelerations and forces independently of the displacements for future work.
- Meshes with nonuniform density should be generated to better capture buckling and reduce computational time. Where geometric morphing is used the morphing boxes should be strategically placed to retain a fine mesh density in the region where buckling occurs. In

cases where the region in which large strains occur are difficult to predict, it is recommended that adaptive meshing be used.

- The position of impact between the tube and striker was kept constant in this study, it is thus recommended that the effect of varying the striking position be investigated.
- There were seven special cases of square tube drop tests where the deflections were larger. It is recommended that repeatability tests be conducted for those configurations and further study be carried out to interpret this phenomenon.

References

[1] R. Nader, Unsafe at Any Speed, Detroit: Grossman Publishers, 1965.

[2] World Health Organisation, "Global Status Report on Road Safety," WHO, Geneva, 2015.

[3] WHO, "The top 10 causes of death," 03 September 2014. [Online]. Available: http://www.who.int/mediacentre/factsheets/fs310/en/index3.html. [Accessed 02 March 2015].

[4] I. Lau, J. Capp and J. Obermeyer, "A comparison of frontal and side impact: crash dynamics, countermeasures and subsystem tests," in *35th Stapp Car Crash Conference*, San Diego, California, 1991.

[5] O. D. Kuhnel, A. Suren, H. Weber, L. Gotzen, G. Schockenhoff and V. Vu Han, "Erhebungen am Unfallort," *Unfall und Sicherheitsforschung Strassenverkehr,* vol. 37, pp. 1-100, 1982.

[6] D. Otte, "Comparison and realism of crash simulation tests and real accident situations for biomechanical movements in car collisions," in *34th Stapp Car Crash Conference*, San Diego, California, 1990.

[7] D. Otte, "Deformation characteristics and occupant load capacity in lateral impacts for nearside belted front car passengers," in *37th Stapp Car Crash Conference*, San Antonio, TX, 1993.

[8] S. Rouhana and M. Foster, "Lateral impact - an analysis of the statistics in the NCSS," in *29th Stapp Car Crash Conference*, Washington, DC, 1985.

[9] E. Miltner, D. Kallieris, B. Wiedmann, B. Leutwein, H. Hepp, R. Fischer, H. Salwender and H. Frobenius, "About the threshold of fatal or potentially fatal injuries in car-to-car side collisions - a comparison between real accidents and PMHS-tests," in *35th Stapp Car Crash Conference*, San Diego, California, 1991.

[10] M. Danner and K. Langwieder, "Car/vehicle side impacts - a study of accident characteristics and occupant injuries," in *6th Int. Conference on Experimental Safety Vehicles*, Washington, DC, 1976.

[11] D. Otte, E. Suren, H. Appel and J. Nehmzow, "Vehicle parts causing injuries to front-seat car passengers in lateral impacts," in *28th Stapp Car Crash Conference*, Chicago. IL, 1984.

[12] D. Cesari, M. Ramet and C. Cavallero, "Influence of intrusion in side impact," in *6th Int. Conference on Experimental Safety Vehicle*, Washington, DC, 1976.

[13] K. Brohi, "Trauma.org," British Trauma Society, December 2006. [Online]. Available: http://www.trauma.org/archive/scores/ois.html. [Accessed 24 February 2015].

[14] Volvo Car Customer Service, "TJ Instruction VCC-376947-6," Volvo, Rockleigh, New Jersey 07647, 2013.

[15] NHTSA, "FMVSS NO. 214 Amending Side Impact Dynamic Test Adding Oblique Pole Test," U.S. Department Of Transportation, Washington, DC, 2007.

[16] Boron Extrication, "Hyundai Azera Side Impact Beams and Airbags," First Arriving Emergency Services Network, 16 September 2009. [Online]. Available: http://www.boronextrication.com/2009/09/16/hyundai-azera-side-impact-beams-and-airbags/. [Accessed 22 December 2015].

[17] F. Kressbach, "Body_Vision Door (Outside View with Anti-Intrusion Bar, Outer Skin Not Shown)," Meritor, 02 01 2010. [Online]. Available: http://www.meritor.com/Site%20Images/Forms/DispForm.aspx?ID=102&RootFolder=%2FSite%20Images%2F1Body. [Accessed 16 06 2015].

[18] US DOT, "About NHTSA," National Highway Traffic Safety Administration, [Online]. Available: http://www.nhtsa.gov/About. [Accessed 24 February 2015].

[19] Insurance Institute for Highway Safety, "IIHS HLDI," Highway Loss Data Institute, n.d.. [Online]. Available: www.iihs.org. [Accessed 06 January 2016].

[20] J. Ellway, M. van Ratingen, P. Goutas, P. Gay, T. Versmissen, S. von Montfort, A. Malak, T. Langner, J. Dobberstein, C. Denker, J. Hallack, K. Odanaka and T. Ogihara, "The advanced European Mobile Deformable Barrier Specification of use in Euro NCAP Side Impact Testing," in *Enhanced Safety of Vehicles*, Seoul, Republic of Korea, 2013.

[21] Euro NCAP, "How to Read the Stars," Euro NCAP, 2015. [Online]. Available: http://www.euroncap.com/en/about-euro-ncap/how-to-read-the-stars/. [Accessed 25 February 2015].

[22] R. R. Samaha, L. N. Molino and M. R. Maltese, "Comparative Performance Testing of Passenger Cars Relative to FMVSS 214 and the EU 96/EC/27 Side Impact Regulations: Phase I," National Highway Traffic Safety Administration, Washington, DC, 1998.

[23] ANCAP Australasia Ltd (ANCAP), "ANCAP Home," Involved, 2015. [Online]. Available: http://www.ancap.com.au/. [Accessed 25 February 2015].

[24] Latin NCAP Secretariat, "Latin NCAP Para Autos Mas Seguros," Latin NCAP, n.d.. [Online]. Available: http://www.latinncap.com/en/. [Accessed 25 February 2015].

[25] C-NCAP Information Media Ministry, "China New Car Assessment procedure (C-NCAP) Official Website," China Automotive Technology and Research Center, 2002. [Online]. Available: http://www.c-ncap.org/. [Accessed 25 February 2015].

[26] UNECE Transport Division, "Draft Global Technical Regulation for Pole Side Impact Tests," United Nations Economic Commision for Europe, Paris, 2012.

[27] N. Jones, Structural Impact, Second Edition, New York: Cambridge University Press, 2012.

[28] C. J. Opperman, "Study of a simplified bumper system subjected to offset impact loading," MSc Thesis, Department of Mechanical Engineering, University of Cape Town, Cape Town, 2012.

[29] A. Ghadianlou and S. B. Abdullah, "Crashworthiness design of vehicle side door beams under low-speed pole impacts," *Thin-Walled Structures,* vol. 67, pp. 25-33, 2013.

[30] M. Strano, A. Villa and V. Mussi, "Design and manufacturing of anti-intrusion bars made of aluminium foam filled tubes," *Int J Mater Form,* vol. 6, pp. 153-164, 2013.

[31] E. Hearn, Mechanics of Materials 1, Third Edition, Oxford: Butterworth Heinemann, 1997.

[32] G. Lu and T. Yu, Energy Absorption of Structures and Materials, Cambridge: Woodhead Publishing Limited, 2003.

[33] W. Johnson and A. Walton, "An experimental investigation of the energy dissipation of car bumpers under quasi-static lateral loads," *International Journal of Impact Engineering,* vol. 1, pp. 301-308, 1983.

[34] R. Hill, Mathematical Theory of Plasticity, Oxford: Oxford University Press, 1950.

[35] J. de Oliveira, T. Wierzbicki and W. Abramowicz, "Plastic behaviour of tubular members under lateral concentrated loading," *Nor. Veritas Tech. Rep,* Vols. 82-0708, 1982.

[36] T. Wierzbicki and M. Suh, "Indentation of tubes under combined loading," *International Journal of Mechanical Sciences,* vol. 30, pp. 229-248, 1988.

[37] S. Reid and K. Goudie, Denting and bending of tubular beams under local loads, New York: John Wiley & ons, 1989.

[38] Intercad Part of Central Innovation, "Lateral compression of tubes in SolidWorks," Intercad, n.d.. [Online]. Available: http://intercad.com.au/resources/technical-blog/lateral-compression-of-tubes-in-solidworks/. [Accessed 02 July 2015].

[39] J. A. DeRuntz and P. Hodge, "Crushing of a Tube Between Rigid Plates," *Journal of Applied Mechanics,* vol. 30, no. 3, pp. 391-395, 1963.

[40] S. Reid and T. Reddy, "Effect of strain hardening on the lateral compression of tubes between rigid plates," *International Journal of Solids and Structures,* vol. 14, no. 3, pp. 213-225, 1978.

[41] A. Sherbourne and F. Lu, "Strain hardening in the moving hinge method," *International Journal of Solids and Structures,* vol. 30, no. 24, pp. 3475-3489, 1993.

[42] R. Burton and J. Craig, "An investigation into the energy absorbing properties of metal tubes loaded in the transverse direction," BSc(Eng) report, University of Bristol, Bristol, 1963.

[43] R. Redwood, "Discussion of (DeRuntz JA & Hodge PG 1963)," *ASME Journal of Applied Mechanics,* vol. 31, p. 357, 1964.

[44] A. Olabi, E. Morris and M. Hashmi, "Metallic tube type energy absorbers: A synopsis," *Thin-Walled Structures,* vol. 45, pp. 706-726, 2007.

[45] S. Reid, Laterally compressed metal tubes as impact energy absorbers, London: Butterworths London, 1983.

[46] Insurance Institute for Highway Safety, "IIHS Side impact test program rating guidelines," IIHS, Virginia, 2006.

[47] M. Ashby, A. Evans, N. Fleck, L. Gibson, J. Hutchinson and H. Wadley, Metal Foams: A Design Guide, Woburn: Butterworth-Heinemann, 2000.

[48] H. Grover, "Material property design criteria for metals. In: WADC technical report 55-150, Part VI, The conventional short elevated temperature properties of selected high alloys.," ASTIA Document. No. AD 142043, 1957.

[49] G. Sun, X. Tian, J. Fang, F. Xu, G. Li and X. Huang, "Dynamical bending analysis and optimization design for functionally graded thickness (FGT) tube," *International Journal of Impact Engineering,* vol. 78, pp. 128-137, 2015.

[50] T. L. Teng, K. C. Chang and C. H. Wu, "Development and Validation of Side Impact Crash and Sled Testing Finite Element Models," *Vehicle System Dynamics,* vol. 45, no. 10, pp. 925-937, 2007.

[51] J. Fang, Y. Gao, G. Sun, Y. Zhang and Q. Li, "Parametric analysis and multiobjective optimization for functionally graded foam-filled thin-wall tube under lateral impact," *Computational Materials Science,* vol. 90, pp. 265-275, 2014.

[52] D. Muller, A. Mowat and A. Malan, *Future Fast Aeroelastic Simulation Technologies,* Cape Town: University of Cape Town, 2010.

[53] Y.-Y. Jing and D. C. Barton, "The response of square cross-section tubes under lateral impact loading," *International Journal of Crashworthiness,* vol. 3, no. 4, pp. 359-378, 1998.

[54] J. Hallquist, LS-DYNA Theory Manual, Livermore, California: Livermore Software Technology Corporation, 2006.

[55] H. Zarei and M. Kroger, "Bending behavior of empty and foam-filled beams: Structural optimization," *International Journal of Impact Engineering,* vol. 35, pp. 521-529, 2008.

[56] R. S. R. Husin, N. L. T. Lile and S. Yaacob, "Optimization of Circular Side Door Beam for Crashworthiness Analysis," *International Journal on Advanced Science Engineering Information Technology,* vol. 2, no. 3, pp. 58-62, 2012.

[57] N. Harle, J. Brown and M. Rashidy, "A Feasibility Study For An Optimising Algorithm To Guide Car Structure Design Under Side Impact Loading," *International Journal of Crashworthiness,* vol. 4, no. 1, pp. 71-92, 1999.

[58] P. Marklund and L. Nilsson, "Optimization of a car body component subjected to side impact," *Structural and Multidisciplinary Optimization,* vol. 21, pp. 383-392, 2001.

[59] H.-S. Kim, G. Ben and N. Sugimoto, "Comparison of Experimental Results with FEM for Impact Response Behavior of CFRP Tubes and CFRP/Al Hybrid Beams for Absorbing Impact Energy in Full-lap and Side Collisions of Automobiles," Research Institute of Industrial Technology, Nihon University, Tokyo, 2007.

[60] J. Njuguna, "The Application of Energy Absorbing Structures on Side Impact Protection Systems," *International Journal of Computer Applications in Technology,* vol. 40, no. 4, pp. 280-287, 2011.

[61] E. Markiewicz, P. Ducrocq and P. Drazetic, "An inverse approach to determine the constitutive model parameters from axial crushing of thin-walled square tubes," *International Journal of Impact Engineering,* vol. 21, no. 6, pp. 433-449, 1998.

[62] M. Langseth, O. Hopperstad and A. Hanssen, "Crash behavior of thin-walled aluminium members," *Thin-Walled Structures,* vol. 32, pp. 127-150, 1998.

[63] M. Dietenberger, M. Buyuk and C.-D. (. Kan, "Development of a High Strain-Rate Dependent Vehicle Model," in *LS-DYNA Anwenderforum*, Bamberg, 2005.

[64] A. Olabi, E. Morris, M. Hashmi and M. Gilchrist, "Optimised design of nested circular tube energy absorbers under lateral impact loading," *International Journal of Mechanical Sciences,* vol. 50, pp. 104-116, 2008.

[65] G. Belingardi, E. Koricho and J. Ji, "Crashworthiness evaluation of composite vehicle side door," in *International Conference on Impact Loading of Lightweight Structures*, Cape Town, 2014.

[66] L. Wu and J. F. Carney, "Experimental analyses of collapse behaviors of braced elliptical tubes under lateral compression," *International Journal of Mechanical Sciences,* vol. 40, no. 8, pp. 761-777, 1998.

[67] H. Lukman, A. R. A. Ghani, H. Hashim and M. S. b. SaifulBahri, "Impact response of circular tube with multiple slot geometry," *European International Journal of Science and Technology,* vol. 3, no. 7, pp. 271-283, 2014.

[68] G. Belingardi and J. Obradovic, "Numerical crash analysis of composite racing car front impact attenuator by use of explicit FEM codes," *Applied Mechanics and Materials,* vol. 82, pp. 290-295, 2011.

[69] M. Miyazaki, H. Endo and H. Negishi, "Dynamic axial plastic buckling of square tube," *Journal of Materials Processing Technology,* vol. 85, pp. 213-216, 1999.

[70] L. Lanyon and W. Hampson, "Bone deformation recorded in vivo from strain gauges attached to the tibial shaft," *Acta Orthopaedica Scandinavica,* 1975.

[71] D. Burr, C. Milgrom, D. Fyhrie, M. Forwood, M. Nyska, A. Finestone, S. Hogshaw, E. Saiag and A. Simkin, "In vivo measurement of human tibial strains during vigorous activity," New York, 1996.

[72] S. Simunovic, P. K. V. V. Nukala, J. Fekete, D. Meuleman and M. Milititsky, "Modeling of Strain Rate Effects in Automotive Impact," in *Society of Automotive Engineers*, 2003.

[73] D. B. Gladman, LS-DYNA Keyword Users Manual Volume II: Material Models, Livermore: Livermore Software Technology Corporation (LSTC), 2014.

[74] G. Cowper and P. Symonds, "Strain hardening and strain-rate effects in the impact loading of cantilever beams," Brown University Division of Applied Mathematics, Providence, 1957.

[75] S. Bodner and P. Symonds, "Experimental and theoretical investigation of the plastic deformation of cantilever beams subjected to impulse loading," *Journal of Applied Mechanics,* vol. 29, pp. 719-728, 1962.

[76] P. Symonds and C. Chon, "Approximation techniques for impulsive loading of structures of time-dependent plastic behaviour with finite-deflections," *Mechanical Properties of Materials at High Strain Rates,* vol. 21, pp. 299-316, 1974.

[77] M. Forrestal and M. Sagartz, "Elastic-plastic response of 304 stainless steel beams to impulse loads," *Journal of Applied Mechanics,* vol. 45, pp. 685-687, 1978.

[78] J. Paik and A. Thayamballi, Ultimate Limit State Design of Steel Plates Structures, London: John Wiley and Sons, 2002.

[79] P. Cunat, "Stainless steel properties for structural automotive applications," euro inox, Cologne, 2000.

[80] EUR 18412, "Light weight automotive construction with steel," European Commission, 1999.

[81] "Development & Validation of a Finite Element Model for the 2010 Toyota Yaris Passenger Sedan (NCAC 2011-T-001)," The National Crash Analysis Center, Washington, 2011.

[82] The Engineering Toolbox, "Friction and Coefficients of Friction," The Engineering Toolbox, n.d.. [Online]. Available: http://www.engineeringtoolbox.com/friction-coefficients-d_778.html. [Accessed 2015 October 23].

[83] M. Waldron, Interviewee, *Material composition interactions at the Centre for Imaging and Analysis, University of Cape Town.* [Interview]. 03 August 2015.

[84] Zwick GmbH & Co. KG, *Zwick Roell,* Ulm: GmbH, 2015.

[85] The National Crash Analysis Center, "Finite Element Model Archive," George Washington University, Washington, 2014.

[86] P. Blatz and W. Ko, "Application of finite elastic theory to the deformation of rubbery materials," *Transactions of The Society of Rheology,* vol. 6, pp. 223-251, 1962.

[87] N. Artimovich and D. Albin, "U.S. Department of Transportation Federal Highway Administration," The Federal Highway Administration, 30 June 2014. [Online]. Available: http://safety.fhwa.dot.gov/roadway_dept/policy_guide/road_hardware/ctrmeasures/mash/. [Accessed 12 February 2015].

[88] NHTSA, ""New Car Assessment Program Frontal Barrier Impact Test -Toyota Motor Corporation 2007 Toyota Yaris", NHTSA Test 5677," MGA Research Corporation, Burlington, WI, 2006.

[89] NHTSA, “"New Car Assessment Program Frontal Barrier Impact Test - Toyota Motor Corporation 2008 Toyota Yaris 3-Door Liftback", NHTSA Test 6221,” MGA Research Corporation, Burlington, WI, 2007.

[90] US DOT, “FMVSS No.201,” Japan Automobile Standards Internationalization Center, 2005.

[91] L. Richardson, “The deferred approach to the limit. Part I. single lattice. Part II. interpenetrating lattices,” *Philosophical Transactions of the Royal Society of London,* vol. 226, no. 1, pp. 299-361, 1927.

[92] R. Ramsdale, “Reference Tables -- Coefficient of Friction,” Engineer's Handbook, n.d.. [Online]. Available: http://www.engineershandbook.com/Tables/frictioncoefficients.htm. [Accessed 01 July 2015].

[93] Photron, “Photron High Speed Cameras,” n.d.. [Online]. Available: http://www.photron.com/. [Accessed 10 June 2015].

[94] L. Barbato, “Tracker 4.91,” Open Source Physics, 01 October 2015. [Online]. Available: http://www.opensourcephysics.org/items/detail.cfm?ID=7365. [Accessed 15 August 2015].

[95] R. R.K., “AME 50542 Manufacturing Processes for Engineering Materials Lecture Notes,” University of Notre Dame, Notre Dame, 2003.

[96] M. Bambach, H. Jama, X. Zhao and R. Grzebieta, “Hollow and concrete filled steel hollow sections under transverse impact loads,” *Engineering Structures,* vol. 30, pp. 2859-2870, 2008.

[97] H. Thairy and Y. Wang, “A Numerical Study of the Behaviour and Failure Modes of Axially Compressed Steel Columns Subjected to Transverse Impact,” *International Journal of Impact Engineering,* pp. <10.1016/j.ijimpeng.2011.03.005>. <hal-00829114>, 2011.

[98] Argus Media Service, “MetalPrices.com,” Argus Media Service, 23 November 2015. [Online]. Available: http://www.metalprices.com/. [Accessed 06 January 2016].

[99] P. E. Labossiere, “ME354 Mechanics of Materials Laboratory,” University of Washington, Autumn 2007. [Online]. Available: http://courses.washington.edu/me354a/Energy%20methods.pdf. [Accessed 18 August 2015].

[100] DuPont Fluoroproducts, “RJ Chase Company, Inc.,” n.d.. [Online]. Available: http://www.rjchase.com/ptfe_handbook.pdf. [Accessed 01 October 2015].

[101] M. J. Vermeulen, "Dynamic Impact Loading of Scaled Steel Frame," Blast Impact and Survivability Research Unit, Cape Town, 2015.

[102] P. Roache, "Quantification of uncertainty in computational fluid dynamics," *Annual Review of Fluid Mechanics,* vol. 29, pp. 123-160, 1997.

Appendix A

Analytical Beam Bending Solution

Consider a beam subjected to bending due to impact loading at a point at an arbitrary point along the length of the beam as illustrated in Figure 8.1.

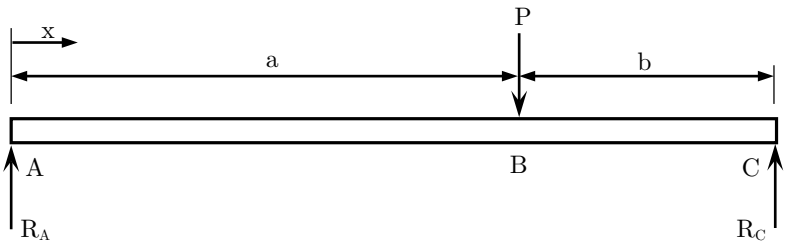

Figure 8.1: Simply supported beam under bending, subjected to transverse load P.

The resulting reactions may be calculated using Equations A.1 and A.2.

$$\Sigma M_C = 0 \qquad (cw+) \tag{A.1}$$

$$R_A = \frac{b}{a+b}P \quad and \quad R_C = \frac{a}{a+b}P \tag{A.2}$$

A.1. Assumptions

The following assumptions were made in the derivation of the equation describing the transverse deflection of the beam when subjected to a striking body, derived from Hearn [31].

- The striking body will exert a point load on the beam,
- No local plastic deformation will take place in the region of the striking load,
- The energy of the striking body is entirely transferred to the deformable structure,
- No energy is dissipated during the impact,
- The striking body should not bounce off the structure and retain part of its energy, and
- The inertia of the structure is negligible when compared with that of the striking body.

None of the above are satisfied in practice, however, each one leads to a conservative design of the structure and is a necessary simplification of the problem to make hand calculation possible without considerable complexity.

A.2. Slope and deflection of a simply supported beam

To determine the transverse deflection as a result of a load P it is necessary to double integrate the moment equations to give Equation A.7.

$$\frac{dy}{dx} = \frac{1}{EI}\int_{\Omega} M\,dx \tag{A.3}$$

$$\frac{dy}{dx} = \frac{1}{EI}\int_{0}^{a+b} \frac{Pbx}{a+b} - P[x-a]\,dx \tag{A.4}$$

$$\frac{dy}{dx} = \frac{P}{EI}\left(\frac{b}{2(a+b)}x^2 - \frac{1}{2}[x-a]^2 + A\right) \tag{A.5}$$

Integrating the slope equation thus yields the deflection equation in A.7.

$$y = \frac{P}{EI}\int_{\Omega} \left(\frac{b}{2(a+b)}x^2 - \frac{1}{2}[x-a]^2 + A\right) dx \tag{A.6}$$

$$y = \frac{P}{EI}\left(\frac{b}{6(a+b)}x^3 - \frac{1}{6}[x-a]^3 + Ax + B\right) \tag{A.7}$$

Boundary conditions are given in Equation A.8,

$$y = 0 \;\; at \;\; x = 0 \qquad and \qquad y = 0 \;\; at \;\; x = a+b \tag{A.8}$$

Applying boundary conditions to Equation A.7 yields Equations A.9 and A.10,

$$A = \frac{b^3}{6(a+b)} - \frac{b(a+b)}{6} \tag{A.9}$$

$$B = 0 \tag{A.10}$$

The point of maximum deflection for a simply supported beam is expected to occur at the point in which the slope is zero, thus set the slope Equation A.5 to zero and substitute for A, it follows that the position of maximum deflection is,

$$x = \pm\sqrt{\frac{a}{3}(a+2b)} \tag{A.11}$$

Given that the beam exists between $x = 0$ and $x = a + b$ where a and b are positive numbers, the negative term from Equation A.11 can be ignored. Substituting A.9, A.10 and A.11 back into A.7 yields the equation for the transverse deflection of a beam subjected to load P.

$$y_{max} = \frac{P}{EI}\left(\frac{b}{6(a+b)}\left(\frac{a}{3}(a+2b)\right)^{\frac{3}{2}} - \frac{1}{6}\left[\left(\frac{a}{3}(a+2b)\right)^{\frac{1}{2}} - a\right]^3 + \left(\frac{b^3}{6(a+b)} - \frac{b(a+b)}{6}\right)\left(\frac{a}{3}(a+2b)\right)^{\frac{1}{2}}\right) \tag{A.12}$$

The quantity in Macaulay brackets may be ignored if the magnitude of the position x of maximum deflection is less than the geometric quantity a.

A.3. Determination of P using method of internal energy

Strain energy as a result of an induced bending moment is defined as,

$$U = \int_0^l \frac{M^2}{2EI}dx \tag{A.13}$$

where the bending moment "M" is defined in Equation A.14 using Macaulay's method.

$$M = \frac{Pbx}{a+b} - P[x-a] \tag{A.14}$$

Substituting the moment equation into the integral equation for strain energy and multiplying out yields Equation A.15.

$$U = \int_0^{a+b} \left(\frac{Pb}{a+b}\right)^2 x^2 - \frac{2P^2bx[x-a]}{a+b} + P^2[x-a]^2\,dx \tag{A.15}$$

Applying integration by parts to the middle term in Equation A.15 and integrating yields,

$$U = \frac{(Pab)^2}{6(a+b)EI} \tag{A.16}$$

Now equating the internal energy in the beam as a function of the load "P" to the kinetic energy in the striker when contact is made yields Equation A.18.

$$\frac{(Pab)^2}{6(a+b)EI} = \frac{1}{2}mv^2 \tag{A.17}$$

$$P = \sqrt{\frac{3mv^2EI(a+b)}{(ab)^2}} \tag{A.18}$$

Equation A.18 shows the equivalent representative static load P that would cause the same transverse deflection as with the dynamic case.

A.4. Determination of P using linear load deflection assumption

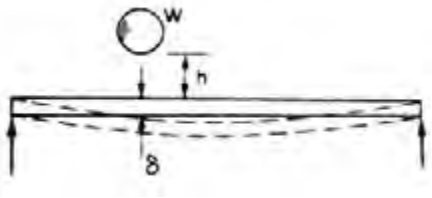

Figure 8.2: Impact load - bending application [31].

Consider a load P applied statically to the beam as shown in Figure 8.1. The work done by that static load when the beam deflects by δ is,

$$E = \frac{1}{2}P\delta \tag{A.19}$$

If this were equated to the potential energy of some mass m dropped by some height h from the unloaded beam it would produce equation A.20, from where P was made the subject in Equation A.21.

$$mg(h+\delta) = \frac{1}{2}P\delta \tag{A.20}$$

$$P = \frac{2mg(h+\delta)}{\delta} \tag{A.21}$$

However, if the weight of the dropped mass were applied statically then by proportionality it can be inferred that,

$$P = \frac{\delta}{\delta_s}mg \tag{A.22}$$

Thus equating Equations A.21 and A.22, and solving for the dynamic deflection δ yields,

$$\delta = \delta_s\left(1 \pm \sqrt{1+\frac{2h}{\delta_s}}\right) \tag{A.23}$$

Applying Equation A.18 and A.12 together will provide the first analytical solution. The second analytical solution is produced by setting the load P in Equation A.12 to mg where m is the mass of the striking object. This will yield the transverse static deflection of the beam, which is then substituted into Equation A.23 to give the dynamic deflection as a result of dropping the same mass m from a height h.

Appendix B

Tube Lateral Compression Theory

This section seeks to establish a relationship between compression force and deflection of a square and round tube subjected to elastic lateral tube compression. The underlying assumptions made during the derivation are stated where necessary. The derivations were divided into two parts, namely square and round tube derivations.

B.1. Round Tube Compression Theory

Suppose there is a curved member subjected to compression as shown in Figure 8.3.

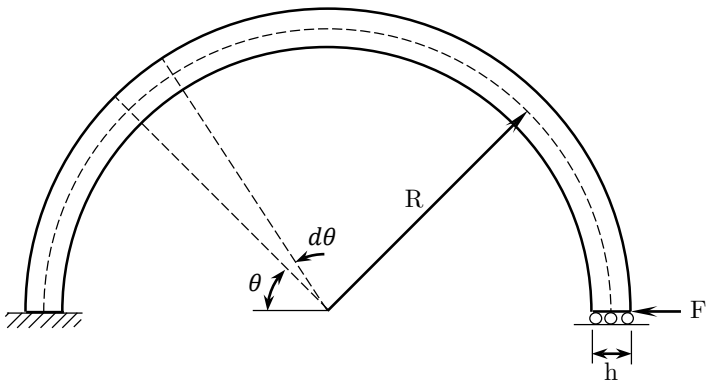

Figure 8.3: Flexible half cylindrical specimen subjected to elastic loading (F).

Assuming that the material is linear elastic and that energy is conserved upon application of load F, that is to say all work done on the curved member is converted to stored internal energy. The corresponding three forms of energy may be divided into direct compressive, shear, and bending loading. These three loading conditions are shown in Figure 8.4 for a single element along the circumference of the curved member.

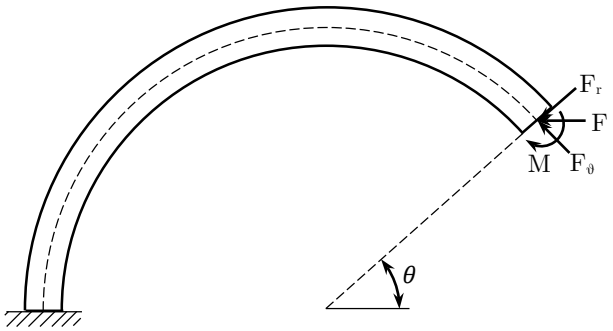

Figure 8.4: Elemental force breakdown at some angle θ from the applied load.

Castigliano's theorem states that the deflection of any linear elastic structure as a result of an applied inline load is equal to the partial derivative of the total strain energy with respect to the load. The corresponding equation describing the deflection δ at the point of application of a force F is given by Equation B.24.

$$\delta_i = \frac{\partial U}{\partial F_i} \tag{B.24}$$

The following derivation is largely based on the works of Paul E. Labossiere [99]. If a small element is defined by the elementary angle dϑ as per Figure 8.3 the strain energy may be divided in accordance with the three loads inferred from F. The strain energies as a result of direct compression, shear, and bending are given in Equations B.25, B.26, and B.27 respectively.

$$dU_\theta = \frac{F_\theta^2 R d\theta}{2AE} \tag{B.25}$$

$$dU_r = \frac{C F_r^2 R d\theta}{2AG} \tag{B.26}$$

$$dU_M = \frac{M^2 R d\theta}{2EI} \tag{B.27}$$

where C=1.5 for rectangular cross-sections in shear [99] and Equation B.28 only applies if the $R/h > 10$. The corresponding equation describing the total strain energy is given in B.28.

$$U = \int_{\Omega} dU_{\theta} + \int_{\Omega} dU_{r} + \int_{\Omega} dU_{M} \tag{B.28}$$

$$U = \int_{\Omega} \frac{F_{\theta}^{2} R d\theta}{2AE} + \int_{\Omega} \frac{C F_{r}^{2} R d\theta}{2AG} + \int_{\Omega} \frac{M^{2} R d\theta}{2EI} \tag{B.29}$$

And applying Equation B.24 to Equation B.29, yields Equation B.30.

$$\delta = \frac{\partial U}{\partial F} = \int_{0}^{\pi} \frac{F_{\theta} R}{AE} \left(\frac{\partial F_{\theta}}{\partial F}\right) d\theta + \int_{0}^{\pi} \frac{C F_{r} R}{AG} \left(\frac{\partial F_{r}}{\partial F}\right) d\theta + \int_{0}^{\pi} \frac{MR}{EI} \left(\frac{\partial M}{\partial F}\right) d\theta \tag{B.30}$$

The relationship between θ and the three loading conditions in element $d\theta$ from Figure 8.3 may be expressed according to Equations B.31, B.32, and B.33.

$$F_{\theta} = F sin\theta \qquad \Longrightarrow \qquad \frac{\partial F_{\theta}}{\partial F} = sin\theta \tag{B.31}$$

$$F_{r} = F cos\theta \qquad \Longrightarrow \qquad \frac{\partial F_{r}}{\partial F} = cos\theta \tag{B.32}$$

$$M = \frac{FR}{2}\left(cos\theta - \frac{2}{\pi}\right) \qquad \Longrightarrow \qquad \frac{\partial M}{\partial F} = \frac{R}{2}\left(cos\theta - \frac{2}{\pi}\right) \tag{B.33}$$

From equation B.33 it can be shown that the bending is at a minimum when the contents of the brackets are zero, which occurs at $\theta \approx 50°$ and $\theta \approx 310°$, and the bending moment is a maximum at $\theta = 0°$ and $\theta = 90°$.

$$M_{min} = 0 \quad at \quad \theta = cos^{-1}\left(\frac{2}{\pi}\right) \approx 50° \; and \; 310° \tag{B.34}$$

$$M_{max} = \frac{FR}{\pi} \quad at \quad \theta = 0° \quad and \quad 90° \tag{B.35}$$

By substituting Equations B.31, B.32, and B.33 into Equation B.30, and integrating yields Equation B.36.

$$\delta = \frac{\pi FR}{2AE} + \frac{\pi CFR}{2AG} + \frac{0.1488 FR^{3}}{2EI} \tag{B.36}$$

If, however, the mean diameter to thickness ratio is large, the first two terms are negligibly small in comparison with the 3rd term. Thus Equation B.36 becomes.

$$\delta = \frac{0.1488FR^3}{2EI} \tag{B.37}$$

B.2. Square Tube Compression Theory

Suppose there is a square tube oriented on its corner to make a diamond shape, subjected to compression as shown in Figure 8.5.

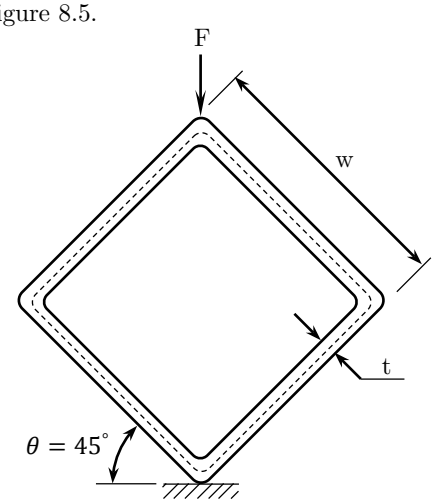

Figure 8.5: Flexible square tube specimen subjected to elastic loading (F).

A quarter symmetry model of Figure 8.5 is shown in Figure 8.6 for the purpose of deriving the force versus deflection equation.

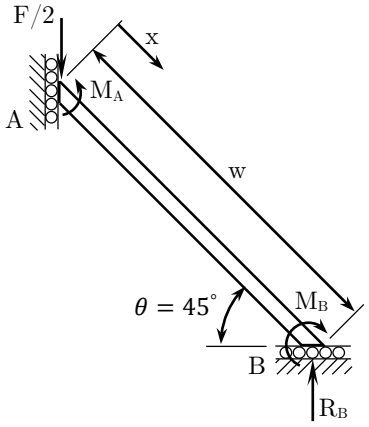

Figure 8.6: Flexible square tube specimen subjected to elastic loading (F).

Assuming that the material is linear elastic and that upon application of load F all work done on the specimen is converted to stored internal energy. The corresponding three forms of energy may be divided into direct compressive, shear, and bending load forms. These three loading conditions are shown in Figure 8.7 for a single element along the width of one edge of the member.

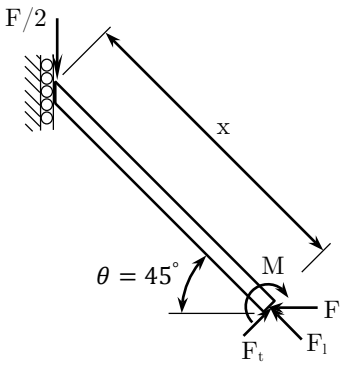

Figure 8.7: Elemental force breakdown at some position x from the applied load.

As there are no externally applied horizontal loads the reactive force at A will be zero. Also the only reactive load to resist the application of force F is at B which is vertical. There will be reactive couples at both ends of the quarter symmetry boundary preventing any rotations at the boundary. The corresponding moment equation as per Figure 8.6, where clockwise is taken as positive, is given by Equation B.38.

$$M_A - M_B - \frac{Fw}{2\sqrt{2}} = 0 \tag{B.38}$$

And the Moment as measured about an arbitrary distance x from the applied load is given in Equation B.39.

$$M(x) = -M_A - \frac{Fx}{2\sqrt{2}} \tag{B.39}$$

From equation B.39 it can be shown that the bending is a minimum at $x = 0$, and the bending moment is at a maximum when x= w.

$$M_{min} = -M_A \quad at \quad x = 0 \tag{B.40}$$

$$M_{max} = -M_A - \frac{Fw}{2\sqrt{2}} \quad at \quad x = w \tag{B.41}$$

To determine the transverse deflection as a result of a load $F/2$ it is necessary to double integrate the moment Equation B.42 to give B.45 deflection.

$$EI\frac{d^2\delta_M}{dx^2} = M \tag{B.42}$$

$$EI\frac{d^2\delta_M}{dx^2} = -M_A - \frac{Fx}{2\sqrt{2}} \tag{B.43}$$

$$EI\frac{d\delta_M}{dx} = \int -M_A - \frac{Fx}{2\sqrt{2}}\,dx \tag{B.44}$$

$$EI\frac{d\delta_M}{dx} = -M_A x - \frac{Fx^2}{4\sqrt{2}} + C_1 \tag{B.45}$$

Applying the boundary condition $\frac{d\delta_M}{dx} = \theta = 0$ at $x = 0$ yields Equation B.46.

$$C_1 = 0 \tag{B.46}$$

And applying boundary condition $\frac{d\delta_M}{dx} = \theta = 0$ at $x = w$ yields Equation B.47.

$$M_A = -\frac{Fw}{4\sqrt{2}} \tag{B.47}$$

Substituting Equations B.46 and B.47 into B.45 yields Equation B.48,

$$EI\frac{d\delta_M}{dx} = \frac{Fw}{4\sqrt{2}}x - \frac{Fx^2}{4\sqrt{2}} \tag{B.48}$$

Now integrating, again:

$$EI\delta_M = \int \frac{Fwx}{4\sqrt{2}} - \frac{Fx^2}{4\sqrt{2}}dx \tag{B.49}$$

$$EI\delta_M = \frac{Fwx^2}{8\sqrt{2}} - \frac{Fx^3}{12\sqrt{2}} + C_2 \tag{B.50}$$

Applying the boundary condition $\delta_M = 0$ at $x = w$,

$$C_2 = -\frac{Fw^3}{24\sqrt{2}} \tag{B.51}$$

Now substituting Equation B.51 into B.50 and setting δ_M as the subject of the formula gives the equation for the deflection due to bending:

$$\delta_M = \frac{1}{EI}\left(\frac{Fwx^2}{8\sqrt{2}} - \frac{Fx^3}{12\sqrt{2}} - \frac{Fw^3}{24\sqrt{2}}\right) \tag{B.52}$$

Thus to find the deflection at the point of application of load F set $x = 0$ in Equation B.52.

$$\delta_M = -\frac{Fw^3}{24\sqrt{2}EI} \tag{B.53}$$

As for the direct compression and shear components, the deflection at the point of application of the point load F is determined using Equations B.54, B.55, and B.56.

$$\delta_l = \frac{\sigma w}{E} \tag{B.54}$$

$$\delta_l = \frac{-Fw}{2\sqrt{2}AE} \tag{B.55}$$

$$\delta_l = \frac{-F}{2\sqrt{2}lE} \tag{B.56}$$

The deflection due to longitudinal compression given in Equation B.56 is of an order of magnitude smaller than the deflection due to bending for high width to thickness ratios w/t. Similarly, the deflection due to shear across the width of the tube is negligibly small and thus excluded from the final equation for the deflection of the tube. Therefore, the equation describing the full elastic deflection of the tube subjected to a point load on its edge is given in B.57 and B.58.

$$\delta = \delta_M + \delta_l + \delta_t \tag{B.57}$$

$$\boxed{\delta = -\frac{Fw^3}{24\sqrt{2}EI}} \tag{B.58}$$

Appendix C

Side Impact Beam Calculations

This section describes the calculations performed in the design of the side impact beam experimental test rig.

C.1. Determination of the striker impact point

The impact point on the door in the full vehicle model takes place at a distance 360 mm from the short end of the 928.8 mm length tube. The angle through which the tube buckles due to impact is 63.3°. This results in a centre distance reduction of approximately 70 mm. Therefore due to the test rig boundary conditions differing from the full scale test the distance of the pivoted collar from the bolted side is determined from the average centre distance from before and after impact as shown in Figure 8.8. This results in an approximate distance of 880-900 mm.

To minimise the effect of the test rig boundary conditions on the results the sliding collar support should be closest to the striker impact point, however, due to spatial limitations in the drop tester the bolted side must be mounted to the rear/wall side.

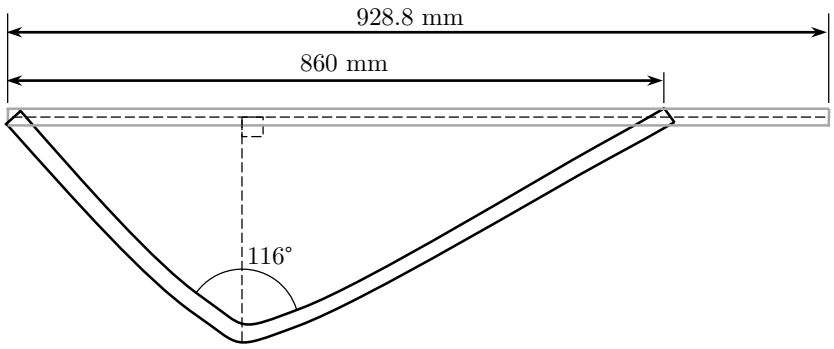

Figure 8.8: Deflection geometry of a front door tube in a 4-door sedan in a side impact with a Ø10 inch rigid vertical pole at 29 km/h with the pole 1045.75 mm longitudinally from the front axle.

Due to spatial constriction the actual distances equate to an impact point of approximately 322 mm from the bolted pivot, and 557 mm from the Polytetrafluoroethylene (PTFE) collar.

C.2. Teflon Insert Strength Calculations

To ensure a low coefficient of friction on the sliding support of the side impact beam test apparatus a PTFE collar separated the tube from the support. As a result, due to the cost of Teflon and the importance of the correct functioning of the collar it was identified as a high value item, necessitating the need for these calculations. To ensure an adequately sized collar was used some basic calculations were performed to determine the approximate size, followed by a verification using FEA. These calculations are described in short below.

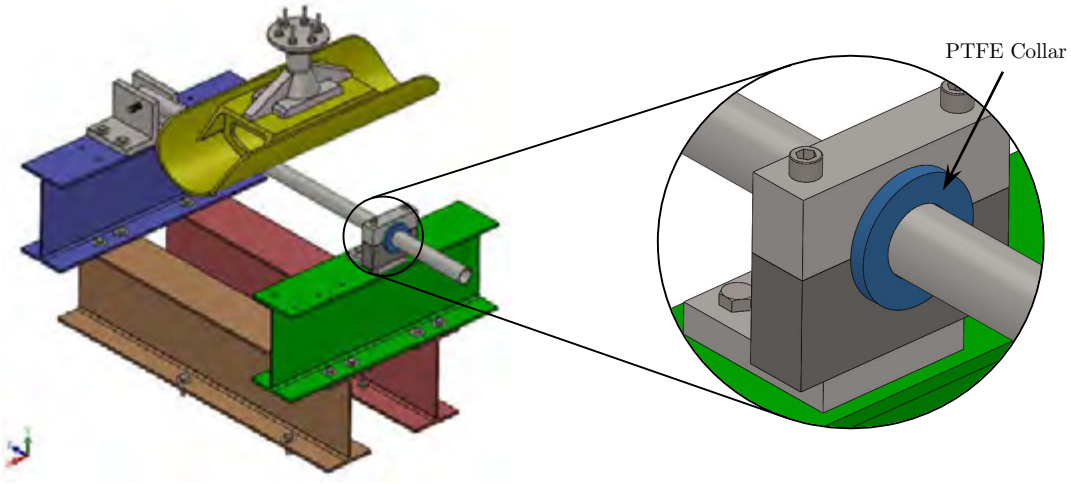

Figure 8.9: Side impact beam drop test apparatus, with PTFE collar detail view.

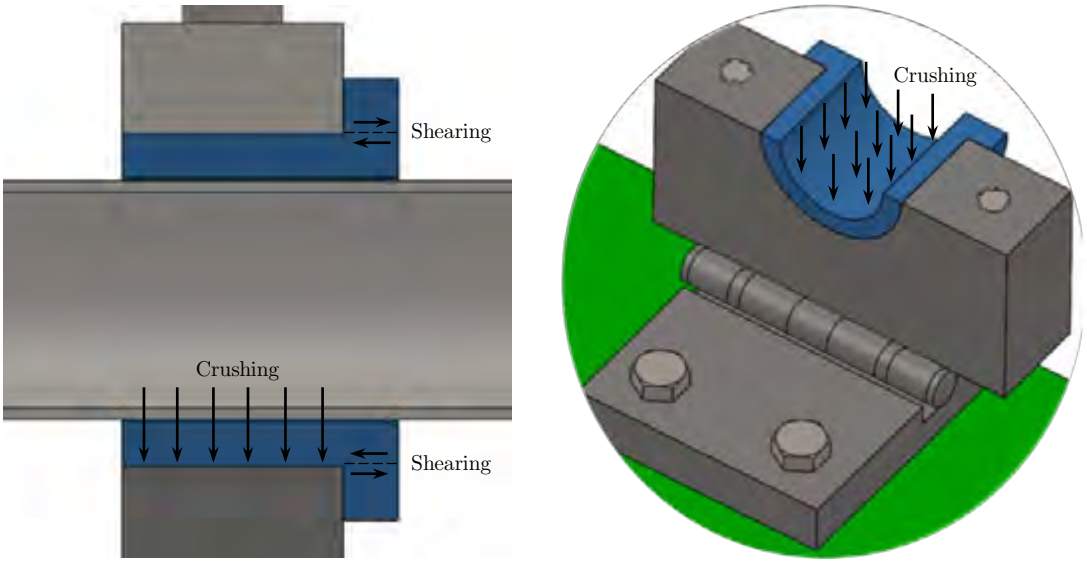

Figure 8.10: Idealised loading conditions on the PTFE collar in the sliding pivot.

The 2 main loading conditions identified that were used in the design of the Teflon collar were direct crushing and shear loading. The diameter of the tube was constant at Ø43 mm with the mass of the striker being 200 kg and the maximum velocity at the point of impact was 3.13 m/s due to a drop height of 500 mm. Therefore, assuming a uniform load across the vertically downward projected area, the minimum collar length can be computed. It should be noted that transients such as vibration and the inertial effect of the pillow block support were not accounted for here. Thus a FE simulation is conducted using the results of these calculations to confirm that the collar is strong enough. As from (A.3) in Appendix A the equivalent static load due to the impact is given by Equation C.1.

$$P = \sqrt{\frac{3mv^2EI(a+b)}{(ab)^2}} \tag{C.1}$$

Which yielded an equivalent static load of 44272 N. And given that the PTFE collar was on the side furthest from the impact load, the collar support must be able to support is given by Equation C.2.

$$R_A = \frac{b}{a+b}\sqrt{\frac{3mv^2EI(a+b)}{(ab)^2}} \tag{C.2}$$

Which can be reduced to Equation C.3.

$$R_A = \sqrt{\frac{3mv^2EI}{a^2(a+b)}} \tag{C.3}$$

This resulted in a load at the collar support of 16209 N. It is known that the Yield strength of Teflon is 9 MPa [100]. Therefore the area can be calculated.

$$A = \frac{F}{\sigma_y} = \frac{16209}{9 \times 10^6} \approx 1800\ mm^2 \tag{C.4}$$

Given that the tube had an outside diameter of 43 mm, the length of the collar may be calculated from the projected area.

$$l = \frac{A}{d} = \frac{1800}{43} = 41.9\ mm \approx 50\ mm \tag{C.5}$$

The shear force is small given that the friction between the collar and tube should be counteracted by the frictional force between the collar and pillow block housing. The lip was only added to prevent any possible pull through while the striker is descending, a thickness of 10 mm was chosen. The spring back also plays a role in that it may cause the collar to pull through on rebound, however, this is accounted for by giving a small interference between the collar and pillow block support.

The subsequent collar geometries were modelled in LS-DYNA using the simplified Johnson-Cook material model with a viscoplastic formulation for rate effects with the following parameters:

Table 8.1: Material parameters for PTFE using the simplified Johnson-Cook material model in LS-DYNA.

Material Parameter	**Quantity**
Mass Density	2200 kg/m^3
Young's Modulus	625.01 MPa
Poisson's Ratio	0.46
A	9.2 MPa
B	10.5 MPa
N	0.36
C	0.041

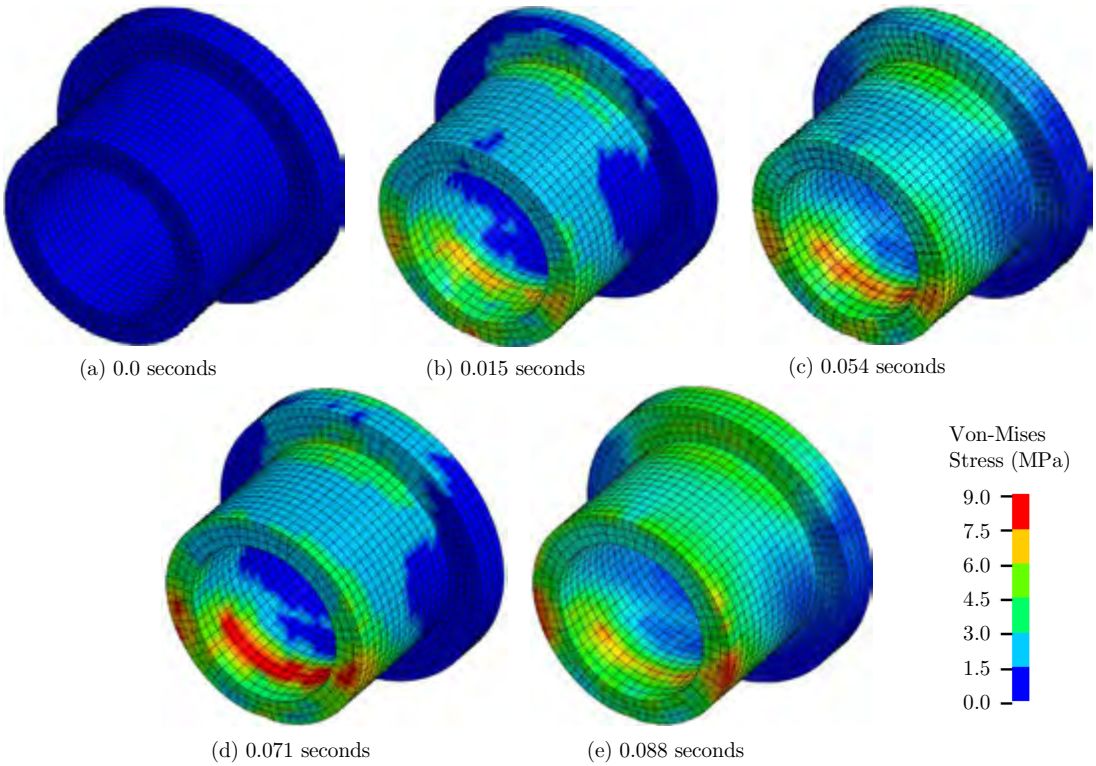

Figure 8.11: Von-Mises stress at five different instances in time on the surface of the PTFE collar during impact.

The Von-Mises stress contour illustration in Figure 8.11 shows that the limit of stress was reached in localised regions on the leading edge of the inner surface. The animation showed a rotary oscillation of the pillow block support about the pivot point which caused the stress to oscillate as well. This should not happen in the experiment as the hinge was damped with grease, which was not modelled in the FE model. Also the impact velocity of 3.31 m/s was ambitious as this would only be the case if the striker fell with no-friction. And from the work of Vermeulen [101] there were approximately 10-20% losses in striking velocity in the BISRU drop tester from the ideal velocity.

Appendix D

Richardson Extrapolation

A mesh sensitivity study is necessary when there is no closed loop feedback from experimental results. One example would be when the numerical simulations are used to determine a set of parameters that cannot be obtained from any other technique and the magnitude thereof is affected by the density of the mesh. In such cases, if there is no other way of verifying the results through experimentation or an analytical approach a mesh sensitivity study is necessary. A trade-off is typically made between accuracy and computational expense.

A technique for determining the zero grid spacing solution f_{extrap}, also known as the mesh independent solution, was developed by Richardson [91] using three design points. The technique extrapolates the asymptotic solution from the design cases where the difference between each design parameter and the asymptotic solution can be determined for the purpose of calculating the error. The Richardson extrapolation technique as described by Roache [102] is given firstly by the mesh independent solution described by Equation D.1.

$$f_{extrap} \cong f_j + \frac{f_j - f_{j+1}}{r^p - 1} \tag{D.1}$$

where r is the ratio between average grid spacing of solutions j and $j+1$, and p is the order of accuracy which is determined iteratively. Typically an order of accuracy of two is chosen for the first iteration. Richardson extrapolation requires a minimum of three working solutions to function. The grid spacing ratios between each solution is given by the equations in D.2.

$$r_{12} = \frac{h_2}{h_1} \qquad r_{23} = \frac{h_3}{h_2} \tag{D.2}$$

The relative error between solutions f_j are then computed as per equations in D.3.

$$\epsilon_{12} = f_2 - f_1 \qquad \epsilon_{23} = f_3 - f_2 \tag{D.3}$$

The extrapolated asymptotic solution is computed using Equation D.1, after calculating the order of accuracy using the iterative equations given in D.4 and D.5.

$$p_{12}(i+1) = \omega p_{12}(i) + (1-\omega)\frac{ln[\beta_{12}(i)]}{ln[r_{12}]} \tag{D.4}$$

$$p_{23}(i+1) = \omega p_{23}(i) + (1-\omega)\frac{ln[\beta_{23}(i)]}{ln[r_{23}]} \tag{D.5}$$

where β_{12} and β_{23} in Equations D.4 and D.5 are determined using the equations in D.6.

$$\beta_{12}(i) = \frac{\left(r_{12}^{p_{12}(i)}\right)\epsilon_{23}}{\left(r_{23}^{p_{12}(i)}\right)\epsilon_{12}} \qquad \beta_{12}(i) = \frac{\left(r_{12}^{p_{12}(i)}\right)\epsilon_{23}}{\left(r_{23}^{p_{12}(i)}\right)\epsilon_{12}} \tag{D.6}$$

Typically convergence of the order of accuracy is achieved within one or two dozen iterations. The extrapolated asymptotic solutions f_{12}^{extrap} and f_{23}^{extrap} should equate indicating the successful convergence on the mesh independent solution, from where the accuracies of numerical solutions f_1, f_2 and f_3 relative to the mesh independent solution can be calculated.